Titre: Title:	Development of a New Multi-Channel MRI Coil Optimized for Brain Studies in Human Neonates
Auteur: Author:	Nibardo Lopez Rios
Date:	2017
Type:	Mémoire ou thèse / Dissertation or Thesis
Référence: Citation:	Lopez Rios, N. (2017). Development of a New Multi-Channel MRI Coil Optimized for Brain Studies in Human Neonates [Thèse de doctorat, École Polytechnique de Montréal]. PolyPublie. https://publications.polymtl.ca/2816/

UNIVERSITÉ DE MONTRÉAL

DEVELOPMENT OF A NEW MULTI-CHANNEL MRI COIL OPTIMIZED FOR BRAIN STUDIES IN HUMAN NEONATES

NIBARDO LOPEZ RIOS

DÉPARTEMENT DE GÉNIE ÉLECTRIQUE

ÉCOLE POLYTECHNIQUE DE MONTRÉAL

THÈSE PRÉSENTÉE EN VUE DE L'OBTENTION

DU DIPLÔME DE PHILOSOPHIAE DOCTOR

(GÉNIE ÉLECTRIQUE)

NOVEMBRE 2017

UNIVERSITÉ DE MONTRÉAL

ÉCOLE POLYTECHNIQUE DE MONTRÉAL

Cette thèse intitulée :

DEVELOPMENT OF A NEW MULTI-CHANNEL MRI COIL OPTIMIZED FOR BRAIN STUDIES IN HUMAN NEONATES

présentée par : LOPEZ RIOS Nibardo

en vue de l'obtention du diplôme de : Philosophiae Doctor

a été dûment acceptée par le jury d'examen constitué de :

M. LESAGE Frédéric, Ph. D., président

M. COHEN-ADAD Julien, Ph. D., membre et directeur de recherche

M. DEHAES Mathieu, Ph. D., membre et codirecteur de recherche

M. CALOZ Christophe, Ph. D., membre

M. NEAR Jamie, Ph. D., membre externe

DEDICATION

To Linnet, Mario and Laura

ACKNOWLEDGEMENTS

First, I would like to express my special appreciation to my supervisors Prof. Julien Cohen-Adad and Prof. Mathieu Dehaes, for their support and trust. I would like to thank them for giving me the opportunity to work on such exciting projects. I also want to express my immense gratitude for the constructive discussions, advise and direct help with experiments. I am very fortunate to be allowed work in the highly skilled research group and pleasant environment that Prof. Julien Cohen-Adad has created.

I would like to thank my thesis committee, Prof. Frédéric Lesage, Prof. Christophe Caloz and Prof. Jamie Near for accepting to participate in my defense. My sincere appreciation for using your time to read and evaluate my manuscript, and for your brilliant comments and suggestions.

I thank also Prof. Gregory Lodygensky for the valuable advice and collaboration since the very beginning of the project. I thank our collaborators Fraser Robb, Miguel Navarro, Pei H. Chan, Jorge Guzman, and Kellie Tribbey from GE Healthcare for their valuable support, technical assistance and encouragement. I appreciate also the aid received from Brian A. Hargreaves from Stanford University. I also thank Jonathan Polimeni from the MGH Martinos Center for sharing his code to compute the SNR.

I would like to acknowledge the funds received by the Canada Research Chair in Quantitative Magnetic Resonance Imaging, the Canadian Institute of Health Research (CIHR FDN-143263), the Canada Foundation for Innovation (32454), the Fonds de Recherche du Québec - Santé (28826, 32600), the Fonds de Recherche du Québec - Nature et Technologies (2015-PR-182754), the Natural Sciences and Engineering Research Council of Canada (435897-2013, 2015-04672), the Québec Bio-Imaging Network (5886) and a fellowship from the CREER (FRQNT).

I thank my lab mate Alexandru Foias for the great discussions and his valuable support in many aspects. In addition, I would like to thank Prof. Nikola Stikov and my fellow students and researchers Tanguy Duval, Benjamin De Leener, Ryan Topfer, Gabriel Mangeat, Grégoire Germain, Sara Dupont, Charley Gros, Simon Lévy, Tommy Boshkovski, Agah Karakuzu, Manh-Tung Vuong, Aldo Zaimi, Atef Badji, Christian Perone, Stephanie Alley, Ariane Saliani, Hadi Begdouri, Harris Nami, Pierre-Olivier Quirion, George Peristerakis, Jennifer Campbell, Darya Morozov, Pascale Beliveau and many others for their support and for being such a nice workgroup.

I thank also Prof. Frédéric Lesage and Philippe Pouliot for their important support with related research. Many thanks also to all my Professors for such interesting courses and workshops.

I would like to thank my family and friends: especially to my wife Linnet for her love and for being always so supportive; to my parents Nibardo and Melvis, to my brothers Jose Enrique and Pedro, and my daughter Laura for their vital support, and finally to my son Mario for being a new motivation for everything. To my friends and colleagues in Cuba for their preoccupation and valuable help in difficult moments. Without all of them, this work would not have been so pleasant.

RÉSUMÉ

Plusieurs événements et conditions indésirables causent des lésions cérébrales chez les nouveau-nés qui peuvent conduire plus tard à des troubles neurodéveloppementaux. Des études d'imagerie rapides, non invasive et de haute qualité sont nécessaires pour initier un traitement neuroprotecteur précoce et minimiser les effets néfastes sur ces patients. L'imagerie par résonance magnétique (IRM) est une méthode de choix pour détecter ces lésions et évaluer le développement du cerveau in vivo. Les systèmes d'IRM comprennent des antennes spécifiques qui permettent d'interagir avec l'objet étudié au moyen de signaux radiofréquences (RF). Ces antennes jouent un rôle important sur la qualité d'image résultante et donc sur notre capacité à détecter des pathologies subtiles. Plus les antennes sont proches du tissu à imager, meilleure est la qualité d'image.

Le but de ce travail était de développer une nouvelle antenne de réception IRM qui peut s'adapter physiquement à la taille de la tête des nouveau-nés dans la gamme de prématurés de 24 semaines à des bébés de 1.5 mois.

L'antenne est constituée de treize éléments répartis de manière sphérique, fixés individuellement à un soufflet en plastique compressible, qui peuvent se déplacer de manière indépendante dans des directions radiales et axiales. Un système pneumatique les rétracte au moyen d'un vide, en maximisant l'espace à l'intérieur de l'antenne pour faciliter le placement du sujet. Le vide est ensuite libéré pour permettre l'expansion du soufflet et le mouvement des éléments vers le centre de l'antenne jusqu'à ce qu'ils s'adaptent physiquement à la forme de la tête. La simulation électromagnétique a aidé le processus de conception, révélant la faisabilité de l'idée proposée. Un découplage efficace à l'aide de préamplificateurs a garanti les niveaux requis de découplage global entre les canaux de l'antenne. La validation a été effectuée sur le banc d'essai et sur une IRM 3T en utilisant différents fantômes en forme de tête.

Les résultats démontrent une augmentation moyenne de rapport signal-à-bruit (SNR) de jusqu'à 68% dans la région de la tête et 122% dans la région du cortex, par rapport à une antenne commerciale de tête à 32 canaux. La distribution du SNR est stable pour toutes les tailles de fantômes utilisés.

En conclusion, une antenne de réception a été conçue, modélisée puis construite. Cette antenne est adaptable avec contrôle pneumatique, ce qui a permis un SNR plus élevée par rapport à une antenne de tête commerciale à 32 canaux utilisée normalement dans la pratique clinique. Les risques

associés à la pression mécanique sur la tête des nouveau-nés sont inexistants (utilisation de pression négative versus positive) et le mouvement de la tête est restreint. En plus, la méthode a des applications potentielles à d'autres groupes d'âge et parties du corps.

ABSTRACT

Several adverse events and conditions cause brain injury in neonates that can later lead to neurodevelopmental disabilities. Fast, non-invasive and high-quality image studies are required to initiate early neuroprotective treatment and minimize adverse effects on these patients. Magnetic Resonance Imaging (MRI) is a vital method to detect these injuries and assess brain development in vivo. The MRI systems include specific types of antennas, commonly known as radiofrequency (RF) coils, to interact with the object under study by means of RF signals. These coils play a strong role on the resulting image quality and hence on our ability to detect subtle pathologies. The closer the coils are to the scanned tissue, the better the image quality.

The purpose of this work was to develop a new MRI RF receiver array coil that can physically adapt to infant head sizes from 24-week premature to 1.5-month-old.

The coil is made of thirteen spherically distributed elements, individually attached to compressible plastic bellows, that can independently move in radial and axial directions. A pneumatic system retracts them by means of vacuum, maximizing the space inside the coil to facilitate the placement of the subject. The vacuum is afterward liberated to allow the expansion of the bellows and the movement of the elements toward the coil center until they physically adapt to the head shape. Electromagnetic simulation assisted the design process, revealing the feasibility of the proposed idea. A strong preamplifier decoupling guaranteed the required levels of overall decoupling among the coil elements. The validation was performed on the bench and on a 3T scanner using different head-shaped phantoms.

The results show up to up to 68% in the head region and 122% in the cortex region, compared to a 32-channel commercial head coil. A stable SNR distribution through the complete size range was also obtained for all the used phantoms.

In conclusion, an MRI receiver coil was designed, modeled, and built. The coil is adaptable with pneumatic control, which allowed a higher SNR compared to a commercial 32-channel head coil used normally in clinical practice. The risks associated with mechanical pressure on the head of newborns are non-existent (use of negative versus positive pressure) and the head motion is restricted. In addition, the method has potential applications to other age groups and body parts.

TABLE OF CONTENTS

LIST OF TABLES

LIST OF FIGURES

List of symbols and abbreviations

DTI	Diffusion tensor imaging
ESR	Equivalent Series Resistance
FEM	Finite Element Method
FID	Free induction decay
FOV	Field-of-view
GE	General Electric
GRE	Gradient Recalled Echo
iSNR	Intrinsic signal-to-noise ratio
MoM	Method of Moments
MPRAGE	Magnetization Prepared Rapid Gradient Echo
MR	Magnetic resonance
MRI	Magnetic resonance imaging
MRS	Magnetic resonance spectroscopy
NF	Noise figure
NMR	Nuclear magnetic resonance
PCB	Printed circuit board
PI	Parallel imaging
Q	Quality factor
Q_U	Unloaded quality factor
Q_L	Loaded quality factor
RF	Radio frequency
RL	Return loss
ROI	Region-of-interest

rSoS	Root-sum-of-squares
Rx	Receiver
SENSE	SENSitivity Encoding
SMASH	SiMultaneous Acquisition of Spatial Harmonics
SNR	Signal-to-noise ratio
T1	Longitudinal relaxation
T2	Transverse relaxation
TE	Echo time
TR	Repetition time
Tx	Transmitter
Tx/Rx	Transmitter/Receiver
uiSNR	Ultimate intrinsic SNR
VLBW	Very low birth weight

LIST OF APPENDICES

CHAPTER 1 INTRODUCTION

1.1 Problem

Neonatal brain injury and abnormality due to adverse events or conditions, such as intracranial hemorrhage, stroke or vascular anomalies, are frequent in very low birth weight (VLBW) preterm infants and newborns with birth asphyxia or congenital heart disease [1], [2], [3], [4]. The injuries resulting from these events, can later lead to significant neurodevelopmental disabilities. Fast and high-quality image studies are required to initiate early neuroprotective treatment and minimize the adverse effects on the newborns. Since the clinical manifestations of the neurological diseases are very subtle in the newborn infant, mainly in the premature [4], there is a great need for high-resolution imaging of the neonatal brain. Magnetic Resonance Imaging (MRI) is currently one of the methods of choice to detect neonatal brain injury and assess brain development in vivo [5]. Advanced MRI techniques, such as magnetic resonance spectroscopy (MRS) and diffusion tensor imaging (DTI), have contributed to enrich the field of the neonatal brain studies, triggering an important amount of research and applications [5]. MRS is used to measure local brain compounds that are valuable in assessing metabolic changes associated with brain development and injury. DTI is used to characterize the three-dimensional spatial distribution of water diffusion in each voxel of the MRI scan, which provides a sensitive measure of regional brain microstructural development.

On the other hand, MRI systems include specific types of antennas, commonly known as radio frequency (RF) coils, to interact with the object under study by means of RF signals. High-energy excitation pulses are sent with a transmitter coil to the object, which afterward emits a very weak response signal that is captured by a receiver coil. These coils play a strong role on the resulting image quality and hence on our ability to detect subtle pathologies. Their design parameters are closely related to the geometry and composition of the object.

Regardless of the importance of imaging studies in infants, only a limited number of fixed-size receiver coils for the neonatal brain is commercially available, among which a few arrays can be distinguished [6], [7]. It was demonstrated that higher image Signal-to-Noise Ratio (SNR) is obtained by means of receive array coils closely positioned on the subject [8]. On the other hand, it is known that the dimensions and shape of the head in the pediatric population are highly variable,

mainly during the first weeks of age when the brain is undergoing maturational processes. Accordingly, the performance of a fixed-size coil is optimal for the largest head that fits into it while it shows poorer image parameters as the head dimensions reduce. This is even worse in the clinical practice, where standard adult head or knee coils are used. In these cases, the difference in dimensions is even bigger, as the inner diameter of an adult coil is around 24 cm. Some commercial flexible coils and pediatric birdcages are also used, but they do not have the best potential for neonatal brain studies due to their cylindrical configuration, among other disadvantages. To improve SNR with these alternatives, the typical solutions involve longer scan times, which is more likely to produce images with increased motion artifacts and may affect the physiological conditions of these most vulnerable patients.

A few optimized but not commercially available pediatric head coils were proposed. One approach is based in a set of age-matched arrays that resulted in optimal images, but it also has practical inconveniences related to cost and workflow [9], [10]. These results were the main motivation for subsequent efforts, including the present work. A different approach is based on adjustable coils based in arrays divided in two or four sections that are moved by means of actuators [11], [12], [13], [14]. The ideas presented in these works might be used to build a neonatal coil, but no evidence of a constructed adjustable coil for infants was found during this project. In addition, these ideas present potential risks for the fragile head of the neonates. More details are provided in 3.5.

1.2 Goal

The purpose of this work is to develop and evaluate a novel size-adaptable receive RF array coil which can be used to scan a variety of infant head sizes, including preterm and term babies, to increase image SNR compared to fixed-size coils.

1.2.1 General approach

The project was focused on the design, construction and evaluation of a first-of-its-kind MRI neonatal receiver array coil. The coil was specifically built for a 3T scanner (Signa MR750, GE Healthcare, Wauwatosa, WI, USA) but the same design can be applied to other MRI models or field strengths. The number of channels, dimensions and shape were optimized to obtain a high SNR in the intended population. Improved SNR compared to commercial coils, high levels of

comfort for the newborn, adjustability to the head size, simplicity of utilization of life support systems, such as endotracheal tubes and incubators, were the optimizing criteria. Improvements were also anticipated in Parallel Imaging (PI) applications.

The structure of the loops and the general decoupling among them in different conditions were evaluated by electromagnetic field simulations during the design process. 3D design and printing tools were used to model and build the coil. Phantoms of different sizes were also constructed to simulate the presence of the patients in the coil through the test stages. The array was initially adjusted and assessed in the workbench. Then, it was evaluated in the scanner by following standard methods. The results were compared to a fixed-size commercial coil.

CHAPTER 2 MRI OVERVIEW

Magnetic Resonance Imaging (MRI) is a diagnosis method that combines the use of magnetic fields of different nature with the magnetic properties of certain atomic nuclei, such as hydrogen (^{1}H), to create very detailed images of the biological tissue. It is based on Nuclear Magnetic Resonance (NMR), a phenomenon that was discovered simultaneously and independently by Felix Bloch and Edward Mills Purcell, who received the Nobel Prize in Physics in 1952. The first 2D images were produced by Paul Lauterbur and Sir Peter Mansfield in the 1970s, who were also awarded the Nobel Prize in Physiology or Medicine in 2003 for their development of MRI. Raymond Damadian developed the first MR scanner and obtained the first human body images in 1977.

MRI uses radio frequency (RF) signals that are in the commercial spectrum and does not need ionizing radiation, which makes it a safer imaging method compared to other modalities, such as X-ray, computed tomography (CT) and molecular imaging (use of radiotracers). Other important advantages of this method are the amount of information contained in the images and the possibility of adjusting the MRI protocol to boost or reduce the effects of the intrinsic parameters of the object under study, which generates images with different contrast. Cellular structure, flow and diffusion can be studied with this versatile method.

The NMR experiment can be explained in a simple way. The selected nuclei align with a strong magnetic field created by a magnet. They are rotated by using a RF pulse, and afterward they return to the equilibrium alignment oscillating in the magnetic field and emitting a RF signal at the same time.

2.1 System architecture

An MRI machine is made of several blocks among which three main components can be distinguished: the magnet, the magnetic field gradient system and the RF system. A simplified block diagram is presented in Figure 2.1. The magnet is placed in a completely shielded room (Faraday cage) to isolate the RF signals from the electromagnetic environment. The magnet generates a strong and uniform static magnetic field, known as $\boldsymbol{B_0}$, which polarizes the nuclear spins. Clinical scanners typically have B_0 from 1.5 to 3 Tesla (T). The homogeneity of B_0 is corrected with a lower magnetic field created by a set of active shim coils, in addition to a set of static metallic plates carefully positioned during scanner installation. The magnetic field gradient system produces controlled spatial and time dependent magnetic fields that are superposed to $\boldsymbol{B_0}$

with the purpose of signal localization. The typical range for imaging goes from 0 to 10 mT/m with switching times of 1 ms between these values. The RF system consists of a transmitter coil and a receiver coil, or other combinations. The transmitter coil is used to excite the target spin system and must generate a rotating and uniform RF magnetic field $\boldsymbol{B_1}$. The receiver coil is designed and built to have sufficient sensitivity to capture the very low signal emitted by the spins due to the excitation. Excitation pulses can have a peak power of more than 30 kW while the NMR signal is in the range of the microvolts. The MRI systems are normally equipped with a set of different receiver coils with specific designs according with the body parts. Array coils made of simple wire loops are currently the most common coil configurations for reception and, with the progressive increase of B_0 fields, they are also used for transmission.

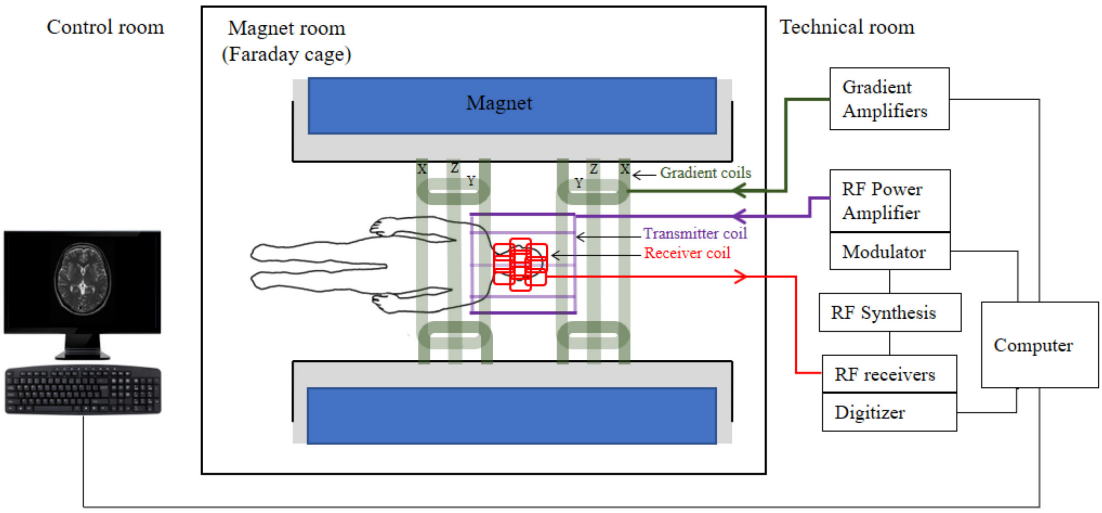

Figure 2.1 Simplified block diagram of an MRI system.

Most electronic blocks, such as power amplifiers, synthesizers, receivers and computers are installed in the technical room. The scanner is controlled by the operator from the control room.

2.2 MRI principles

2.2.1 Magnetization

Nuclei with odd number of protons or neutrons have an angular momentum $\boldsymbol{J}$, also called spin. The atom of hydrogen, for instance, has only one proton. It is the most used element to create MRI images mainly because of its abundance in the biological tissue. Spin is usually represented by a physical rotation about its axis, as shown in Figure 2.2. The ensemble of all spins of the same type

in an object, as hydrogen, is called a spin system. It is known that a magnetic field is created around the nucleus that has finite dimensions, electrical charge and rotates around its own axis. This magnetism resembles the field created by a very small magnet. It is called magnetic moment and is represented by a vector quantity $\boldsymbol{\mu}$. The magnetic moment is related to the angular moment by [15]:

$$\boldsymbol{\mu} = \gamma \boldsymbol{J} = 2\pi \not{\gamma} \boldsymbol{J} \tag{2.1}$$

where γ is the gyromagnetic ratio, which is a physical constant that is different for each nucleus. For ^{1}H, γ = 2.65 x 108 rad/s/T and $\not{\gamma}$ = 42.58 MHz/T. The direction of $\boldsymbol{\mu}$ is random due to the thermal motion if no external magnetic field exists. In consequence, the net magnetization of a macroscopic object is zero.

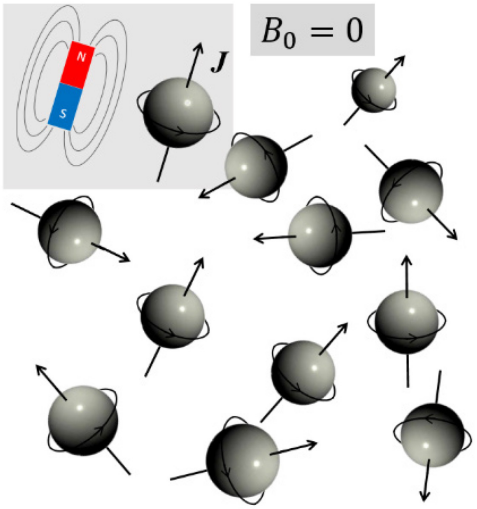

Figure 2.2 Nuclei spinning around their own axis and oriented in random directions when no external magnetic field ($\boldsymbol{B_0} = 0$) is applied. Each nucleus behaves as a very small magnet as shown on the top left corner.

When a spin system in placed in a magnetic field, a nuclear macroscopic magnetism, which is the physical basis of the MRI, appears. The external magnetic field is conventionally called $\boldsymbol{B_0}$ and it is parallel to the z-axis of the MRI frames, so that:

$$\boldsymbol{B}_0 = B_0 \boldsymbol{k} \tag{2.2}$$

A single magnetic moment vector of the spin system partially aligns with the external magnetic field $\boldsymbol{B}_0$ taking one of two possible orientations, parallel (↑) and antiparallel (↓), as shown in Figure 2.3. A small number of nuclei in excess is oriented in the positive z direction. They define the net

magnetization $\boldsymbol{M}$ pointing in the direction of $\boldsymbol{B_0}$. The transverse component of $\boldsymbol{M}$ is zero because the nuclei precess with random phase. Each magnetic moment also shows a motion around the z-axis called nuclear precession. This movement is analogous to the movement of a spinning top and it is described by the following equation [15]:

$$\begin{cases} \mu_{xy}(t) = \mu_{xy}(0)e^{-i\gamma B_0 t} \\ \mu_z(t) = \mu_z(0) \end{cases} \tag{2.3}$$

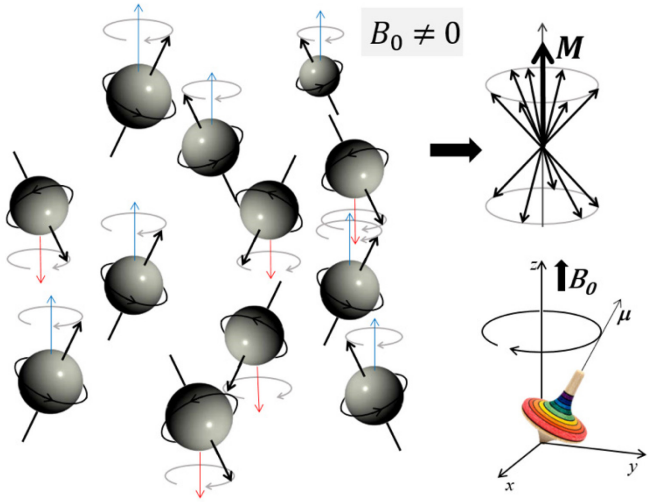

Figure 2.3 The spin system of Figure 2.2 placed in a magnetic field. On the left, all magnetic moments are precessing around opposite directions along the z-axis: parallel (blue z-axis) and antiparallel (red z-axis). On the top right, the spin system is represented as two precessing cones formed by the magnetic moment vectors. The precession motion is illustrated by the movement of a spinning top on the bottom right.

The angular frequency of the nuclear precession, derived from this expression, is known as the Larmor frequency:

$$\omega_0 = \gamma B_0 \tag{2.4}$$

According to this expression the resonance frequency of a spin system is determined by the magnetic field magnitude and its gyromagnetic ratio.

The macroscopic magnetization vector $\boldsymbol{M}$ is used to characterize the spin system as a sum of all magnetic moments:

$$\boldsymbol{M} = \sum_{n=1}^{N_S} \boldsymbol{\mu}_n \tag{2.5}$$

where N_s is the number of spins in the system. As stated before, $\boldsymbol{M} = 0$ when the system is not in a $\boldsymbol{B}_0$ field. If the system is placed in an external magnetic field, $\boldsymbol{M}$ will change as all spins will be oriented in two directions. These two spin groups interact with different energy levels with the $\boldsymbol{B}_0$ field. The group with parallel alignment is in a low-energy state and the antiparallel is in a high-energy state, being the energy difference [15]:

$$\Delta E = E_{\downarrow} - E_{\uparrow} = \gamma \hbar B_0 = \gamma h B_0 / 2\pi \tag{2.6}$$

where h is the Plank's constant (6.6 x10^{-34} J-s) and $\hbar$ is equal to $h/2\pi$.

The population difference between both groups of spins is related to this energy difference:

$$N_{\uparrow} - N_{\downarrow} \approx N_s \frac{\gamma \hbar B_0}{2kT_s} \tag{2.7}$$

where k = 1.38 x 10^{-23} is the Boltzmann's constant and T_s is the absolute temperature of the spin system. From this expression, one can notice that only a few spins in excess are in the low-energy state, which is more stable. For example, only about nine in one million of protons will contribute to the NMR signal at 3T. This small group defines the magnitude of the net magnetization:

$$M_z^0 = |\boldsymbol{M}| = \frac{\gamma^2 \hbar^2 B_0 N_s}{4kT_s} \tag{2.8}$$

it normally points along the z-axis and is proportional to the external magnetic field and the number of spins. This is the reason why images obtained with high field scanners are preferred, as a higher number of spins in excess provides more SNR.

2.2.2 Excitation

When an external oscillating magnetic field $\boldsymbol{B}_1(t)$ is applied on the spin system and it rotates in the same way as the precessing spins, the resonance condition is established. It is expressed by:

$$\omega_{rf} = \omega_0 \tag{2.9}$$

In this condition, the energy transmitted by a radio wave of frequency ω_{rf} induces transitions of spins between energy levels. This energy is transmitted in the MRI experiment by means of radio frequency pulses that last for microseconds to milliseconds. The magnitude, in the range of the tens of mT, is very low compared to the static magnetic field.

A typical $\boldsymbol{B}_1$ field is expressed by [15]:

$$\boldsymbol{B}_1(t) = 2B_1^e(t)\cos\big(\omega_{rf}t + \varphi\big)\boldsymbol{i} \tag{2.10}$$

where $B_1^e(t)$ is the envelope of the pulse, that can have different shapes such as rectangular or *sinc* (cardinal sine function), ω_{rf} is the carrier frequency and φ is the initial phase. This is an *x*-oriented linearly polarized field that can be decomposed into two circularly polarized fields rotating in opposite directions:

$$\begin{aligned}\boldsymbol{B}_1(t) = B_1^e(t)\big[\cos\big(\omega_{rf}t + \varphi\big)\boldsymbol{i} - \sin\big(\omega_{rf}t + \varphi\big)\boldsymbol{j}\big] \\ + B_1^e(t)\big[\cos\big(\omega_{rf}t + \varphi\big)\boldsymbol{i} + \sin\big(\omega_{rf}t + \varphi\big)\boldsymbol{j}\big]\end{aligned} \tag{2.11}$$

The first term rotates clockwise and the second counterclockwise on the *xy*-plane, which is perpendicular to $\boldsymbol{B}_0$. For the purpose of excitation, the first term, also known as B_1^+, is the useful one as it rotates in the same direction as the spins. Then, the excitation field can be expressed as:

$$B_1(t) = B_{1,x}(t) + iB_{1,y}(t) = B_1^e(t)e^{-i(\omega_{rf}t+\varphi)} \tag{2.12}$$

The second term is called B_1^- and it is a field that rotates in the opposite direction of the nuclear precession. According to the principle of reciprocity [16] the magnitude of the current induced in the receiver coil by $\boldsymbol{M}$ is proportional to the magnitude of this field. In other words, the effectiveness of the receiver coil is proportional to its efficiency as a transmitter coil.

A rotating frame of reference with its *z*-axis aligned with $\boldsymbol{B}_0$ and its transverse plane rotating at ω_0 (and ω_{rf} at resonance), is introduced to facilitate the description of the $\boldsymbol{B}_1$, or RF pulse. It is distinguished from the conventionally used stationary frame by using *x'*, *y'* and *z'* to denote the axis. After the introduction of the necessary transformations between both frames, the use of the Bloch equation [15] shows that $\boldsymbol{M}$ performs a precession around the direction of the axis in the rotating frame where the exciting field $\boldsymbol{B}_1(t)$ was applied (if $\varphi = 0$, this axis will be the *x'*-axis). For a rectangular RF pulse the situation in the rotating frame is similar to having $\boldsymbol{B}_0$ for a short time in the conventional frame. In this case $\boldsymbol{M}$ in the rotating frame is described by:

$$\begin{cases} M_{x'}(t) = 0 \\ M_{y'}(t) = M_z^0\sin(\omega_1 t) \\ M_{z'}(t) = M_z^0\cos(\omega_1 t) \end{cases} \qquad 0 \le t \le \tau_p \tag{2.13}$$

where $\omega_1 = \gamma B_1$. This means that $\boldsymbol{M}$ precesses around the *x'*-axis with angular velocity:

$$\boldsymbol{\omega}_1 = -\gamma\boldsymbol{B}_1 \tag{2.14}$$

which is very similar to the Larmor relationship as the precession frequency depends on the applied RF field. This motion is called forced precession and it is represented in Figure 2.4.

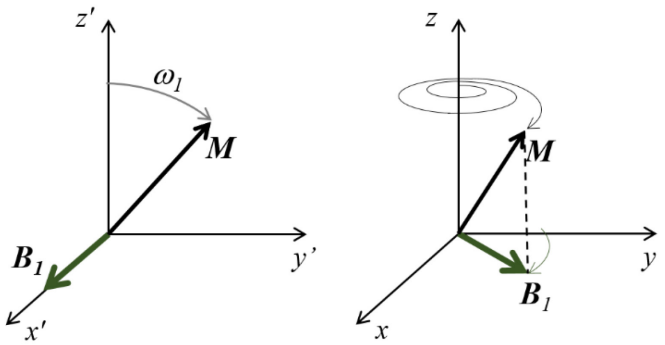

Figure 2.4 $\boldsymbol{M}$ movement caused by $\boldsymbol{B}_1$ in the rotating frame (left), and in the conventional or laboratory frame (right).

The separation from the *z'*-axis, which is called tipping, creates a component in the transverse plane $\boldsymbol{M}_{x'y'}$ that can be externally detected. The magnetization will tip as long as the $\boldsymbol{B}_1$ field is applied. When $\boldsymbol{B}_1$ is switched off $\boldsymbol{M}$ will stop tipping. The angle at this point, known as flip angle, depends on the magnitude of $\boldsymbol{B}_1$ and the pulse length τ_p. For a rectangular pulse, it is:

$$\alpha = \omega_1 \tau_p = \gamma B_1 \tau_p \tag{2.15}$$

To choose the excitation bandwidth the length of the pulse is selected first. Then, the RF power is adjusted to select the flip angle. According to (2.14), the tipping is faster if the RF power is higher.

When $\boldsymbol{M}$ is tipped to the transverse plane by means of a ($\alpha =$) 90º RF pulse, it will return to its alignment with the *z*-axis, rotating around this axis after the pulse is switched off. Its projection in the *xy*-plane, represented by *Mxy*, will obviously rotate as well, as represented in Figure 2.5. If a receiver coil is conveniently placed in that plane, the varying magnetic flux created by *Mxy* will induce a RF current on it, in agreement with Faraday's law. This current is the NMR signal.

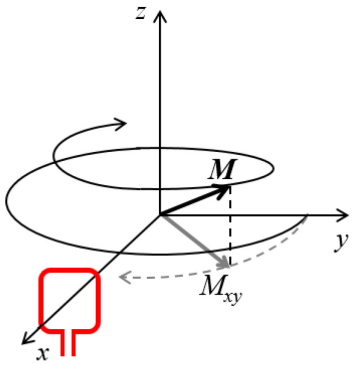

Figure 2.5 Partial trajectory of $\boldsymbol{M}$ after the RF pulse is switched off. The projection on the transverse plane induces a current in a receiver coil (in red) placed perpendicularly to the *x*-axis.

The return of the spin system to the previous equilibrium state, after the RF pulse is turned off, occurs in a certain amount of time where $\boldsymbol{M}$ exhibits a motion called free precession. The longitudinal magnetization M_z is totally recovered and the transversal magnetization M_{xy} is completely attenuated during this time. These processes are called longitudinal relaxation and transverse relaxation respectively. They are described by the following expressions, that can be obtained by solving the Bloch equations for the rotating frame [15]:

$$\begin{cases} M_{z\prime}(t) = M_z^0\left(1 - e^{-t/T_1}\right) + M_{z\prime}(0_+)e^{-t/T_1} \\ M_{x\prime y\prime}(t) = M_{x\prime y\prime}(0_+)e^{-t/T_2} \end{cases} \tag{2.16}$$

where $M_{z\prime}(0_+)$ and $M_{x\prime y\prime}(0_+)$ are the respective magnetizations immediately after the RF pulse, and M_z^0 is the longitudinal magnetization at equilibrium. T_1 and T_2 are time constants that respectively characterize these relaxation processes. T_1 is the time when $M_{z\prime}$ has gained 63% of the magnetization at equilibrium (M_z^0). On the other hand, T_2 is the time after which $M_{x\prime y\prime}$ has lost 63% of its initial magnetization ($M_{x\prime y\prime}(0_+)$). Illustrative values for biological tissues are: T_1 = 300 – 2000 ms and T_2 = 30 – 150 ms. The curves in Figure 2.6 represent both processes.

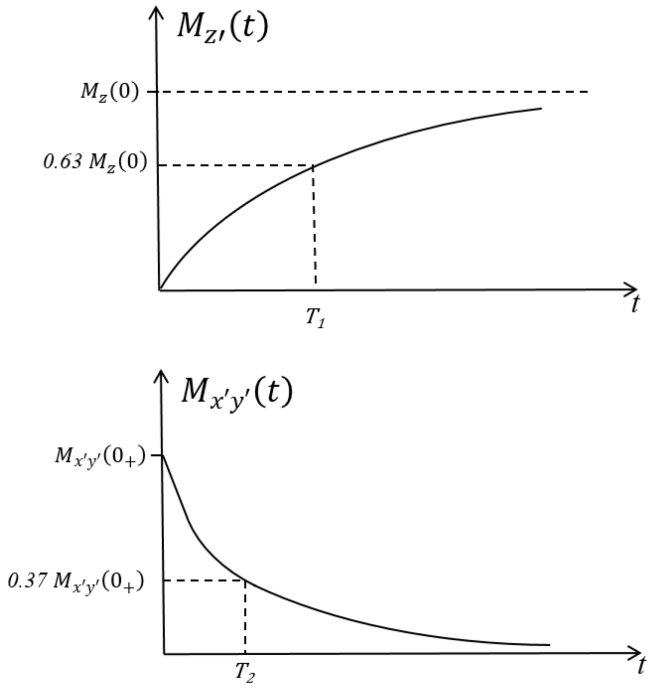

Figure 2.6 Curves that describe the longitudinal relaxation (top) and the transversal relaxation (bottom) after a 90º pulse. In these conditions $M_{z\prime}(0_+) = 0$ and $M_{z\prime}(t)$ in Equation 1.16 has only the first term on the right.

T_1 is also called spin-lattice relaxation time as it is related to the energy exchange between the spin system and the environment. T_2 on the other hand is related to field interactions among spins of the same system and is also called spin-spin relaxation time. The difference between the relaxation times of specific tissues is one of the sources of the contrast in MRI, being the high soft tissue contrast one significative advantage of this image modality.

2.2.3 FID and Echo

The free precession of $\boldsymbol{M}$ around $\boldsymbol{B}_0$ after an α pulse generates a signal called Free Induction Decay (FID). For a spin system with only one spectral component resonating at ω_0 this signal is expressed by [15]:

$$S(t) = M_z^0 \sin\alpha \, e^{-t/T_2} e^{-i\omega_0 t} \qquad t \geq 0 \tag{2.17}$$

As can be seen in this expression, the decay for this type of spin system is characterized by T_2. Also, as the maximum of the FID is reached at $t = 0$, its value is expressed by [15]:

$$A_f = M_z^0 \sin\alpha \tag{2.18}$$

Equation (2.17) is more general if the field inhomogeneities are considered, which leads to [15]:

$$S(t) = \pi M_z^0 \gamma \Delta B_0 \sin\alpha \, e^{-t/T_2^*} e^{-i\omega_0 t} \qquad t \geq 0 \tag{2.19}$$

where T_2^* is a very used time constant that is expressed by [15]:

$$\frac{1}{T_2^*} = \frac{1}{T_2} + \gamma \Delta B_0 \tag{2.20}$$

The shape of an FID of this type is shown in Figure 2.7.

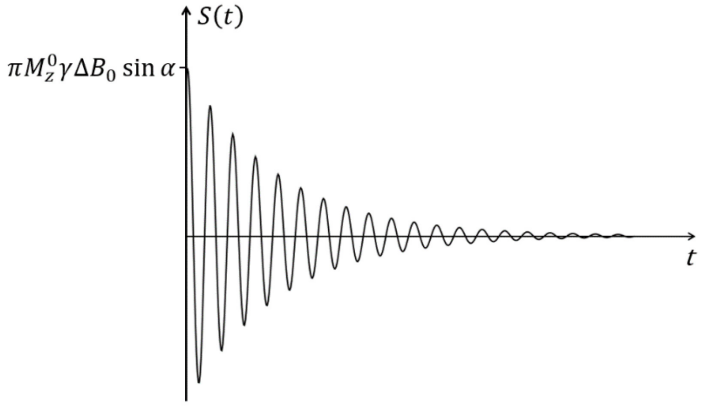

Figure 2.7 FID of a spin system having only one spectral component in an inhomogeneous magnetic field.

If a 90º RF pulse is followed by a 180º RF separated by a time interval τ, a signal called spin echo can be generated. This scheme is called 90-τ-180 and it can be illustrated by the representations in Figure 2.8.

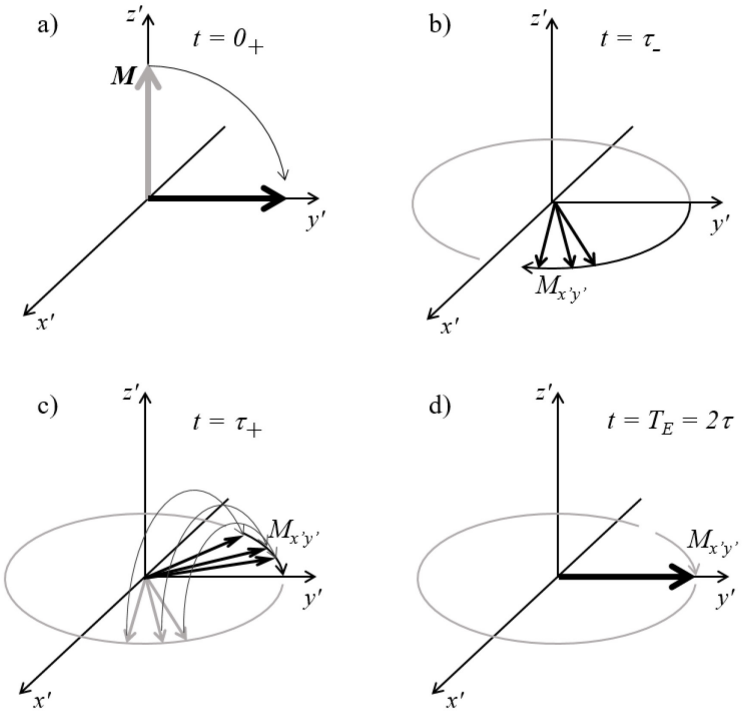

Figure 2.8 Evolution of the transverse magnetization due to a 90-τ-180 RF pulse sequence.

The rotating frame is used and, for simplicity, only the evolution of $M_{x'y'}$ after the 90º pulse ($t = 0_+$) is shown. A biological sample is initially placed in a $\boldsymbol{B}_0$ field which makes the net magnetization $\boldsymbol{M}$ ideally aligned with the *z'*-axis. If a 90º RF pulse (α_1) is applied along the *x'*-axis, $\boldsymbol{M}$ will be rotated to the *y'*-axis (a). After the pulse, $\boldsymbol{M}$ starts precessing around the *z*-axis and M_{xy} describes a circle in the *xy*-plane. But in a real sample the inhomogeneities and the interactions among the spins make them precess in a range of frequencies instead of only at ω_0. This creates a phase difference among the spins that progresses during the precession. In

Figure 2.8 (b) the $M_{x'y'}$ of some spins are shown. After a time τ, there will be a phase angle range $\Delta\omega\tau$. If now a 180º pulse (α_2) is applied along the *y'*-axis, all the $M_{x'y'}$ will be flipped to the other side of the *x'y'*-plane as shown in (c). As a result, the $M_{x'y'}$ that had the slower precession will be now ahead and the fastest ones behind. Since all the spins will continue precessing at the same frequencies and directions, after another time interval τ they will be all at the same phase as shown

in (d). In other words, after a $t = T_E = 2\tau$ the phase coherence among the spins will be recovered. This rephasing process will generate a signal called echo. The maximum amplitude of this signal is given by [15]:

$$A_E = M_z^0 \sin\alpha_1 [\sin(\alpha_2/2)]^2 \, e^{-T_E/T_2} \tag{2.21}$$

This expression shows the dependence on T_2 of the echo signal and that the maximum is reached with the previous pulse combination, but it is lower than the FID. Figure 2.9 shows the evolution of the NMR signal with the explained RF pulse combination.

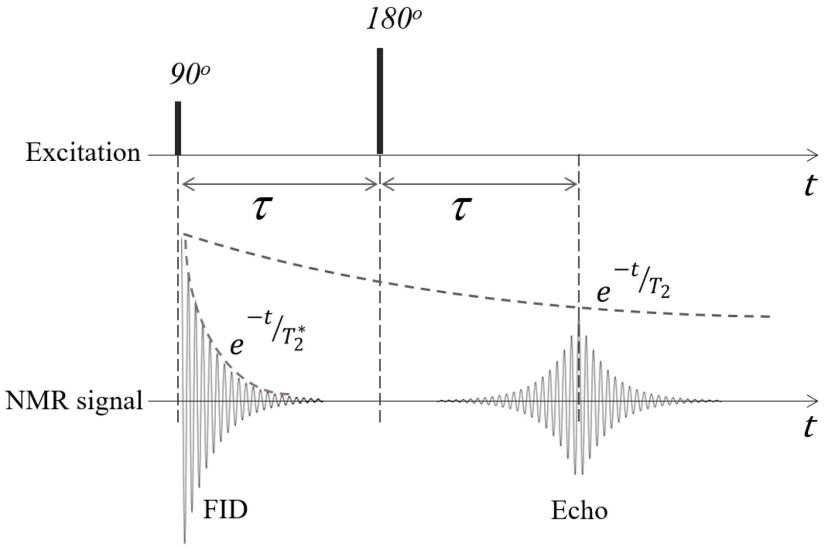

Figure 2.9 NMR signals due to a 90-τ-180 RF pulse sequence. Notice the T_2^* dependence of the FID and the T_2 dependence of the echo.

2.2.4 Signal detection

The NMR signal should be converted to an electrical signal to make it useful. Since the net magnetization is precessing at a radio frequency it can be captured by any conducting loop tuned at the same frequency by means of the Faraday law for electromagnetic induction. Taking advantage also of the principle of reciprocity [17] and after some mathematical treatment [15] the following expression for the voltage induced in a receiver loop, or coil, in the laboratory frame is found:

$$V(t) = \int_{object} \omega(\boldsymbol{r}) \left|B_{r,xy}(\boldsymbol{r})\right| \left|M_{xy}(\boldsymbol{r},0)\right| e^{-t/T_2(\boldsymbol{r})} \cos\left[-\omega(\boldsymbol{r})t + \emptyset_e(\boldsymbol{r}) - \emptyset_r(\boldsymbol{r}) + {}^{\pi}/_{2}\right] d\boldsymbol{r} \tag{2.22}$$

where $\boldsymbol{r}$ is a position in the laboratory frame, $\omega(\boldsymbol{r})$ is the free precession Larmor frequency, $M_{xy}(\boldsymbol{r},0)$ is the transverse magnetization and $B_{r,xy}(\boldsymbol{r})$ is the sensitivity of the coil determined by the principle of reciprocity, all at the point $\boldsymbol{r}$. $\emptyset_r(\boldsymbol{r})$ and $\emptyset_e(\boldsymbol{r})$ are respectively the reception phase angle and the initial phase shift introduced by the excitation.

This RF signal is afterward demodulated by using a quadrature method based in phase-sensitive detection and power combination. The output of this demodulator is a complex signal expressed by [15]:

$$S(t) = \int_{object} B^*_{r,xy}(\boldsymbol{r}) M_{xy}(\boldsymbol{r},0) e^{-i\gamma\Delta B(\boldsymbol{r})t} d\boldsymbol{r} \tag{2.23}$$

where:

$\gamma\Delta B(\boldsymbol{r}) = \Delta\omega(\boldsymbol{r})$ (accounts for the inhomogeneity of $\boldsymbol{B}_0$ during the free precession)

$B^*_{r,xy}(\boldsymbol{r}) = \left|B_{r,xy}(\boldsymbol{r})\right| e^{-i\emptyset_r(\boldsymbol{r})}$

$M_{xy}(\boldsymbol{r},0) = \left|M_{xy}(\boldsymbol{r},0)\right| e^{i\emptyset_e(\boldsymbol{r})}$

2.2.5 Spatial encoding

An image can be reconstructed from NMR signals if spatial-dependent information is added. This is achieved by spatial encoding using magnetic field gradients. Three orthogonal gradient coil systems (x, y and z directions) are provided in the scanners with this purpose, as shown in Figure 2.1. Typically, the spatial encoding includes slice selection and both frequency and phase encoding. First, the spins in a sample need to be distinguished to enable slice selection. If a linear field gradient is added to the $\boldsymbol{B_0}$ field in one direction, for example z, the precession frequency of the spins will change in that direction. A selective RF pulse can now be configured, in shape and frequency, to excite a specific slice of the sample. In Figure 2.10 a) two possible slices, where protons precess at different Larmor frequencies, are shown. Since the NMR signal from the selected slice is a complex exponential, it can be spatially encoded while it is active by manipulating its frequency and its phase. With that purpose, two more gradients are added in the other two directions (x and y). Applying a linear gradient in the y direction will make the spins in that direction experience a different magnetic field and they will precess with different Larmor frequencies. After a certain time, a phase difference will be accumulated among them and the gradient is turned off as shown in Figure 2.10 (b). They will continue their precession around the z-axis at the frequency

they had before the gradient was applied (ω_0), but the phase of the signal will contain spatial information. This is called phase encoding. In this state, the spins aligned with the *x*-axis still have the same frequency. Thus, a new gradient must be added along the x-axis to make the Larmor frequency change in this direction. In consequence, this is called frequency encoding. The resultant NMR signal, which now is spatially encoded, can be processed to construct an MRI image by means of a 2D Fourier transform.

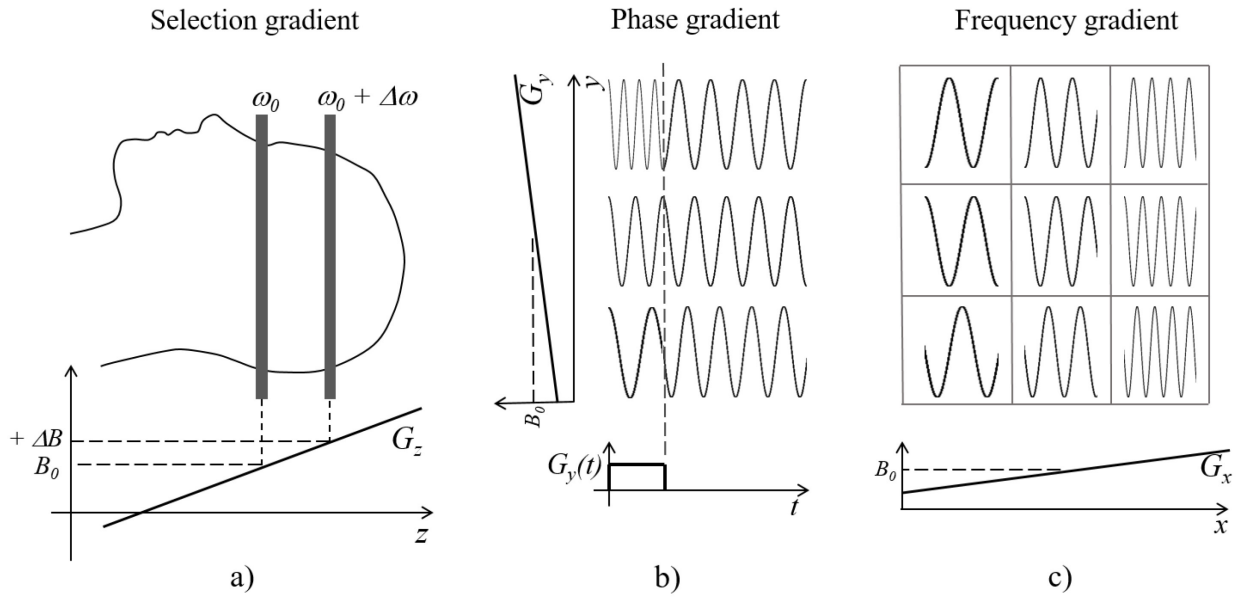

Figure 2.10 Spatial encoding. a) two possible selected slices on a human head having the Larmor frequency at the eyes and a higher frequency at the head. b) phase encoding reached by previously applying a time invariant frequency gradient $G_y(t)$. All signals start with the same phase but at the end of the pulse they have a different phase. c) 3 x 3 matrix representing one selected slice from a) (the one at ω_0) where the phase-encoded signals from b) are subsequently frequency-encoded by means of another time invariant frequency gradient ($G_x(t)$). Notice that each member of the matrix has a unique combination of phase and frequency.

The spatially encoded signal after detection can be expressed by [18]:

$$S(t) = \iint_{object} \rho(x,y)\, e^{i\gamma(G_x x + G_y y)t} dxdy \tag{2.24}$$

where $\rho(x,y)$ is a spin distribution and $G_x x$ and $G_y y$ are the linear gradient fields at x and y. This integral is over spatial dimensions only, so that the simple variable substitutions $k_x = (-\gamma G_x t/2\pi)$

and $k_y = (-\gamma G_y t/2\pi)$ can be made (for the FID). This transformation will map the time signal to the known *k*-space signal [18]. Thus:

$$S(k_x, k_y) = \iint_{object} \rho(x,y)\, e^{-i2\pi(k_x x + k_y y)} dxdy \tag{2.25}$$

x, k_x and *y,* k_y are then considered as the Fourier conjugate variables, as ω and *t*, which has the same structure as a 2D Fourier integral. Then, taking the inverse Fourier transform of the detected signal will give the solution for the spin distribution $\rho(x,y)$ [18]:

$$\rho(x,y) = FT^{-1}[S(k_x,k_y)] = \iint_{k-space} S(k_x,k_y)\, e^{i2\pi(k_x x + k_y y)} dk_x dk_y \tag{2.26}$$

In conclusion, when the inverse Fourier transform is applied to the raw data in *k*-space, an MRI image is obtained.

In general, not only constant gradients are used. They can also be a function of time, like a sinusoid for example. In those cases, the relationship between t and k should be written as: $k(t) = \frac{\gamma}{2\pi}\int_0^t G(\tau)d\tau$ [15].

2.2.6 Typical image acquisition sequence and k-space

Image sequences are composed by RF pulses and gradients conveniently combined to acquire images. The MR signals acquired with them are stored in *k*-space. One of the most important sequences, called Gradient Recalled Echo (GRE), is shown in Figure 2.11. In this sequence, the 180º RF pulse is replaced by gradient rephasing pulses. A 90º RF pulse and a slice selection gradient G_z are simultaneously applied to tip ***M*** at a *z* position to the transverse plane. The negative part of G_z is used to re-phase the nuclei in the *z* direction which were de-phased by the positive part of G_z. After the negative G_z, a phase encoding gradient G_y is applied (red in Figure 2.11). This creates a phase shift in the MR signal that is a function of the position in the *y*-direction. In *k*-space the magnetization is moved in the positive *k*-direction. A frequency or readout gradient, having a negative and a positive pulse, is applied after some delay (blue and green in Figure 2.11). The negative part (blue) is a previous compensation for the de-phasing that will create the positive part (green). The magnetization in k-space respectively moves to the negative *x* and to the positive *x*. As a result, the frequency of the MR signal is a function of the position in the *x*-direction. This gradient produces the echo signal as the transverse magnetization components re-phase gradually.

The sequence is repeated, changing the amplitude of the phase gradient on each step, to move the magnetization to a new line in *k*-space until it is completely swept. Each line of k-space is filled with a digitized echo. The echo signal is recorded in quadrature, so each *k*-space point (black dots) is a complex number that contains spatial frequency and phase information about every pixel in the final image. For that reason, the inverse Fourier transform can convert *k*-space data in an MRI image.

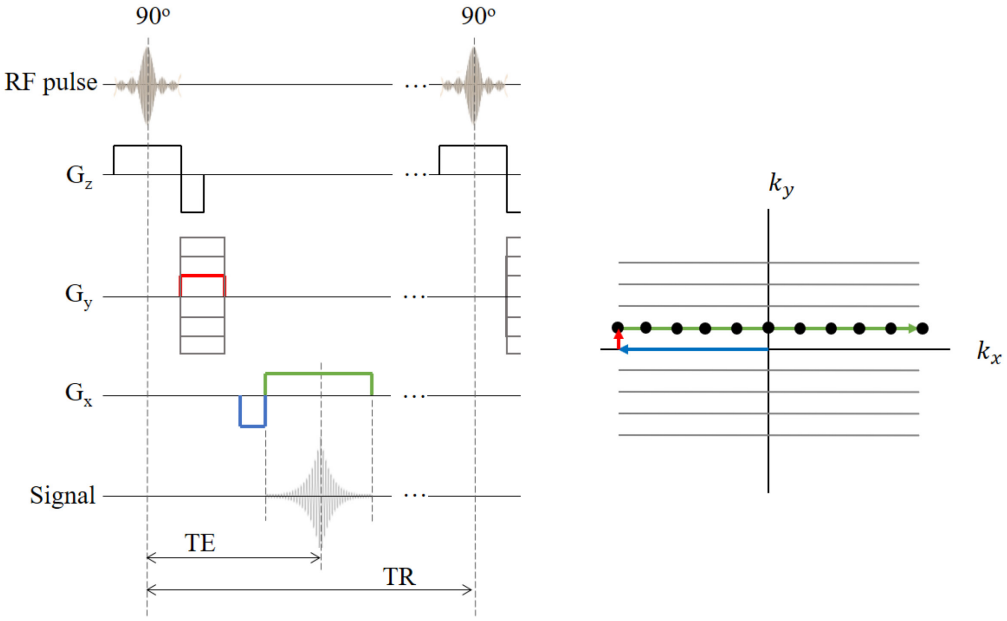

Figure 2.11 Diagram of the Gradient Recalled Echo (GRE) pulse sequence and the trajectory of the magnetization in *k*-space.

The parameters of this sequence, namely the echo time (TE) and the repetition time (TR), along with the flip angle, are adjusted to modify the contrast of the images. This sequence is frequently used with small flip angles to reduce the scan times.

2.2.7 Signal to noise ratio (SNR)

The SNR is a very important parameter of the MRI images. It is typically measured as the ratio of the pixel intensity, or the mean inside a region of interest, and the standard deviation of the background noise. However, different methods and corrections are used according to the receiver coil and the experiment setup. The noise in NMR signal comes from spontaneous fluctuations such as the thermal motion of free electrons inside the electrical components and the sample that is being

scanned. This noise can be modified in the subsequent processing, which will have an impact on the image noise [15].

The SNR of the NMR signal depends on several variables that can be related by the following expression [17], [19]:

$$SNR \propto \frac{\omega_0 B_0^2 K V_{sample} (B_1)_{xy}}{\sqrt{4k\Delta f \left(T_{coil} R_{coil} + T_{sample} R_{sample}\right)}} \tag{2.27}$$

where the numerator contains the signal-dependent variables and the denominator the noise-dependent variables. The signal depends on the static magnetic field B_0, the geometry of the coil (K factor), the volume of the sample (V_{sample}) and the B_1 components in the transverse plane (B_1^+ related to the excitation field and B_1^- related to the sensitivity of the coil). The noise depends on the reception bandwidth (Δf), the temperature and the resistance of the coil and the sample; k is the Boltzmann constant. The main contribution to the noise at low B_0 comes from R_{coil} while at higher fields it comes from R_{sample}. This is because R_{coil} is proportional to $\sqrt{\omega}$ due to the skin effect while R_{sample} is proportional to ω^2.

2.2.8 Parallel imaging

The increase in SNR achieved with a phased array coil can be used to reduce the scan time by means of parallel imaging techniques. These techniques take advantage of the differences in the sensitivities of the array elements to reconstruct the images with reduced data. These differences can be used to create a sensitivity map of the coil that allows to determine the origin of a signal. The number of phase-encoding steps (k-space lines) is reduced by simultaneously acquiring data from multiple receive elements. This leads to reduced scan time and aliased images. Several methods were proposed for reducing the Fourier encoding, being Sensitivity Encoding (SENSE) one of the most established [20]. In this method, the SNR is reduced by at least $\sqrt{R}$ due to the reduction of phase-encoding steps. R is defined as the factor by which the number of samples is reduced with respect to full Fourier encoding. Additional SNR losses are characterized by the g-factor (geometry factor) of the coil, which is always at least equal to one. The geometry factor describes the ability of the coil to separate pixels superimposed by aliasing. It allows a priori SNR estimates and provides an important criterion for the design of dedicated coil arrays since:

$$SNR_{\rho}^{red} = \frac{SNR_{\rho}^{full}}{g_{\rho}\sqrt{R}} \tag{2.28}$$

where ρ is the index of the voxel under consideration, $full$ denotes full Fourier encoding and red denotes reduced encoding.

2.3 Radiofrequency (RF) coils

As mentioned above RF coils can be divided in transmitter (Tx) coils, used to tip ***M*** from the z-axis, and receiver (Rx) coils, which are used to detect the signal induced by the precession of the spins. There is also a combination between them called transmitter/receiver (Tx/Rx) coils that is switched between both functions during the MRI experiment. Tx coils are desired to have a homogeneous $\boldsymbol{B_1}$ field while the Rx coils should have a high sensitivity and produce images with high SNR. The next sections will be focused mainly in surface Rx coils as they are the main topic of this work.

2.3.1 Coil model

An RF coil can be represented by a very simple series-resonant equivalent circuit, as shown in Figure 2.12. The resonance frequency of this circuit is the known expression: $\omega = 1/\sqrt{LC}$. The signal from the sample and the noise are represented by V_S and V_N. R includes the coil losses (R_{coil}) and the sample losses (R_{sample}). R_{coil} can be reduced by a proper selection of the coil materials and dimensions. R_{sample} is the equivalent series resistance due to the induced eddy current losses in the sample, which is a lossy conductor. It is related to the thermal motion of free electrons and it will always be present. Therefore, it is necessary to keep R_{coil} small compared to R_{sample} which leads to the condition called sample noise dominance.

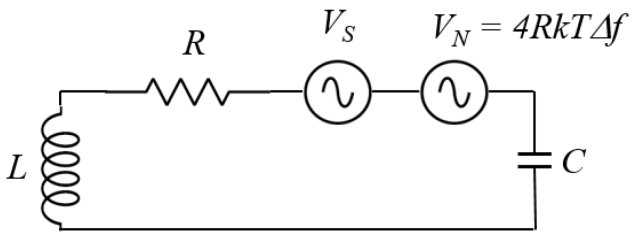

Figure 2.12 Equivalent circuit of a series tuned coil.

The quality factor Q is a very important parameter of this circuit. It relates the peak energy stored in the circuit reactance to the energy dissipated in its resistance during each oscillation cycle, or: $Q = \omega L/R$. It is directly linked to the bandwidth (Δf) of the resonant circuit at -3 dB by means of: $Q = f_0/\Delta f$.

2.3.2 Impedance matching

The impedance of the tuned coil is normally low as it is a series resonant circuit. It must be matched to the impedance required for the next stage. Usually it is a preamplifier that is designed to achieve its minimum noise figure (NF) for a certain source impedance. Most preamplifiers are designed for 50 Ohm but some of them can accept a range of source impedances with negligible degradation of the NF. In any case, it is important to respect the recommended values as this NF has the greatest contribution to the total NF of the receiver. Two distinctive tuning and matching networks are shown in Figure 2.13. After L and R are measured, for example with a network analyzer, the components for these networks can be easily found by using a Smith Chart tool. For the series resonant circuit, they can by calculated also by using the following expressions obtained from the electric circuit analysis:

$$C_2 = \frac{1}{2\omega R}\sqrt{1-(1-2R/R_L)^2} \qquad C_1 = \frac{1}{\omega^2 L-(1-R/R_L)/C_2} \tag{2.29}$$

For the parallel resonant the expressions are:

$$C_2 = \frac{1}{\sqrt{(Q\omega L-R_L)R_L\omega^2}} \qquad C_1 = \frac{QR_L\omega C_2-1}{QR_L\omega^3 C_2 L} \qquad Q = \omega L/R \tag{2.30}$$

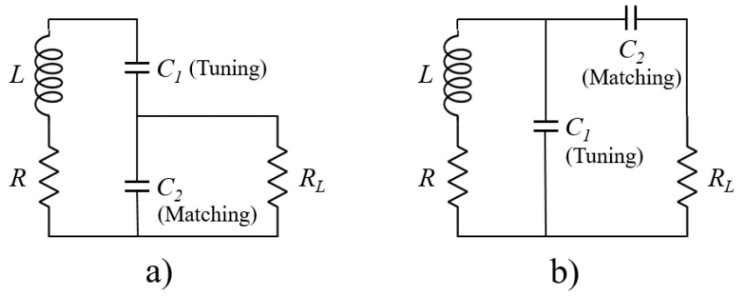

Figure 2.13 Series (a) and parallel (b) resonant circuits commonly used in RF coils. R_L is the source impedance required for noise match, usually 50 Ohm.

2.3.3 Detuning

RF Rx coils must be detuned when a separate Tx coil is used and vice versa. Since these coils are tuned at the same frequency, the Tx coil can induce high currents in the Rx coil during the excitation mode, which could destroy components designed for very weak signals. In addition, during reception, the noise amplified by the RF power amplifier could be transmitted to the receiver chain, contributing to a considerable amount of image noise. In the transmission mode, a non-detuned Rx coil can act as a magnifying glass and focus the electric field in small regions, causing burns in the biological tissue.

Parallel-resonant LC circuits are inserted in series with the coil loop, creating high impedance paths to the unwanted RF currents as they virtually open the loop. These circuits can be active or passive and they are tuned at the Larmor frequency. The active circuits are provided with PIN diodes that are switched on during the transmit mode by a DC bias current generated by the MRI control system and sent through the coil connection port [21], [22]. The passive circuits are automatically switched by the excitation pulses by means of anti-parallel diodes and are mostly used to act as a backup protection in case of active detuning failure [23], [22], [24]. The capacitors already connected in series with the loop are used to implement these techniques and only the diodes and an adjustable inductor are added. Fuses can also be added for increased protection.

2.3.4 Baluns

Common-mode currents that exist in the MRI systems generate unwanted coupling and heating among coils and cables, which produces image degradation and safety issues. To minimize these currents some types of baluns are used. The most common is made by winding a semi-rigid coaxial cable and resonating, at the Larmor frequency, the inductance formed by the external surface of the shield with a capacitor connected in parallel. This creates a common-mode choke that represents a high impedance for the common-mode current that circulates through the exterior of the cable, without affecting the differential RF signal that circulates inside the cable.

2.3.5 Surface coils

Surface coils are conductive loops that are tuned to the Larmor frequency by means of capacitors, as presented in Figure 2.13. The dimensions of the loops are selected according to the desired

penetration depth in the sample. The total length of the selected conductor should be short enough ($< \lambda/20$) to keep a nearly uniform current circulating on it at the Larmor frequency. Since the phase of the current will be fairly constant, very low field inhomogeneities will appear due to dephased contributions of different coil segments when the coil is in transmit mode [25]. The sensitivity of these coils is maximum at its surface and decreases rapidly along the perpendicular direction. It is also higher for smaller coils as illustrated in Figure 2.14. This characteristic makes them attractive for building arrays of small coils and, consequently, increase the SNR and the field-of-view (FOV) compared to single and volumetric coils.

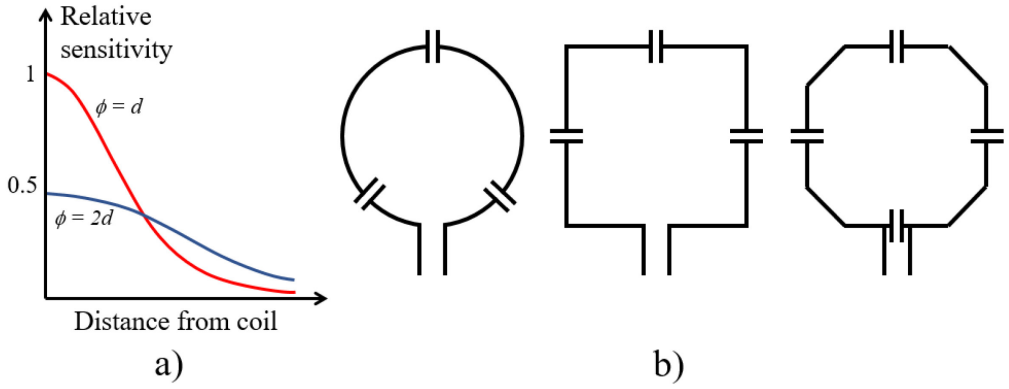

Figure 2.14 Surface coils and typical sensitivity. a) Relative sensitivity of two surface coils with different diameters (ϕ). b) A few common topologies used to build surface coils.

According to the principle of reciprocity, it is important to know the configuration of the magnetic field produced by the RF coil because it is related to its sensitivity pattern. This magnetic field is generated by contributions from all the conductive parts of the coil. The coil can be decomposed in elementary wire segments carrying currents (I) that generate magnetic field vectors ($d\boldsymbol{B}$) which can be added together based on the principle of superposition to find the total $\boldsymbol{B}$ at a point P:

$$\boldsymbol{B} = d\boldsymbol{B}_1 + d\boldsymbol{B}_2 \cdots + d\boldsymbol{B}_i \tag{2.31}$$

The contributions to the total magnetic field vector can be calculated by using the Biot-Savart law by [26]:

$$d\boldsymbol{B} = \frac{\mu_0}{4\pi} I \frac{d\boldsymbol{s} \times \boldsymbol{r}}{|r^3|} \tag{2.32}$$

where r is the distance from a small wire segment to the point P, $\boldsymbol{ds}$ is the unity vector parallel to the wire segment, $\boldsymbol{r}$ is the unity vector along the line described by r and $\mu_0 = 4\pi \times 10^{-7}$ is the permeability of the free space. The module of this expression is the contribution to the amplitude of the magnetic field:

$$dB = \frac{\mu_0}{4\pi} I \frac{|ds||r| \sin\theta}{|r^3|} \tag{2.33}$$

It is obvious that the magnetic field for a single point can be easily found when the involved geometries are simple. However, when the coils have a complex geometry, or when a field map must be created, it is advisable to use Computational Electromagnetics (CEM), which involves the use of computers to obtain numerical results to electromagnetic problems.

2.4 Receiver array coils

As presented in 1990 by Roemer and colleagues [8], a number of small surface coils can be arranged to acquire images of large regions of interest (ROI) as the thorax or the spine. This combination of coils is called array coil. It was demonstrated that an array can show improved performance compared to a unique surface coil that covers the same region. The NMR signal captured by each sub-coil or element, according to its sensitivity profile, is transmitted to a receiver channel of the scanner. All signals are afterward processed to reconstruct the image. If these sub-coils, that are all tuned at the same frequency (ω_0), were placed in a very close proximity, the mutual inductance among them would split their tuning frequencies creating multiple resonance peaks and reducing the sensitivity at the desired frequency. The resultant images would have reduced SNR and artifacts created by cancellation of signals. Therefore, each sub-coil must be decoupled from the others to prevent the loss of image quality. Two decoupling techniques that have been extensively used by array coil builders were also presented in Roemer's work, namely geometric decoupling and preamplifier decoupling.

2.4.1 Geometric decoupling

Well-designed RF coils exhibit a high sensitivity to magnetic field, which makes them susceptible to inductive coupling, as mentioned before. It was shown [8] that overlapping surface coils in a precise way reduces the mutual inductance to zero maximizing the decoupling between them.

Optimum distances between the centers of circular and squared loops, respectively related to the diameter and side length, were found in the cited work. They are reproduced in Figure 2.15 along with the magnetic flux lines corresponding to coil-1 that cross the internal area of coil-2. The current created by the flux that enters the plane of the coils is equal to the current created by the flux that comes out, and thus they cancel each other. This method is useful to decouple adjacent coils, but in an array, there is still some coupling between non-adjacent coils that must be minimized as well.

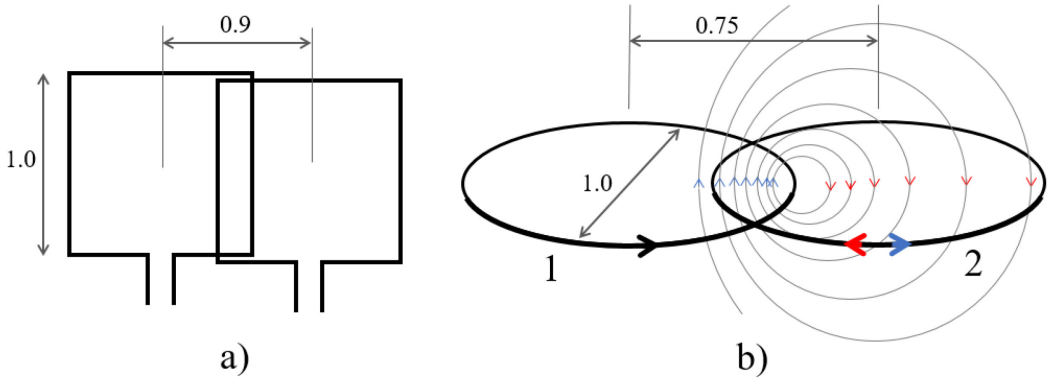

Figure 2.15 Critical overlapping for geometric decoupling between two squared (a) and circular (b) loops. The currents induced in coil 2 due to a current circulating in coil 1 are added in b). Notice that equal numbers of magnetic flux lines cross coil 2 in opposite directions, inducing equal currents that mutually cancel.

2.4.2 Preamplifier decoupling

This technique was proposed to reduce the coupling among coils that are not adjacent, since the geometric decoupling cannot be used [8]. It can be explained by using the simplified schematic presented in Figure 2.16. Coils 1 and 2 are both tuned to ω_0. A mutual inductance M exists between them so that a current circulating in coil 1 induces a current in coil 2. The coil 2 is connected to a preamplifier that has a very low input impedance R_P (≈ 1 Ohm). The preamplifier is designed to reach the lowest NF when the source impedance is 50 Ohm. C_T, C_M and L_M are selected to adapt the coil 2 to this impedance. If at the same time, C_M and L_M have the same reactance, they will be virtually connected in parallel by R_P. The resultant parallel-resonant circuit, which has a high impedance, is connected in series with coil 2, effectively blocking the current flow on it. The NMR signal can still be detected by the preamplifier as a voltage drop at the coil terminals. As a result,

the NMR signal coming from the region of the sample covered by coil 1 will induce a current on it but that current cannot induce any current in coil 2. In practice, all sub-coils in an array show the circuit of coil 2.

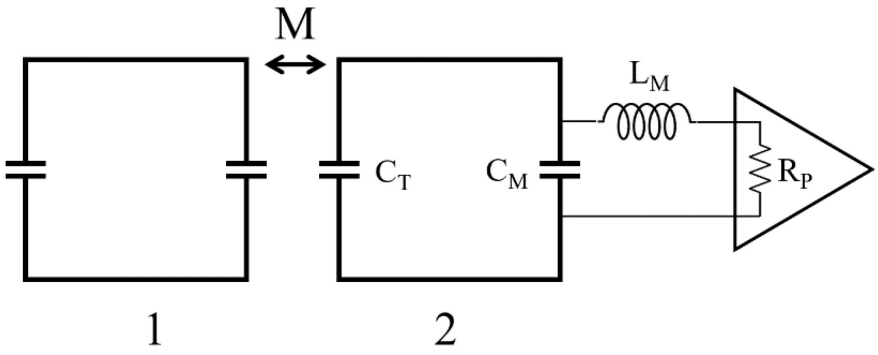

Figure 2.16 Simplified circuit that illustrates the principle of preamplifier decoupling, adapted from Roemer's work [8].

Having the preamplifier decoupling implemented, the Q of the loop is spoiled resulting in a bandwidth increase for the circuit. This is an advantage considering that a high Q circuit is potentially risky since a small detuning, which can easily occur just because of a load difference or a small coupling, can move the resonance peak and drastically reduce the sensitivity of the circuit. In terms of SNR this scenario is not desirable because the noise that is present at all frequencies is not affected. With the preamplifier decoupling, if the loop is detuned in a compratively significant range, the SNR is not affected. Nevertheless, care must be taken because a substantial detuning can take the preamplifier out of its noise match condition.

On the other hand, preamplifier decoupling must be carefully adjusted to have the best possible decoupling. Most preamplifiers include a high Q impedance transformer in the input circuit [27], [28]. The coil-transformer-preamplifier circuit must be provided with a means for tuning the preamplifier decoupling to the maximum value. A small frequency shift will considerably degrade decoupling. Also, any component added to this circuit, such as coaxial cables, cable traps, capacitors, etc., will damage its own Q in some degree and this in turn is going to degrade the decoupling. According to the latter, to reach the best decoupling, it is better to place the preamplifier as close as possible to the coil. However, this approach makes the circuit more potentially unstable.

2.5 Coil validation

2.5.1 Noise correlation matrix

When signals from the same region of the sample are received by more than one coil, as what happens in array coils, the image reconstructed by a combination of these signals may be affected if the noise voltages in the coils are correlated. The knowledge of the correlation of the total noise (from the sample and from the coil) between coil elements is important for the coil builder since it has a direct impact on the final image quality. It was demonstrated [29] that the total noise correlation between two coils can be deduced by measuring the cross talk between them in the presence of the loading. The following expressions were proposed to calculate the noise current correlation:

$$\langle i_1 i_2 \rangle = \alpha \cos\frac{\delta_T}{|Z_T|} \tag{2.34}$$

$$\langle i_1 i_2 \rangle = \alpha \, \mathbf{Re}\left(\frac{1}{Z_T}\right) \tag{2.35}$$

where i_1 and i_2 are the total noise currents induced in each coil, the diamond brackets mean the time average, $\alpha = 4kT\Delta f$, δ_T is the phase of Z_T, and Z_T is the mutual transfer impedance between the two coils. Thus, knowing Z_T is sufficient to deduct the noise correlation between two coils. This method eliminates the requirement of measuring the correlation on the noise itself. For an array coil a noise correlation matrix can be constructed by sequentially calculating the noise correlation between pairs of sub-coils.

Even though the arrays are designed for minimum coupling between channels, the situation may change when the samples are included. The sample can reduce the degree of decoupling between sub-coils and in consequence, increase the noise correlation.

A method for calculating the noise correlation matrix from the raw data acquired with a phased-array coil was proposed [30]. It is based on the calculation of the correlation between two elements of an M-channel array coil by means of the following expression [31]:

$$\rho_{ij} = \frac{\langle N_i N_j cos(\varphi_i - \varphi_j)\rangle}{\sqrt{\langle N_i^2\rangle\langle N_j^2\rangle}} \tag{2.36}$$

where N_i is the maximum noise amplitude if the noise voltage at point $\boldsymbol{r}$ is $e_i(\boldsymbol{r}) = N_i e^{j\varphi_{i(r)}}$. The angle $\varphi_i(\boldsymbol{r})$ is the angle between $\boldsymbol{B_1}$ and the $\boldsymbol{M}$ of the voxel at the point $\boldsymbol{r}$ for the coil i. Each ρ_{ij} is the ij^{th} element of the noise correlation matrix of the array. An acquisition with no RF power is performed and a noise correlation matrix is calculated after each phase encoding step. The statistical distribution of each matrix element, or correlation coefficient, is obtained from the ensemble of the matrices computed after all the phase encoding steps.

2.5.2 Image SNR calculation

Image SNR is a parameter related to clinical usefulness of MRI images and a sensitive measure of hardware performance. It can be used to compare the performance of two coils, among other evaluations of the MR system. Different methods were proposed to compute the SNR in MRI images. The choice depends on the type of coil, namely volumetric or surface coils, and single coils or arrays.

A series of test standards, developed by the medical diagnostic imaging industry to measure performance parameters that govern image quality of MRI systems, such as SNR, was established by the National Electrical Manufacturers Association (NEMA) [32], [33], [34]. The standards are intended for use by MRI system manufacturers, manufacturers of accessory equipment (including radiofrequency coils), and by MRI end users. The methods are designed to measure thermal and other broadband, non-structured noise.

The method recommended to determine the SNR of phased array coils by NEMA [32] is based in the method suggested for single surface coils [33]. The resulting SNR is a number determined by: $SNR = S/ImageNoise$. Correction factors according to the number of array channels that account for the noise distribution in array images are provided. Basically, for a single coil element, a signal measurement region at a selected distance (reference position) from the coil surface is defined. The region should be in the sensitive volume of the coil and inside the signal producing volume of a homogenous phantom. Ideally, the reference position shall approximate the position of the anatomical feature for which the coil is used or intended. A measurement region-of-interest

(MROI) of 7 x 7 pixel is selected around the reference position. The mean signal intensity value in this MROI shall be used as the numerator (*S*) of the SNR.

The image noise is determined by different methods. One method involves the acquisition of two consecutive images and the calculation of the pixel-by-pixel signed difference image. A noise evaluation area, which comprises the MROI plus at least 72 additional pixels, is defined in the difference image. The standard deviation (SD) of the pixels in that area is determined and the SNR is: $SNR = S\sqrt{2}/SD$. The $\sqrt{2}$ factor is introduced to correct the image noise estimation ($ImageNoise = SD/\sqrt{2}$), since the SD calculation is performed on an image than involves a difference operation. This procedure is valid, for both real and absolute value images, only when the noise is evaluated in those areas containing significant signal.

Another method to determine the image noise is performing only one acquisition and measuring SD of the noise contained in an area of the image without signal or artifacts. In magnitude images, the noise in regions with significant signal has a Gaussian distribution, while the noise in non-signal-containing areas has a Rayleigh distribution (a special case of the Rician distribution) [35]. The change of noise distribution must be compensated for, as the SNR measure ($SNR = S/ImageNoise$) assumes the noise is Gaussian distributed. For a single-channel system the correction factor is 0.655, leading to: $ImageNoise = SD/0.655$, as demonstrated before [36]. The SNR is then calculated by: $SNR = 0.655\ S/SD$.

When computing the noise standard deviation from multi-channel magnitude reconstructed images, a different correction factor is required to produce the appropriate equivalent Gaussian noise statistic, as the number of signal channels used to produce the magnitude image also alters the Rayleigh noise distribution [32]. The appropriate correction factors for multi-channel noise standard deviation computations were tabulated. For a 13-channel array, for example, the measured standard deviation of the rectified noise must be divided by a factor of 0.7 to derive the corrected standard deviation (symmetric normal distribution) of the noise. In consequence $SNR = 0.7\ S/SD$. For a 32-channel array the factor is 0.71 (see [32], Annex A).

An alternative calculation of the image noise levels was proposed [34]. Instead of using the standard deviation of a background region, the measured mean of the rectified noise in the exact same region (MROI) is computed on an image acquired with no RF excitation and an appropriate correction factor is applied. The image noise is then calculated by [34]: $ImageNoise =$

$Mean/1.253$. The correction factor 1.253, also derived in [36], is applied for a single coil. For images acquired with multi-channel arrays the correction factors were also tabulated ([32], Annex A). Thus, for a 13-channel array the factor is 5.05 and for a 32-channel array the factor is 7.97.

The comparison of phased array coils designed for different samples is complicated with the above-mentioned SNR methods since it is not possible to fix a single reference position that is appropriate for all array elements. In those cases, it is useful to compute a quantitative SNR map using direct measures of noise from each channel.

CHAPTER 3 LITERATURE REVIEW

3.1 Receive arrays, initial stages

This review is focused on the evolution, architecture, associated techniques and applications of MRI receiver array coils. The topic of the receiver arrays has been very active in the field of RF technology R&D for MRI. The constant development of new arrays with an increased number of elements has pushed forward the sensitivity of the scanners and contributed to considerably reduce scan times. The history of array coils was very well addressed elsewhere [37].

The receive array coils for MRI were introduced in 1990 by P. B. Roemer et al [8]. In their work, the first practical application of a simultaneous acquisition of signals, performed with an array of conveniently positioned surface coils, was presented. The authors obtained the high SNR of a small surface coil over a field of view that was normally associated with a volume coil, without increasing the scan time. To reach these results they reduced the interactions, or coupling, between elements by introducing techniques such as critical overlapping and preamplifier decoupling. They also proposed a methodology to maximize the image SNR, which was based on independently capturing and storing data from each coil and combining them, while introducing weights that depend on the location of each voxel in the ROI. For proving the methodology, they built two 4-channel arrays for the spine and obtained image SNR increases of 2 to 3 over a typical rectangular coil with similar dimensions, by means of various image reconstruction techniques. These ideas were quickly applied to designs with bigger numbers of elements and extended from relatively superficial regions, such as the spine, to more volumetric structures such as the head.

In an early application to volumetric regions, a 4-channel phased array, having two coils placed anteriorly and two posteriorly, was constructed and used to scan the human pelvis [38]. A significant improvement in SNR compared to other volumetric architectures was obtained. An extension of these experiments explored the influence of the relative orientation between the elements and the static magnetic field ($\boldsymbol{B_0}$) obtaining similar results [39]. The human head as a volumetric application was rapidly introduced [40]. A 4-channel phased array of surface coils was designed to scan the temporal lobes and was compared with a standard quadrature head coil. An improvement of 1.67 in SNR was obtained over the region of the hippocampus by using a phantom as a sample. In another extension of the ideas, a cardiac phased array coil that included a cylindrical

2-channel array placed on a human chest and a planar 2-channel array placed under the back, was introduced [41]. SNR on the heart region was improved by a factor of 1.1 to 2.85 over two commercially available planar coils: a flexible coil and a four-loop array. An improvement in terms of resolution was shown with a 2-channel phased array developed to obtain images of atherosclerotic plaques in the carotid artery [42]. The authors compared their array with a conventional single 3-inch surface coil obtaining an SNR that was 37% better.

The number of channels was increased to 16 in a cylindrical array for the brain that was built by creating a 2 x 8 grid of square elements on a cylinder surface [43]. Comparing it with a circularly polarized head coil of similar dimensions resulted in a SNR increase of nearly 3 in the proximities of its surface and a comparable SNR in the center of the ROI. Mutual coupling was minimized by combining overlapped elements and current-reducing matching networks. Data was acquired simultaneously from the 16 channels by means of a 4-channel receive system that was upgraded by multiplexing each channel in the time domain by a factor of 4.

3.2 Acceleration

The growth in the number of channels and its motivations will be reviewed later. It is convenient to summarize first another important line of research that was initially evolving in parallel: the reduction of scan time. This is the other important achievement in the MRI world whose introduction was facilitated by the array coils. It was called acceleration as it is the reduction of the total scan time, compared to what can be reached using conventional imaging sequences. Another benefit of faster acquisitions is the decrease of phase accumulation error during certain studies, which results in lesser image distortion. The MRI encoding process is shortened by using faster sequences combined with image reconstruction from under sampled k-space data. The price paid for the acceleration is an increase in complexity for image reconstruction and a decrease in SNR of the final image.

Some of the initial ideas on this area were only brought to the formulation or simulation stages because the technological conditions for the practical implementation were not created yet, i. e. the placement of an array of decoupled detectors around an object. In an early work [44] the author proposed a technique for reducing the number of phase-encoded spin echoes required for reconstructing an image by means of an algorithm based on multiple RF detectors. The additional information introduced because of the use of multiple coils was used as a part of the reconstruction.

Another work presented a theoretical imaging procedure to be used with multiple receiver coils [45]. The process avoided the sequential acquisition of signals from the individual coils, used at that time, with some advantages in terms of contrast and gradient requirements. One more method demonstrated by simulations that an image from an arbitrary body surrounded by an array of detectors could be obtained instantaneously without the need of pulsing gradients [46]. By calculating the induced current from each voxel over an array of detectors, the authors established a relationship between the set of signals and the structure of the body under investigation. They represented this relationship in matrix notation and inverted the matrix for creating an image of the body.

A method using a sub-encoding data acquisition scheme and a multiple element receive system was proposed and demonstrated [47]. In this method, the data was acquired with reduced phase encoding steps and the distance-dependent sensitivity information of each element was used to reconstruct the resulting aliased image. It was shown here that the reduction rate of data acquisition time was proportional to the number of elements.

A new method, named SiMultaneous Acquisition of Spatial Harmonics (SMASH), that took advantage of the spatial information inherent in the geometry of a surface coil array, to substitute for some of the phase encoding produced by magnetic field gradients, introduced a reduction in the image acquisition time over existing fast-imaging methods by an integer factor, without significantly sacrificing spatial resolution or SNR [48]. The method can be applied to many of the existing fast-imaging sequences and allows for partially parallel acquisitions. A 50% reduction in scan time was demonstrated using commercial phased arrays on two different MRI systems. It was also suggested that more reduction could be expected from optimized coil designs.

Another method called Sensitivity Encoding (SENSE) was presented [20]. It is based on the encoding effect that is generally added by the receiver sensitivity to the gradient encoding. The technique improved the MRI process in systems with array coils, since it considerably reduced scan time. The authors formulated the problem of image reconstruction from sensitivity-encoded data and solved it for arbitrary coil configurations and k-space sampling patterns.

Because of the impact of the results in both areas, RF instrumentation for MRI has evolved to a more complex architecture with a highly-parallelized receiver subsystem and more software

handling capability. Nowadays the majority of commercial MRI coils is composed of arrays, being the most common those with 16 and 32 channels [37].

Receiver parallelization has shown that SNR is enhanced with the increase in the number of array elements, compared to a volume coil or a single coil with the same dimensions than the array. Near the surface of the array the SNR is high because of the combined sensitivity of the small surface coils. At deep locations inside the imaged object the SNR is better, or not worse, because of an averaging effect that takes place when the data are phase-aligned and combined during the reconstruction process. In this region the SNR improvement compared to a single channel, can be more than 10 times for a 128-channel array [37].

The question of what could be the limits of parallelization led to further studies. A few works based on mathematical modeling and simulation tools, concerning the evaluation of the absolute performance of RF coil arrays in parallel MRI, were published [49], [50], [51], [52], [53]. The general result of these works is useful as a starting point to select the number of channels of an array, to compare coil arrays between them and to compare arrays with volume coils.

One of these works presented a method for determining the ultimate intrinsic SNR (uiSNR), or the highest SNR allowed by the electrodynamics of the signal detection process, when parallel reconstruction is used [49]. A complete set of basis functions, that satisfy Maxwell's equations within the sample, is used to express arbitrary coil sensitivities independently of any particular conductor arrangement and to perform PI reconstruction. The authors found inherent theoretical limits for acceleration in PI and provided a procedure for generating the optimal coil sensitivity pattern for a given acceleration.

A subsequent study revealed the same limitations [50]. The authors used a spherical model object and a set of basis sensitivity profiles, which are solutions of Maxwell’s equations for a sphere, to show that the behavior of the uiSNR imposes different limits on the acceleration rate in PI. They found that PI performance significantly improves from far-field wave behavior occurring at high field strengths and/or large object sizes and concluded that parallel techniques were promising for human MRI at very high field. In a posterior work the same authors demonstrated experimentally the fundamental benefits of far-field effects by investigating the dependence of parallel MRI performance on B_0 [51]. They later calculated the PI performance of model arrays consisting of a finite number (4, 8, 16, 32 and 64) of discrete, circular current distributions and compare them with

the theoretical SNR limits previously revealed [52]. As a result, they found that the uiSNR is most nearly achieved in the center of the sphere while at the periphery the sensitivity grows approximately linearly with the number of elements. They also found that for low B_0 (1.5 T) only 8 elements are needed to achieve the best possible reception in the center while at a higher B_0 (7.5 T) more coil elements are needed.

An algorithm to calculate the uiSNR was implemented to develop a tool for evaluating the absolute performance of array coils [53]. A spherical geometry was used again. Simulations on a 32-channel array were experimentally reproduced in a 2.98T system and results were compared. It was found that the highest performance is achieved in the non-accelerated case and a maximum of 85% of the uiSNR was observed with a phantom whose electrical properties did mimic the human brain. The performance was similar until 2x acceleration, but worsened at higher factors. This suggests that the number of elements should be higher for useful highly accelerated parallel images. The authors proposed their method as a tool for evaluating coil designs and to guide the development of original designs, which aim at approaching the optimal performance.

Other experimental works have shown the same SNR behavior. In one of them the authors have compared brain array coils with 12, 32 and 96 elements and revealed that a high SNR increase takes place in the distal cortex and a little gain is achieved in the brain center [54]. Another work compared a 32 and a 64 elements brain arrays built on the same former [55].

Other aspects, such as the noise that comes from the electronics, have to be taken into account to evaluate the performance of the array and to select the number of channels [52]. Clearly, if the level of this noise is significant, the array will be farther from reaching the uiSNR. A very important factor to define during the optimization of an array is the size of the array elements because it can define the noise contributions to the final SNR. This aspect will be reviewed later.

The influence of the patterns used for tiling the elements in the array on the performance of the coil in terms of SNR and acceleration, was studied [37]. By means of simulations, gapped and overlapped arrays with different number of elements, different accelerations and configurations were compared. In general, it was found that the gapped arrays had better SNR for 4x acceleration and low number of channels, as shown in previous works. On the other hand, for 32 channels or above, overlapped elements produced the highest SNR. Comparing only arrays with 32 elements, it was observed that for acceleration factors higher than 5 a gapped array in one direction showed

a better SNR than a completely overlapped array, although the difference was not considerable. These results suggest that with 32 elements and 4x acceleration it is possible to explore different tiling configurations without losing a considerable SNR performance. This could be used to search for a suitable mechanical configuration for the coil that could include adjustability.

3.3 Array components and design techniques

The following paragraphs will be dedicated to the main components of the array and the strategies used to provide decoupling between channels. Most of the MRI phased array coils with a large number of elements are an assembly of conductive loops. Other structures, such as microstrip and transverse electromagnetic (TEM) arrays, have been successfully used, mainly in very high B_0 fields where the wave length starts to be comparable to the coil dimensions [56], [57], [58], [59]. Nevertheless, the cylindrical geometry of these configurations causes them to have a lower SNR performance in the whole brain than arrays of conductive loops, closely distributed on the head surface and resembling a helmet. Since brain injuries are the motivations of this project, this review is mostly dedicated to arrays made of conductive loops.

A receive loop coil [60], [61] is intended to efficiently capture the high frequency oscillating magnetic flux produced by certain excited atomic nuclei that integrate the object under study. It is mainly built of a conductive material, as copper wire or copper foil, and other elements needed for tuning, matching and switching purposes such as capacitors, inductors and PIN diodes. All of them have resistive losses that determine the unloaded quality factor of the coil (Q_U), when added to the eddy current losses produced in metallic structures located in the proximities of the coil [62]. If a conductive body is placed near the coil, more losses will add to the circuit because of the eddy currents and displacement currents that circulate in it. These losses are added to the component losses to define the loaded quality factor of the coil (Q_L). The relationship between these factors (Q_U/Q_L) is an indicator of coil efficiency. It gives an idea of how much noise comes from the body and how much from the circuit. It can be used for determining if the noise coming from the components should be considered. It is always desirable to have body noise dominance because this noise is detected by the same mechanism that the useful signal. Thus, having more body noise means having more MR signal. This can be expressed by $R_L/R_O = Q_U/Q_L - 1$, where R_L represents the body noise and R_O the coil noise [17], [23].

Loop arrays combine the large field of view of the larger coils with the high SNR of smaller coils. Large loops have relatively more energy dissipated in the body than in the coil and are more efficient, while small loops have better SNR in their proximities [17] (see Figure 2.14a).

The effects on the SNR of the tuning capacitors, conductors, solder joints, eddy currents and the sample, were studied in overlapped array coils of different radius, from 40 to 400 MHz [63]. In this study, it was determined that copper wire and foil perform similarly, but copper foil in arrays has bigger eddy current losses. Tuning capacitance is commonly distributed in the loop instead of having a single capacitor. The authors have shown that using parallel capacitors for this, instead of single capacitors, minimizes the total losses from the tuning capacitors, increasing Q_L and Q_U, which might be expected. The electric field is concentrated near the distributed capacitors and is less coupled to the sample, which reduces the noise reception [17]. The gaps created in the metal reduce also the eddy currents. Therefore, the loop becomes less sensitive to loading changes, which makes the performance of the coil less dependent on the subject.

For the placement of the elements in the array the ideal condition is to reach the highest possible isolation between them. Although the use of some image reconstruction and hardware techniques can mitigate the effects of moderate decoupling, minimum mutual coupling between elements is in general beneficial. It is known from electric circuit theory that coupling between two coils tuned at the same frequency splits the resonance peak in two and reduces sensitivity at that frequency [8]. Matching is also made more difficult to reach so that part of the noise captured by the coil is reflected at the input of the preamplifier (connected at the coil output) and retransmitted back to other coils. This will obviously affect image SNR. The most common method for minimizing mutual inductance is known as critical overlapping [8]. It was described in 2.4.1. Other techniques based on the utilization of passive components such as capacitors and inductors were introduced [64], [65]. These techniques can be combined with critical overlapping and can be evaluated for applications involving complex geometries.

The MR signal captured by the coils must be amplified and transmitted to the receivers in the scanner. A network for impedance transformation is added to the loop circuit to connect it to the preamplifier, which is used subsequently to raise the signal level. The network configuration depends on the loop parameters, the loading and the preamplifier, among other practical considerations. It would be ideal to design this network for the best power match to the preamplifier

input, but for some preamplifiers this condition does not coincide with the best noise match condition. In these cases, the priority is to transform the impedance to the value the preamplifier requires to operate in its best noise condition, or minimum NF. As pointed before, this network is also used to implement the active decoupling, which adds some design complexity. In some cases, the elements of this network are involved in another important decoupling technique: the preamplifier decoupling, which was described in 2.4.2.

Different preamplifier designs are available for the coil builder. The input impedance can vary from very high to very low and sometimes including some reactive part, but the most common preamplifier has very low input impedance and a noise match near 50 Ohm. This configuration is more practical because of the 50 Ohm standard used for building coaxial cables, connectors and instruments. It also allows the design of very simple networks containing only one capacitor and one inductor to be used for active detuning and preamplifier decoupling purposes.

Descriptions of all these techniques can be found in several published works that contain the extensive experience of prestigious groups in the field of design and construction of array coils with a high number of channels [9], [37], [54], [55], [66], [67], [68], [69]. Almost all constructive details, from mechanics to final adjustments, were carefully explained in these works. Strategies, methodologies, materials and components, instrumentation and accessories, are also included. Comprehensive photographs and instrument screenshots that satisfactorily support descriptions were provided. A few details could not be evident for the beginner, but a more experienced designer can extract a complete methodology from these works.

3.4 Parallelization increase

The availability of all this information, the integration of more channels in the receive systems of all commercial scanners and the successful results of several research projects stimulated the interest for the high parallelization. Some works were extended to bigger number of channels or higher frequencies and new groups started working in this field of research. As an early example, a 16-channel array of gapped elements, designed to scan the human brain was built and compared to a birdcage [70]. Technical and practical feasibilities at 3T and a substantial increase in SNR for PI applications were demonstrated.

A new geometry combining pentagonal and hexagonal symmetries was introduced [66], [71]. 32 receive channels were arranged closely following the shape of the head. The elements were critically overlapped in the entire structure. The array was tested at 3T providing significant SNR improvements over commercially available head coils, including in the center of the head. In close agreement with [52] the authors found that PI performance was also improved, since they obtained different possibilities for reducing g-factor.

The rise of the number of channels was extended to 7T systems [72]. A 24-elements array of radially gapped columns of overlapped loops parallel to B_0 was built for the human brain and successfully tested for PI. This approach improved the solution presented by [70] where long thin elements had low coupling to the sample, high mutual inductance and significant electric field interactions that made less suitable at higher frequencies. This work was later brought to 32 channels with improved results [73].

In the first report found for pediatric brain applications, a 32-channel receiver coil constructed for a 3T scanner, is presented [74]. It was scaled from an adult head array and optimized for 4 years old children. Tests were made using a child's head shaped water phantom and a high-resolution anatomical imaging. SNR and g-factor maps were calculated for the phantom and compared to commercial Siemens 32-channel adult 3T head coil built with similar soccer ball design and a Siemens 12-channel adult head coil. Significant SNR and g-factor improvements were obtained demonstrating that close-fitting arrays are favorable for pediatric brain imaging.

A 32-channel array introducing substantial changes was developed and tested at 7T [75]. Preamplifiers were connected directly to the coil providing the array with a very strong preamplifier decoupling. The amount of conductive material was reduced using copper wire as in [54], elements were closely placed around a well-fitted former, as in [66] and [71], and multiple cable traps were inserted in the output coaxial cables. This configuration increased SNR, stability and isolation.

Motivated by [74], five 32-channel receive arrays were developed for pediatric brain imaging [9]. These coils were size-optimized for five age groups: neonates, 6 months old, 1, 4 and 7 years old. All arrays had the configuration used in [75], i. e., overlapped circular loops tiling a close fitting helmet. In this case, the helmet was divided in two sections to facilitate the placement of the subject. Also, the face was not totally covered, which made possible the use of visual stimulation for functional studies or anesthesia ventilation. The coils were evaluated in terms of SNR and noise

amplification for PI, using phantoms and volunteers, and later compared to a commercial 32-channel adult head coil and a pediatric birdcage. Results showed SNR and g-factor maps improvements in the whole brain. This demonstrated once again that a size-tailored approach could deliver significant sensitivity gains for accelerated and non-accelerated imaging, but in this case for the children's brain. Although a multiple arrays approach is not a practical solution for pediatric applications, as it requires hospitals to be equipped with multiple coils and to manually switch them based on the baby's head size, this well documented work is a good motivation for undertaking the development of an adjustable coil. This work was later extended to premature infants with the development of two 16-channel arrays with different sizes [10]. A 32-channel for term neonates was also developed. Again, SNR and g-factors of the arrays were compared to a standard adult head coil and results were consistent with the preceding work.

In a work focused on diffusion and functional spinal cord research studies at 3T a 32-element coil, that also covers the brain, was developed and successfully utilized [76]. The array includes a detachable paddle designed to cover the anterior part of the neck intended to improve the coverage in that region. The performance of the coil was assessed and compared with a commercial head-neck-spine array obtaining a twofold increase in image SNR and a g-factor reduction of 39% at 4x acceleration in the cervical spinal cord. Diffusion imaging of the spinal cord at 0.6 x 0.6 x 5mm resolution and tractography of the full brain and c-spine at 1.7-mm isotropic resolution were possible. This achievement offered the possibility of performing several enhanced basic and clinical research studies of the involved regions.

Some coils were constructed for exploring the potential capabilities of arrays with even larger number of elements. With that purpose a 90-element receive head array was constructed for a 1.5T clinical scanner [77]. The authors used the same geometrical structure proposed in another work done in parallel [71]. The scanner was modified for the experiments by adding and synchronizing two more 32-channel receiver racks. They evaluated the array in phantoms and humans performing SNR, g-factor, noise correlation and imaging measurements. As in previous results, the array in general provided significant SNR improvements over commercially available coils and allowed for high PI accelerations. The authors noted that in the center of the head the SNR was not improved compared to a 23-channel array constructed as a reference. They attributed this behavior to the small size of the elements, which led to a low Q_U/Q_L, and suggested some solutions.

The same authors later published a new work [54]. Here they increased the number of elements to 96 and the magnetic field to 3T. After several evaluations on the constructing material for the loop, number of tuning capacitors, etc., two additional improvements can be noted in the final design: the elements were built from copper wire and the preamplifiers were placed closer to the coils. Other designers quickly adopted both solutions. This prototype, like the previous one, was compared to an identically sized array with less channels (32 in this case), obtaining significant SNR improvements in the brain cortex while the sensitivity was not significantly lowered anywhere. On the other hand, PI behavior was significantly improved since g-factors for transverse accelerations were reduced. The coil builder could use this experience as a reference to assess, according to the needs of the project, whether it is worth facing such a challenging task. This work is also a motivation for exploring some areas into the array structure that could lead to further improvements, such as the structure of the loops.

Another array with 64 elements was designed for extending the coverage to the neck, the cervical spine and the face at 3T [78]. Its assessment proved that it was useful for brain studies and for exploring the head-neck-spine region. The same number of channels was later distributed around the head and the face by the same group of authors and for the same field [55]. Mechanical design included a split-former that partially overlapped both parts to allow the loops on them to be geometrically decoupled and facilitated workflow during scans. A 32-channel array was also constructed for comparison using the same former. Once again, it was proved that for accelerations of R = 3 or higher, g-factor was better in the brain center for the coil with higher number of channels and images were better in all regions in the head. Arrays with similar numbers of elements and others that have reached 128 were built for other body regions as for example the thorax [79], [80], [81], [82], [83], [84], [85].

3.5 Adjustable arrays

Adjustability is a feature that has been explored as well, since the variability of the body parts is substantial. Some arrays with geometries or shapes that can be changed depending on the sample size were published. The most important problem to solve in these arrays is the changing coupling between elements that affects also tuning and matching. Adjustability allows for optimization of the filling factor, among other benefits.

A geometrically adjustable 16-channel transceiver head array for 7T was presented [86]. The array was made of transmission line elements and capacitive decoupling. The introduction of decoupling capacitors, that automatically change capacitance depending on the distance between neighboring resonant elements, allowed adjusting the geometry between 22 and 26 cm in the anterior-posterior direction and between 16 and 21 cm in the left-right direction. The distance between elements is manually adjusted, which mechanically changes the decoupling capacitance at the same time. This keeps decoupling between elements in values below -14 dB. Preamplifier decoupling was not considered necessary with a convenient distribution of the shielding of the elements. However, the presented images exhibit non-uniformities, which could be caused by the lack of decoupling (-30 dB is recommended) in addition to the cylindrical structure of the coil. Compared to a similar but fixed array, improvements in SNR, PI performance and transmit efficiency were observed. The structure with variable capacitance presented here can be evaluated for using, in combination with other decoupling techniques, in arrays with better possibilities in terms of SNR.

Another transmitter/receiver array for 7T containing a 32-channel receive adjustable array was published [87]. The report is mainly focused on the transmitter section. The receive array was made of four separate segments that are closed around the head. Decoupling in each segment was reached by means of critical overlapping and preamplifier decoupling. On the other hand, decoupling between segments relayed only on preamplifier decoupling and values are not reported. The range of adjustability and the performance as a receiver coil are not mentioned and the physical volume of the complete coil is quite big which makes the approach impractical.

A different idea based on an adjustable head coil, consisting of interacting parts that can be displaced toward each other in a guided linear way by means of actuators, was presented [11]. It is unknown if any coil was constructed to demonstrate the possibilities of the method, but it might be used to build a neonatal coil. The inclusion of a pressure measuring system was recommended, as the use of motors or pistons as push-on elements may produce uncomfortable or dangerous pressure levels on the scanned head. This is a major concern in neonatal studies where the head is still very fragile and sensitive to external pressure.

Two works were presented by the GE Healthcare RF coils group. In one of them the design of a whole body coil for the 0 to 5-year-old population with 80-channel multiplexed to 32 output channels, called Pediatric Suite, is presented [14]. Adjustability is provided for the head and the

torso. The suite contains a 4-sections head array with 24 elements which deliver improved SNR compared to a commercial GE coil. Details about the method used to move the elements are not provided. The other project was named Adaptive Head Array (AHA) and it is intended for the population from 8 years old to any size adult male [12, 13]. It consists of four rigid plates populated with loop coils. 10 elements are placed in left and right plates, 6 in the front and back plates to conform a 32-channel array. The adjustability of this array is reached by moving the plates using actuators, such as motors and positive pressure pneumatic systems, presenting the already mentioned risks for the infant head. In addition, no evidence of the construction of this part has been presented. AHA is retractable for interventional applications and can also be rotated.

Other geometry-varying arrays for other body parts were presented. A modular system of individual surface coils [88] can be conveniently placed to create a receiver array, but the use of this approach in neonates can be difficult and time-consuming. Several known arrays can adapt by simpler operations to different body regions such as the wrist [89], the knee [90] and the pediatric body [91]. The cylindrical or conical geometries of these arrays are not optimum for the nearly spherical shape of the head. The same limitation is shown by flexible arrays [82], [85], [92], [93]. They have geometrical adaptability, but it is usually restricted to one direction in such a way that they can perfectly match regions with cylindrical or semi-cylindrical structures.

An 8-channel phased-array receive coil, adjustable to the width of the marmoset head, was also proposed to perform studies on a 9.4T small-animal scanner [94]. It is a part of a transmit/receive coil with fixed-size transmit coil. The receiver coil was constructed on a helmet formed to head of an adult marmoset. It was split into three sections joined by hinges, creating a semi-rigid structure. The eight elliptical elements were made of flexible PCB. Four elements have variable dimensions due to the inclusion of “pig tail” wire loops that bridge the gaps between sections, expanding and contracting when the helmet changes shape. Critical overlapping was used, when possible, to minimize decoupling. Results showed consistent SNR in the periphery of the brain between head sizes. When compared to a 15-channel, “one size fits all” receive coil, the adjustable coil achieved 57% higher SNR in the superior frontal and parietal cortices and 29% higher SNR in the center of the brain. This idea could be applicable to a human head, mainly if more sections and hinges are added due to the more spherical human head shape.

Printing techniques are also used to create flexible coils [95], [96], [97], [98]. Some results with up to only four channels were shown, with no flexibility improvement and with lower SNR compared

to other flexible coils. Stretchable coils [99] based in copper braids, as those used for coaxial cables, sewn onto an elastic fabric. The complete ensemble can be stretched to adapt to different knees, which can also be scanned in different flexion angles. A work aimed to investigate the potential image quality of stretchable loops was afterward presented [100]. Two conductors in a meandering and waving configurations, as suggested before [99], were mounted on a partially stretchable articulated material. The mechanical structure is quite complex, which could be the reason why only two loops in a nearly flat configuration were built. The image SNR was compared to a standard 2-channel coil reporting an average reduction of 10%. A patent including all these ideas was later filed [101]. Another stretchable array coil with a trellis-like structure, that can scale with the examined object, was proposed [102]. It has a cylindrical shape which can adapt in size while maintaining good tuning, match and decoupling. The coil shrinks in the longitudinal direction while its diameter increases and the overlapping between elements seems to remain approximately constant. These ideas present a high potential for head coil application if the challenge of adapting them to spherical shapes is overcome.

Only a few additional works dedicated to array coils for pediatric applications can be found. An investigation was made with the aim of finding if a phased array designed for highly accelerated PI of the pediatric torso enabled submillimeter resolution [103]. A 32-channel array for a 7-year-old child was built and SNR was reported as “acceptable”. Other work presented an 8-channel array for the pediatric elbow at 1.5T that was successfully compared to an available coil [104]. Another design for 1.5T, but for the spinal cord was built and validated with a 6 year old child [105].

3.6 Other materials

Another area of research that is actively explored nowadays is related to High-permittivity Materials (HPM). It is based in the use of dielectric pads with high permittivity with the aim of improving transmitter and receiver sensitivities. These pads can be conveniently designed and placed in the environment of the MRI coil, as a passive RF shimming, to modify the sensitivity pattern and, as a result, improve image quality [106], [107], [108], [109], [110]. It was suggested by these works that better images could be obtained by optimizing the location, geometry and material properties. Considerable research must still be conducted in this area. For example, it has to be found if a coil integrating HPM can outperform an optimized coil without HPM, or if the improvement is considerable enough to inspire its construction [111]. On the other hand, care must

be taken since certain variations in pad positions can lead to strong specific absorption rate (SAR) hotspots [112]. This is a safety issue that must be solved before these ideas become practical.

A similar approach is being investigated, but using structures called metamaterials. These structures are being explored mainly in high field MRI with the aim of manipulating the transmit RF magnetic field looking for a homogeneous excitation and SAR reduction. As an example, the use of a near-field imaging metamaterial device, known as magneto-inductive lens, was studied in a 1.5T PI experiment after some previous research [113], [114]. As an optical lens does, this lens can transfer the magnetic RF field generated by the MRI coil to locations placed on the opposite side. In this case, it consists of a pair of parallel 2D arrays of resonators, which are inductively coupled between them. The experiments shown that the SNR was improved in some areas of the image without losing PI performance compared to a conventional array. However, the penetration depth was similar with the lens than with the array alone. This result is equal to that obtained with an array of smaller elements directly placed on the sample, but the solution is less expensive as the number of preamplifiers and other components is considerably reduced.

3.7 Conclusions of the literature review

1. The development of an MRI head array coil for neonates which includes both, a high number of channels and some degree of adjustability, may improve the process of studying the neonatal brain in terms of scan time and SNR.
2. All presented solutions have some degree of drawback, suggesting that there is room for improvement.
3. The previous experience shown by several authors ensures, in a considerable degree, that this project is feasible.
4. A significant amount of applicable techniques, either proved or in progress, is available for experimentation. A few examples are the different decoupling methods (geometric, capacitive, shielded) and the new materials (HPM, metamaterials).
5. The scarcity of coil development projects for neonates, suggests that this age group is an additional challenge. For example, the compatibility of the coil with an incubator system needs to be considered.

CHAPTER 4 METHODS

The methods described below were used to develop an adjustable MRI receiver coil for the neonate head. However, they can be used as a guide to design coils for other size-varying body parts such as extremities, breast, neck and adult head or for non-human applications. Due to the larger dimensions of these parts and the less complex structures in some cases, the space available for placing pneumatic and supporting parts is bigger and the mechanical design can be simplified.

4.1 Array configuration

First, the dimensions of the intended biological samples were studied. In this case, an age group ranging from 24-week premature to 1.5-month-old was selected, based on the problem addressed by this project. The 50th percentile of the head circumference was used [115], [116]. Consequently, the adaptability range of the coil was chosen for nearly spherical loads from 8 to 12.5 cm in diameter. A space of 3 mm for padding was reserved in the largest (L) dimensions, as comfort is an important feature in these coils. After some design consideration, detailed in subsequent sections, it was decided to build an array comprising 13 loops. They were distributed on the surface of a truncated sphere with its vertical axis tilted 20^o from the z direction, which is the direction of the magnetic field $\boldsymbol{B_0}$, as shown in Figure 4.1. This configuration helps to better match the brain region and leave more space for possible use of ventilation tubes and anesthesia.

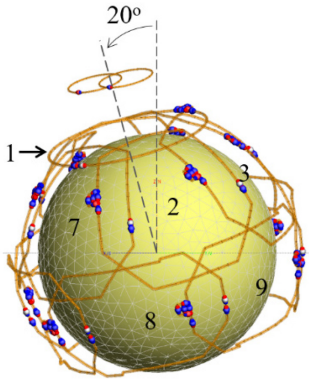

Figure 4.1 Array configuration loaded with a medium size spherical sample. Element 1 has a circular shape and is located at the top of the array. Elements 2 to 7, having a trapezoidal shape, are placed in the top row and elements 8 to 13, with a rectangular shape, make up the bottom row. Notice that the corners of elements 2 to 13 are chamfered. A decoupled double probe is shown on top of element 1.

4.2 Coil modeling and simulations

Given the current development achieved by computational electromagnetics, the engineers have a cost-effective alternative to mathematical analysis to obtain solutions whose accuracy is within the limits of experimental errors. The results are, anyway, later verified with experimental observations, as usually performed in the field of MRI coils development.

After the general idea of the coil was projected, the next step was to model it, taking advantage of the reliability of the currently available tools. In this project, this stage was crucial due to the complex and mobile structure of the proposed coil. Two conditions must be simultaneously satisfied in the complete adjustability range: an adequate performance of the coil and the non-existence of mechanical interferences among electric and mechanical parts. Not performing this stage could lead to several design-building iterations, which would be more time consuming.

4.2.1 Method selection

The commercial electromagnetic simulation software FEKO (Altair, MI, US) was used to create a realistic 3D model of the array and perform the simulations by preferably selecting a method that combines two full-wave, frequency domain methods: The Method of Moments and the Finite Element Method (MoM/FEM) [117], [118]. This hybrid method has proved to be accurate to simulate MRI coils, where the sizes of the studied objects (coils and samples) are small compared to the wavelength, mostly when the biological samples are inhomogeneous or have a complex geometry. The FEKO implementation was compared to other hybrid methods with very similar results [119] and later verified with two different MRI coils [120]. Its accuracy was also verified during the development of a birdcage transmitter/receiver coil designed and built for large rabbits, which have physical dimensions that are similar to those of the human neonates.

Full-wave methods approximate the Maxwell equations numerically, without performing any initial physical approximation and are very accurate [121]. In these techniques an unknown electromagnetic property is discretized, or meshed, typically the surface current for the MoM, and the electric field vector for the FEM. The studied geometry, including the radiating element and the surrounding media, is accordingly divided into a selected number of small elements. In the present work, the wire loops were divided in segments and the dielectric media in tetrahedrons. The meshing must guarantee that the phase is sampled adequately. In the case of MRI receive coil

arrays, where the total length of the conductor used for the loops is kept below λ/20, this requirement is naturally achieved since the phase change is kept very small. This reduction of the mesh improves the accuracy of the results. On the other hand, the element size cannot be reduced too much to avoid the increase of the computational load and the violation of the thin-wire assumption included in the MoM formulation.

Since the MRI experiment is a narrow bandwidth or resonance phenomenon, the frequency domain techniques, which find the solutions one frequency at a time, are a natural choice [117], [118]. In this work, most simulations were performed at the Larmor frequency or at discrete frequencies around it.

MoM/FEM takes advantage on the strength of each method, while avoiding their weaknesses. MoM is very efficient to simulate open boundary radiating wire antennas and curved metallic geometries, such as MRI coils, and FEM is very good for complex media, such as the conductive tissues of the biological samples. The hybridization of them fully accounts for the coupling between the MRI RF coil and the dielectric sample. The MoM is solved first and the resulting equivalent magnetic and electric currents are used as the radiation boundary of the FEM region [118], [122].

The MoM is an integral equations (IE) based method to compute electromagnetic fields in the frequency domain. The free-space region between structures and the boundary conditions are included in the formulation. This makes it a very efficient method as the space region around the radiator does not need to be meshed. In MoM, the radiating structure is replaced by equivalent currents, normally surface currents, that are discretized in wire segments (in the present case where wire loops are used). A matrix equation that represents the effect of every segment on every other segment is derived. This interaction is computed by using the Green function and applying the appropriate boundary condition, to generate a set of linear equations. The solution of this linear system gives the approximate current on each segment. The resulting matrix is populated with complex values [121]. After the currents are known, the loops parameters and the radiation patterns can be derived [117]. For homogeneous samples, such as phantoms with simple geometries, the MoM alone may provide an accurate solution.

The FEM is a partial differential equation (PDE) based method that starts with the partial differential equation form of the Maxwell equations [122]. The computational domain is first discretized into elements, as triangles for 2D modelling and tetrahedrons for 3D modelling, that

have nodes and edges. They are called finite elements. The distribution of the primary unknowns inside the elements is interpolated according to the values at the nodes or edges. The numerical solution corresponds to the values of the primary unknown quantities at the nodes or edges of the unit cells and it is obtained by solving a system of linear equations. This system of equations is formed by converting the governing differential equations and the associated boundary conditions into an integro-differential formulation, which is applied to each element to obtain a series of equations by using weights and interpolation functions. A global matrix system is then formed by assembling all elements and is solved by inversion or iterative techniques that represent the entire computational domain.

Several publications reporting extensive mathematical formulation, implementation and validation of these methods and the hybrid approaches are available [121], [123], [124], [125], [126]. For example, a general setup consisting of a metallic structure (MoM region *W*) and a possibly inhomogeneous medium (FEM region *V*) enclosed by a boundary region (FEM region *S*) is represented by the FEM and MoM matrix equations (see [123] for details). They are respectively:

$$[S]\{E\} + [B_s]\{J_s^{FEM}\} = \{0\} \tag{4.1}$$

$$[P]\{E_s^{MoM}\} + [Q]\{J_s^{MoM}\} = \{b\} \tag{4.2}$$

The MoM matrix does not consider the presence of metallic parts (free-space only), and:

$[S]$ is a sparse, symmetric, complex matrix with rank N_{FEM} (number of unknown field coefficients associated with the FEM region *V*).

$\{E\}$ is the vector of unknown electric field coefficients (size N_{FEM}).

$[B_s]$ is a sparse, complex matrix of rank N_s (number of unknown surface current coefficients on region *S*).

$\{J_s^{FEM}\}$ is the vector of unknown surface current coefficients (size N_s).

$[P]$ and $[Q]$ are dense, complex, nonsymmetric matrices of rank N_s (number of unknown electric field and surface current coefficients on region *S*).

$\{E_s^{MoM}\}$ is the vector of unknown electric field.

$\{J_s^{MoM}\}$ is the vector of unknown surface current coefficients.

$\{b\}$ is the excitation vector.

These equations can be solved simultaneously to obtain a complete field solution. The following boundary conditions must be applied on the region *S* to couple the two equations:

$$\boldsymbol{n} \times \boldsymbol{E}^{FEM}|_S = \boldsymbol{n} \times \boldsymbol{E}_S^{MoM} \tag{4.3}$$

$$\boldsymbol{J}_S^{FEM} = -\boldsymbol{J}_S^{MoM} \tag{4.4}$$

Then, by splitting the electric field in the FEM region into internal ($\boldsymbol{E}_v$) and boundary ($\boldsymbol{E}_s$) field coefficients, the FEM matrix equation () can be written as:

$$\begin{bmatrix} S_{vv} & S_{vs} \\ S_{sv} & S_{ss} \end{bmatrix} \begin{Bmatrix} E_v^{FEM} \\ E_S^{MoM} \end{Bmatrix} + \begin{bmatrix} \cdot & \cdot \\ \cdot & -B_{ss} \end{bmatrix} \begin{Bmatrix} \cdot \\ J_S^{MoM} \end{Bmatrix} = \{0\} \tag{4.5}$$

The MoM matrix equation, after the additional inclusion of the metallic parts can be written as:

$$\begin{bmatrix} \cdot & \cdot & \cdot \\ \cdot & P_{ss} & \cdot \\ \cdot & P_{ws} & \cdot \end{bmatrix} \begin{Bmatrix} \cdot \\ E_S^{MoM} \\ \cdot \end{Bmatrix} + \begin{bmatrix} \cdot & \cdot & \cdot \\ \cdot & Q_{ss} & Q_{sw} \\ \cdot & Q_{ws} & Q_{ww} \end{bmatrix} \begin{Bmatrix} \cdot \\ J_S^{MoM} \\ J_W^{MoM} \end{Bmatrix} = \begin{Bmatrix} \cdot \\ b_s \\ b_w \end{Bmatrix} \tag{4.6}$$

These two matrix equations with two sets of unknowns can now be solved simultaneously.

4.2.2 Coil modelling

Circular loops arranged in the well-known soccer-ball pattern [127] were used at the beginning for simplicity as shown in Figure 4.2. With the coil size range already selected, a starting condition to choose the dimensions of the loops was to establish the geometrical decoupling in the middle of the range. In consequence, the loops were outlined considering that the medium (M) size load has a diameter of 10.25 cm. They were modeled on a spherical surface with a larger diameter (11.8 cm) to leave some space to accommodate supporting structures and padding, and in addition, reduce capacitive loading. All the dimensions of the model were related to variables to facilitate the size adjustments of the coils.

The diameters of the loops were selected to obtain a good penetration depth, so that they were in the proximities of the radius of the sphere where they were outlined (≈ 5.9 cm). They were adjusted to find an initial arrangement having distances between loop centers according to previously measured geometrical decoupling configurations. As a result, the number of coil elements should be 13, distributed in two rows of six plus one on top. Initial tests to explore the adjustability range revealed that large gaps appeared between the circular loops when the coil was expanded to its largest dimensions, which could be a source of decreased image uniformity. It was also very

difficult to find a general structure that had no mechanical interference between loops in the whole coil size range. In addition, when the coil was reduced to the smallest dimensions, there was a lack of space to accommodate the mechanical parts. Besides those complications, a functional shape around the face region, in terms of access to the nose and mouth, was not possible with circular loops and the selected number of elements. These problems can be observed in Figure 4.2c.

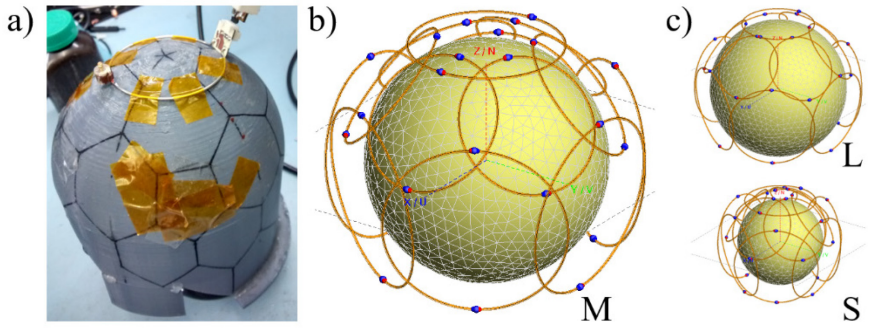

Figure 4.2 Initial coil model. a) Soccer-ball pattern drawn on a fixed-size helmet made for a 32-channer array where only one loop is placed. The other loops will be concentrically placed with the pentagons and hexagons. b) Isometric view of the initial array configuration made with circular loops. c) Array adjusted to the maximum and minimum sizes.

Accordingly, the loops were intuitively remodeled to better adapt the coil to a spherical load, such as a head, improve the coverage of the region of interest (the brain) in the complete coil size range and leave enough space for the mechanical parts. Three shapes were used: a circumference was kept for element 1, a trapezoid for elements 2 to 7 and a rectangle for elements 8 to 13. The elements 2 to 13 were curved to better adapt to the sample and improve the filling factor. Some corners were chamfered to reduce the total wire length and facilitate mechanical movements. The new configuration was performed with the medium size load and the overlapping area between adjacent loops was also intuitively formed. However, the coil was periodically adjusted through the complete range to verify that no mechanical interference arose between the loops.

The reshaping of the elements was performed with another condition: the loops should be still overlapped when the coil is adjusted to its largest (L) size. This would prevent (or reduce as much as possible) the gaps between the loops, which otherwise would decrease the image uniformity. To provide an idea, the minimum overlapping area was approximately 50 times smaller than the loop area, which should result in an S_{21} value of approximately -1 dB. The latter was defined by using as a reference a graph of magnetic coupling coefficient as a function of the separation of two

squared loops presented before [8]. The same S_{21} value (-1 dB) was selected to define the smallest (S) coil dimensions.

Other necessary parts were included in the model. A decoupled double probe, made of two geometrically decoupled non-tuned wire loops, was added to evaluate tuning and preamp decoupling in the same way it is performed on the workbench. A spherical loading sample with variable diameter was used to simulate the coil with different properties. The final setup is shown in Figure 4.1.

4.2.3 Electrical design

At this point it is convenient to add the electrical circuit to the model. Slightly different circuits were proposed to build the elements of a receiver array coil. Some modifications are introduced by the selected scanner, mainly because they have different methods to control the detuning of the coil during the transmit mode.

The schematic used in this work is shown in Figure 4.3. Several materials can be used to build the loops such as copper tape, wire, braid or tubing, printed circuit board (PCB) and high temperature superconductors. In this case a 16 AWG tinned copper wire was used, since it is not expensive, presents a high conductivity and it is easily malleable. In addition, it was proved that the cylindrical shape causes less eddy current losses and Q reduction in arrays [63].

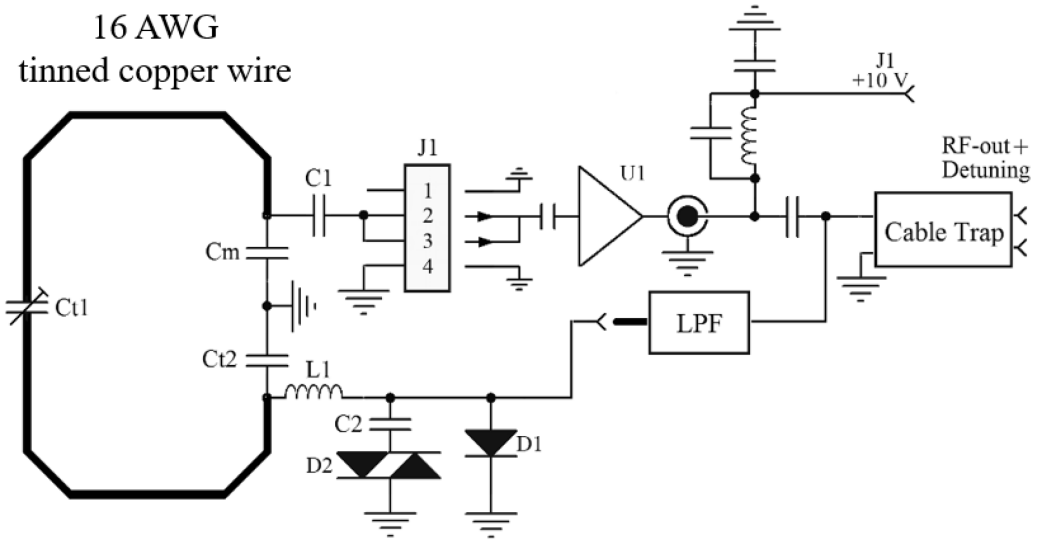

Figure 4.3 Electrical design selected for all coil elements.

The variable tuning capacitor (Ct1) is placed in the opposite side from the matching circuit. This position divides the loop in two equal and shorter segments, which increases the Q_U and reduces the antenna effect as the maximum total wire length can now be $\lambda/10$ [25]. The phase difference of the current circulating along the complete wire loop is now reduced and the field homogeneity is improved. This was also advisable, as the rule of keeping the wire length shorter than $\lambda/20$ at the Larmor frequency was not accomplished. A fixed tuning capacitor (Ct2), having the same value than the matching capacitor (Cm), provides the loop with electrical balance, which minimizes the antenna effect. This unwanted effect appears when the coil has one terminal connected to ground. In this case, the loop behaves as a small omnidirectional vertical antenna and the radiation resistance dominates the coil resistance. As a result, the Q_U factor and the SNR are reduced.

Ct2 and L1 are virtually connected in parallel to ground by a PIN diode (D1) (MA4P1250NM-1072T, MACOM, Lowell, MA, USA) to implement the active detuning. Likewise, an MRI switching diode module (D2) (UMX9989AP, Microsemi, Aliso Viejo, CA, USA) connected in series with a DC blocking capacitor (C2), are used for passive detuning. Ct2 and L1 must have the same reactance and in this case L1 is a handmade solenoid that can be manually tweaked to tune the circuit after the assembly.

A low input impedance preamplifier (U1) (MPB-127R73-90, Hi-Q.A. Inc., Carleton Place, ON, Canada) was selected after a comparative evaluation of another model. It is shown in Figure 4.4 along with the parameters and the electrical schematic. Notice that the input real impedance is 1.4 typical while the input reactance can be adjusted between +j12 and +j37. This means that it can be used to implement preamplifier decoupling, with the added advantage that it can be tuned by adjusting the variable capacitor included in the input circuit. The NF and the power consumption are low, and it is also specified that the amplifier was tested at 3T with properly loaded coils having a characteristic impedance of between 50 and 200 ohms with virtually no degradation in signal to noise ratio. The latter was considered to conveniently design the tuning/matching circuit. The preamplifier was directly connected to the loop in the matching board to prevent the addition of unwanted resistances that could degrade the preamplifier decoupling [128]. C1 is used to cancel part of the inductance introduced by the four-pin input connector (J1) and set the reactance of the input circuit to enable the fine-tuning of the preamplifier decoupling with the tuning elements integrated in the preamplifier.

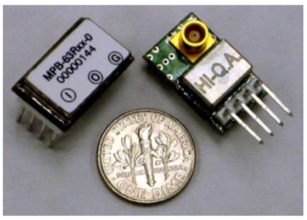

Electrical schematic

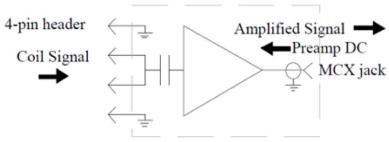

	G.E. 3T	Unit
Center Frequency	127.73	MHz
3dB Bandwidth	31±2	MHz
Phase Throughput	93±6	Degrees
Adjustable gain range (S21)	25 (min) to 32 (max)	dB
Input Z - Real (S11)	1.4 (typ) 1.6 (max)	Ohm
Input Z - Reactive Range (S11)	+j12 to +j37	Inductive Z
Output Return Loss (S22)	<-15	dB
Reverse Isolation (S12)	<-70	dB
Noise Figure	0.5 (typ) 0.55(max)	dB
O/P 1dB Compression Point	>+1	dBm
O/P 3rd Order Intercept Point*	>+13	dBm
Current Consumption	<8	mA
Supply Voltage	10 ± 1	VDC
Maximum RF Input Power **	+30	dBm

Figure 4.4 Selected preamplifier with electrical schematic and parameters.

A small shielded cable trap, made of 2.5 turns of semi-rigid coaxial cable (UT-047C, Micro-Coax, Pottstown, PA, US) wound on a small circuit board containing a 75pF capacitor, was inserted in the output coaxial cable to minimize common mode currents that have several adverse effects including the serious burns that they can cause in humans and animals. An elliptic low-pass T filter conducts the bias current to the PIN diode, while isolates the amplified magnetic resonance signal from the input circuit.

The designed PCBs are shown in Figure 4.5. The circuit was divided in two small boards (a). The matching/detuning board was designed in four versions (b) that would be used according to the position of the element with the aim of keeping the preamplifier aligned with the $\boldsymbol{B_0}$ field. The output board can be rotated with respect to the preamplifier as they are mechanically connected only by the MCX connector. This will add some freedom to place the parts in the array.

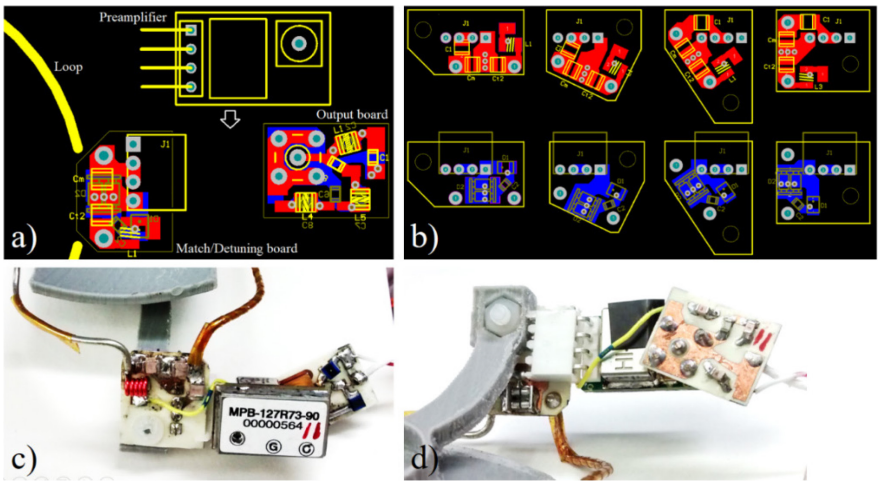

Figure 4.5 PCB design of the coil elements.

4.2.4 Simulations

Since the mutual distance among the loops is relatively small, the overall coupling in the coil should be strong. To reduce this coupling the first resource the coil builder has is the geometric decoupling technique. In consequence, the model was adjusted so that all adjacent elements were critically overlapped and the general coupling was studied.

The testing procedures, typically used in the workbench [67], were reproduced during the simulations to adjust the coil and obtain reference data for the subsequent bench tests. All tuning and matching components were represented by loads in the FEKO model as can be seen in Figure 4.1. A decoupled double probe was also modeled to measure tuning, loaded/unloaded Q, detuning and preamplifier decoupling. With illustrative purposes, Figure 4.6a shows one loop with all loads and the double probe.

4.2.4.1 Loop impedance measurement

The first step was to individually measure the impedance of the loops without any other component and all the other loops removed from the model. The load was the medium size sphere with $\varepsilon_r = 72.84$, $\sigma = 1.109$ S/m, which are the values of the solution used to fill the phantoms [129], [130].

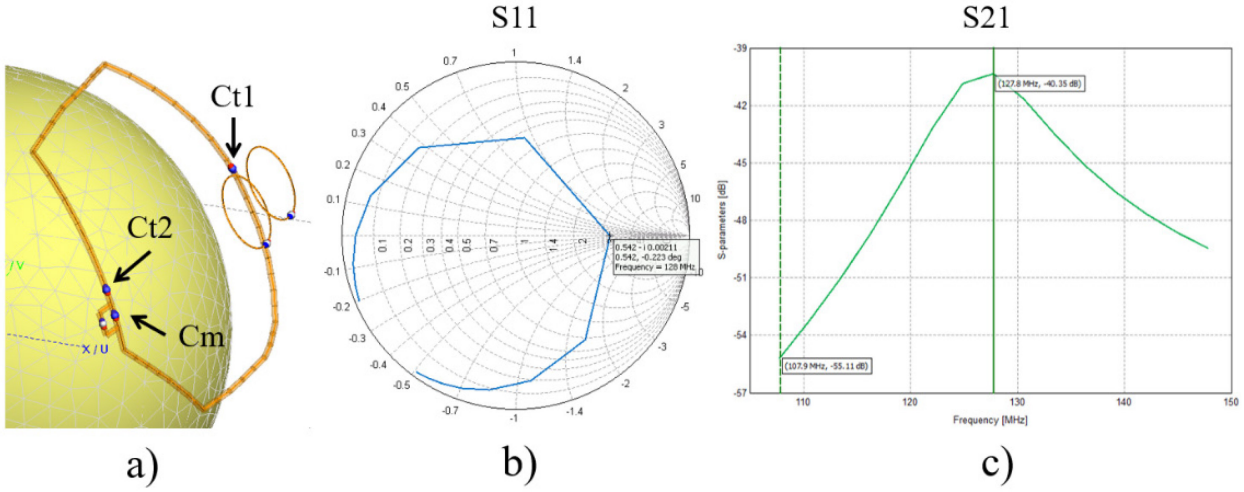

Figure 4.6 Loop test model, and tuning and matching curves. a) The ports and loads used for tuning/matching and a double probe on the M size load. b) The S_{11} parameter measured at the loop output. c) S_{21} measured between the double probes.

4.2.4.2 Tuning and matching

Having the impedance of the loops and using expressions (2.29), the initial values of the tuning and matching capacitors were calculated, since the circuit is the same as in Figure 2.13a. The obtained values were verified and readjusted with a Smith Chart tool. It is convenient to run an optimization search in FEKO to readjust the values to compensate for the addition of other parameters, as the equivalent series resistance (ESR) of the capacitors and the changes in structure, as the loop is now divided in two segments and balanced. All loops were matched to approximately 175 Ohm taking advantage of the possibilities offered by the selected preamplifier. It is common to use 50 Ohm as the noise match impedance, but increasing the value will reduce the matching capacitor and increase the Q of the detuning circuit, which increases the level of the preamplifier decoupling [54], [128]. As an example, the S parameters (loops 2-7) measured in FEKO are shown in Figure 4.6b, c.

The impedances of the tuned and matched loops were verified for all the other selected sample diameters to evaluate the magnitude of the change. Notice that all the adjustments were performed with the medium size load and the component values were kept during all the subsequent simulations (in the complete size range), as the array is intended to operate without any modification.

4.2.4.3 Active detuning

The active detuning function was introduced since it is useful to perform tests in isolated elements. For example, when all the loops are present in the array they introduce additional losses that produce changes in terms of tuning/matching, Q and coupling. To perform adjustments or measurements in individual loops it is important to detune the other elements. Active detuning was accomplished by adding an inductance in parallel with Ct2 in the same load. A variable that calculates the inductance according to the required value of Ct2 for the desired tuning/matching condition was also introduced.

4.2.4.4 Critical overlapping

It is a common practice to configure an array coil in such a way that all pairs of adjacent loops are geometrically decoupled. This technique has an important contribution to the general decoupling

in the array since most of the coupling is generated by the elements that are closer to each other. However, a few proposed arrays do not use this technique at all, or use partial critical overlapping.

To study the effectivity of this technique in the proposed array, the next step was to find the critical overlapping for geometrical decoupling. It was performed by measuring S_{21} between all possible pairs of adjacent elements. As before, the coil loading was the medium size sphere (10.25 cm). First, the loops 2 and 3 were adjusted by changing their dimensions in the horizontal direction until S_{21} was minimized. For doing this, the loops were vertically divided in two halves that were rotated around the *z* axis in opposite directions. The planes and the arrows in Figure 4.7a illustrate the splitting of the loops and the rotations respectively. Secondly, the adjusted loop 2 was used to find the critical overlapping with the loop 1. In this case, only the loop 1 was adjusted in diameter and height. The third step was to adjust the loops 8 and 9 by following the procedure used for loops 2 and 3. Finally, the loop 2, 8 and 9 were adjusted together. The loop 2 was not touched and the loops 8 and 9 were rotated around the center of the model, horizontally and vertically, to find the best possible decoupling between the three loops. The dimensions of the loops 8 and 9 were not changed. The rotation directions are shown with arrows in Figure 4.7b. After the dimensions were changed, all the loops were tuned and matched again to 175 Ohm which only required minor adjustments in Ct and Cm.

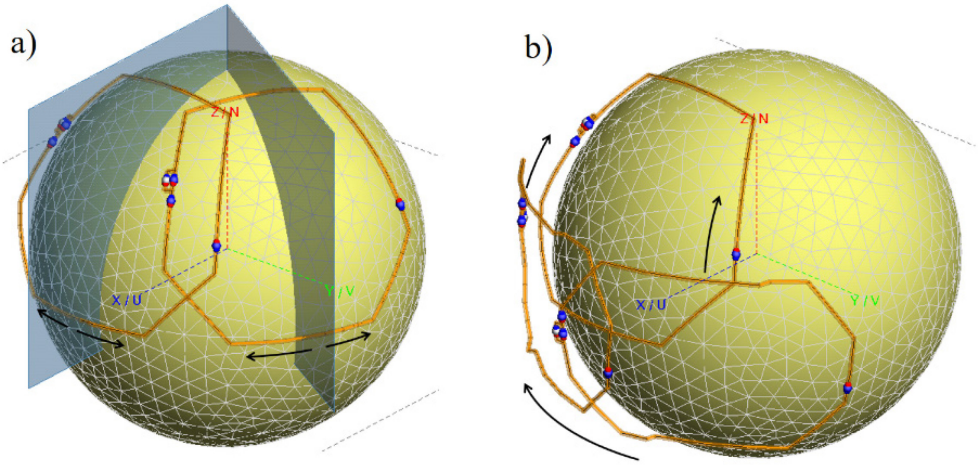

Figure 4.7 Some transformations performed on the loops to find the geometrical decoupling.

The complete array was afterward modeled with all the dimensions and positions and capacitances already found. These transformations can be seen in Figure 4.8 where the model after all adjacent elements were geometrically decoupled is compared to the initial model.

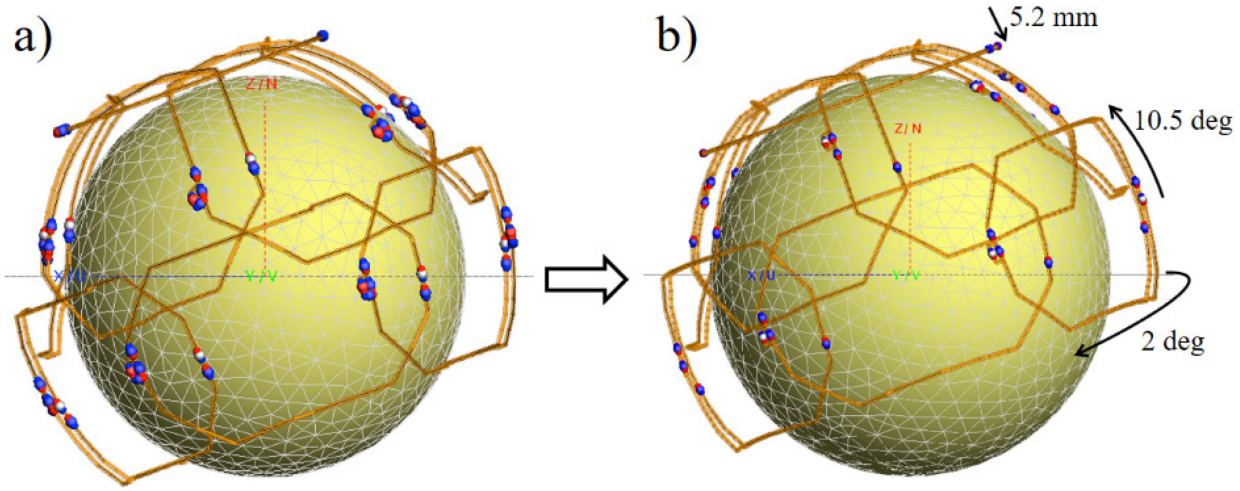

Figure 4.8 Simulated array before and after geometrical decoupling.

4.2.4.5 S-parameters matrix

An S-parameters matrix was created to allow a quick general notion about the overall decoupling in the array. This method was used to evaluate the array after different geometry changes that were required during the development process. For example, during the mechanical design the loops had to be displaced to create space for placing the preamplifiers, PCBs and other parts.

A multiport S-parameters request is initially performed in FEKO with all the loops tuned, i.e. the active detuning was not activated. All sources were matched to the output impedance of the loops, which is now very different to 175 Ohm due to the strong coupling that exists in these conditions. This must be performed to ensure that all the energy generated by the sources will be transferred to the loops, in other words: no reductions in S_{21} are caused by reflections at the loop inputs. On the bench, impedance transformers are added to pairs of loops to match them to the 50Ohm impedance of the network analyzer, while the others are detuned. For simplicity, in these simulations the impedance of each S-parameters source was matched to the real part of the impedance of the corresponding loop. A series load was added in the source circuit to cancel the remaining reactive part and complete the conjugate matching in each loop. This load was either an inductor or a capacitor as required. These actions minimized the reflections at the connection ports without introducing transformers.

To facilitate the task of building the matrix, a simple MATLAB code (Appendix A) was written to extract S_{21} parameters from the simulation output file and display an S-parameters matrix.

Five different load diameters were selected for the simulations: 8 cm, 9.1 cm, 10.25 cm, 11.4 cm and 12.5 cm. These values correspond to equally spaced circumference increments between the 50th percentiles of the 27-week premature and the 1.5-month-old infant.

4.2.4.6 Preamplifier decoupling

An equivalent circuit of the typical LC input transformer found in preamplifiers was also included in the model [28]. This transformer converts the output impedance of the loop ($R_{Loop} = 175$ Ohm in this case) to the impedance required by the first transistor of the preamplifier cascade to provide the lowest noise figure (NF). It is a series resonant circuit that performs as an impedance transformer when the components are calculated with the following expressions:

$$X_m = \sqrt{R_{Loop} R_{FET}} \quad , \quad C = 1/\omega_0 X_m \quad , \quad L = X_m/\omega_0 \tag{4.7}$$

Figure 4.9 shows the schematic of this circuit with the ports and loads used in FEKO. The reactance of the elements was 468 Ohm (L = 583 nH, C = 2.66 pf). To calculate these values, the equivalent noise input resistance of the first transistor in the preamplifier was assumed ($R_{FET} = 1250$ Ohm). The input impedance of the selected preamplifier ($R_{in} = 1.5$ Ohm) was taken from the datasheet. The effectiveness of this circuit was tested with the simulated double probe in the three types of loops. *Z-port* was short-circuited to perform the preamplifier decoupling test and used to measure the impedance of the tuned/matched loop when the preamplifier was not used. In the latter case the components of the preamplifier (C, L and R_{in}) were removed.

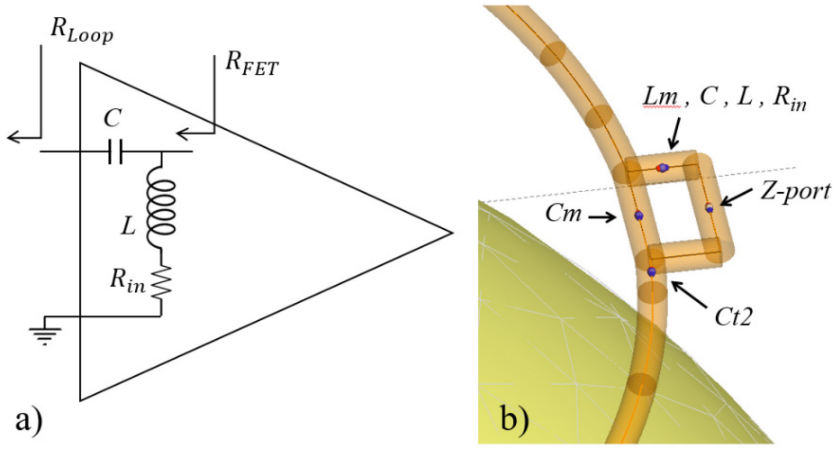

Figure 4.9 Model of the preamplifier. a) Schematic of the input transformer of a preamplifier. b) Ports and loads used in FEKO to model the preamp, shown here in loop-1.

The decoupling after the introduction of preamplifier decoupling was evaluated by using the same MATLAB codes used before to build the S-parameters matrices. For the simulations with the preamplifier models, two S-parameter ports were used in each channel. A low-impedance S-parameters port (n) was placed in series with the loop, near the variable tuning capacitor (Ct1). This port was set to active, which means it was a transmitter. The selected impedance was 0.02 Ohm to replace the equivalent series resistors (ESR) of Ct1. The other port (m), acting as a receiver, replaced the equivalent low-noise input resistance of the first transistor of the preamplifier (1250 Ohm), as represented in Figure 4.9b. The values of the tuning and matching components were kept unchanged, as normally performed during real bench tests when the preamplifiers are connected to the loops to assess preamplifier decoupling. Notice that an inductor (Lm) was included to complete the parallel resonant circuit that is created with Cm when the low impedance of the preamplifier is connected. As explained before, Lm has the same reactance than Cm at the Larmor frequency. Additional resistance that is present in the real circuit (due to connectors, solder joints, copper traces, possible coaxial cables, etc.) can be included in the same load, with C and Lm, to obtain a more accurate level of preamplifier decoupling.

To construct the S-parameters matrix, a modification was introduced in the MATLAB code. It consisted in a normalization to compensate for the mismatch between the active ports (n) and the loops (see Appendix A). As a result, the main diagonal of the matrix is full of zeroes. The other elements show how much power reaches every loop output (m ports) due to the current induced in each loop (n ports), considering that no loss occurs between the transmitter and receiver ports of each channel. Since all elements are very closely positioned, mainly for the smallest loads, this coupling is complex across the coil size range due to signal additions and cancellations.

4.2.4.7 Magnetic field simulations

Some initial magnetic field simulations were performed in FEKO to verify that the selected preamplifier models could minimize the coupling between array elements. For instance, a test was performed with two 4cm loops tuned and matched to 150 Ohm in a critical overlapping condition. The setup is shown in Figure 4.10. The first loop was fed with a matched source and the second one loaded with a matched load. A low intensity magnetic field was induced in the second loop as expected. The loops were then displaced to a high-coupling position and the magnetic field was simulated as a reference. Afterward, the second loop was provided with the model of the

preamplifier and the magnetic field was simulated again. Similar tests were performed with pairs of loops in the complete array adjusted to different sizes and the non-tested elements detuned.

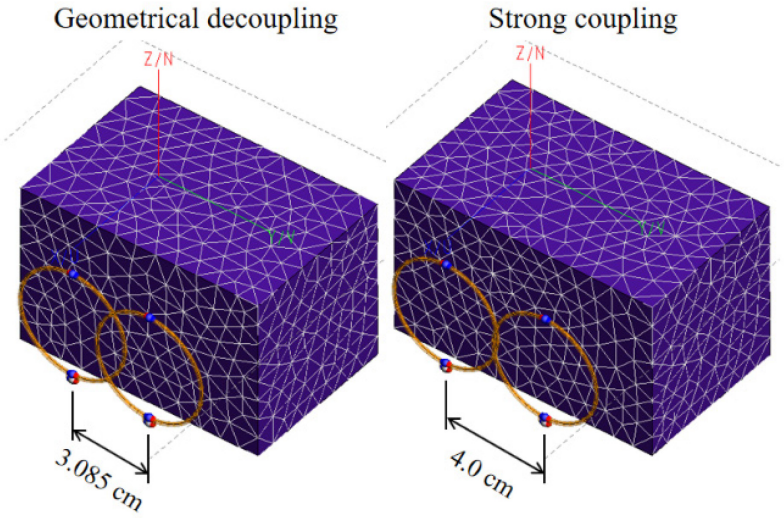

Figure 4.10 Decoupling evaluation by magnetic field simulations.

Magnetic field simulations were also performed in the complete array with and without the preamplifier circuit in all the channels, using the five selected dimensions. Field maps were created by using the MRI script (MRI quantities B_1^+, B_1^-, ratio and iSNR), which can be downloaded from the FEKO website [131]. Taking advantage of the principle of reciprocity, the array was simulated in transmission mode and all the loops were excited with sources with position related phases. Their voltages were adjusted to have the same magnetic field maximum magnitude in both conditions, without and with the preamplifier circuit. The real conditions were simulated by loading the terminals of the loops with 175 Ohm during the simulations without preamplifiers and with 1.5 Ohm during the simulations with the preamplifiers. The values of Ct, Cm and Lm, that were found when the loops were already mounted in the array, were used and not adjusted between tests.

4.3 Mechanical design and construction

4.3.1 Design

4.3.1.1 Array elements

The array of wire loops, in the geometrical decoupling configuration found in the simulations, was transferred to a mechanical design tool (AutoCAD, Autodesk, San Francisco, CA, US). The

associated circuits (matching/detuning board, preamplifier, and output/filter board) were conveniently placed and the supporting parts, including those of the pneumatic system were designed. It was not possible to find a mechanical structure with the geometrically decoupled configuration due to lack of space to place all the parts. Consequently, the positions of the loops were adjusted and new simulations were performed to evaluate the impact of the changes in the complete size range. Figure 4.11 shows the final configuration of the loop array in the medium (M) and the two extreme dimensions (S and L) with a small phantom. Notice that the bottom parts of the loops at the neck region were reformed for a better shape matching.

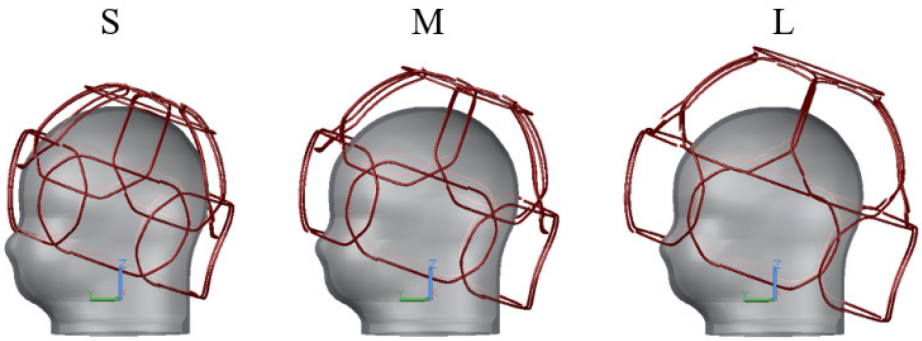

Figure 4.11 AutoCAD model of the loop array adjusted to the extreme and medium loads.

Individual mechanical supports were designed to attach the associated circuits to their corresponding loops. The element 12 is shown in Figure 4.12 with descriptive purpose, as any view of the complete array can be confusing. Each support has a unique design. Small differences among the supports of each row of elements (element 2 to 7 and 8 to 13) were required since the preamplifiers were aligned with $\boldsymbol{B_0}$, to avoid reductions in SNR, and the loop array is tilted 20º from that direction to facilitate the access to the mouth and nose of the patient.

Each support has three arms uniformly distributed around the loop center to hold the loops and other RF components. The main fixing point is a bolted joint between the matching/detuning board and one of the arms. The other two points are slots at the end of the other arms where the wire loop can be snapped. This facilitates the assembly and disassembly of the elements. The supports also contain sections of a fragmented spherical helmet whose diameter corresponds to the smallest coil size (S). The coil elements can move independently as no rigid mechanical connection exists between them. All elements are shown in Figure 4.13.

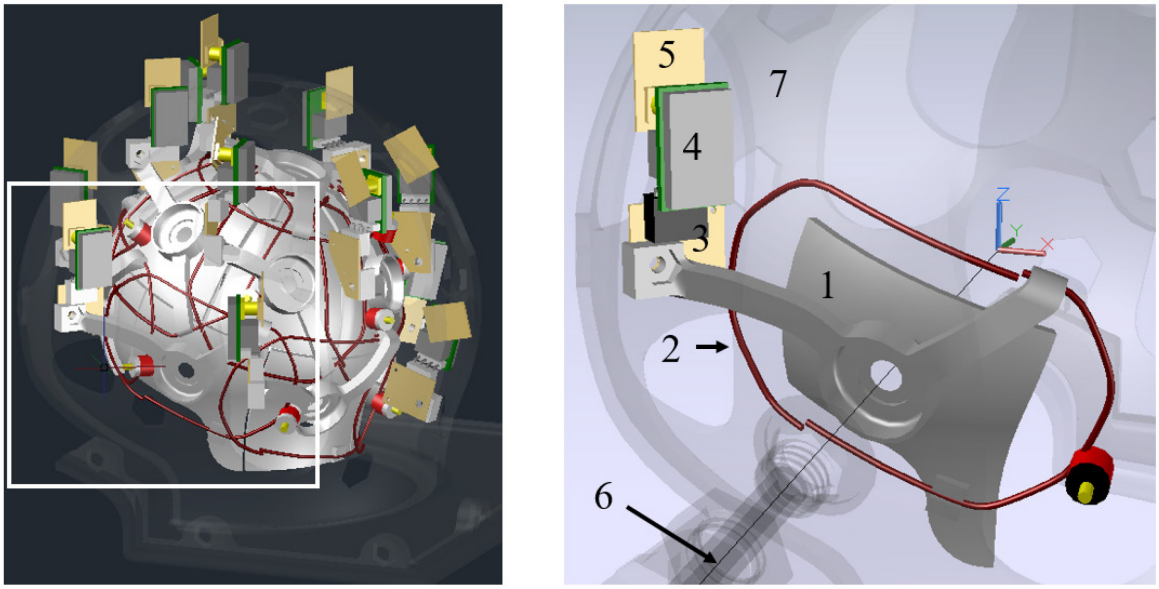

Figure 4.12 Partial AutoCAD 3D model of the coil. a) Adjustable helmet in the S dimension. Some parts are turned off to simplify the view. The section in the white square was magnified in b) and other parts were removed to show only the element 12. The coordinate system was placed in the geometrical center of the array, with the *z* axis in parallel with $\boldsymbol{B_0}$ field. The support (1) holds the wire loop (2) and the matching/detuning board (3) where the preamplifier (4) and the output/filter board (5) are plugged. Notice the alignment of the preamplifier with the *z* axis. The element will move along an axis starting from the coil center (6). A fixed-size spherical frame (7) surrounds the array of elements.

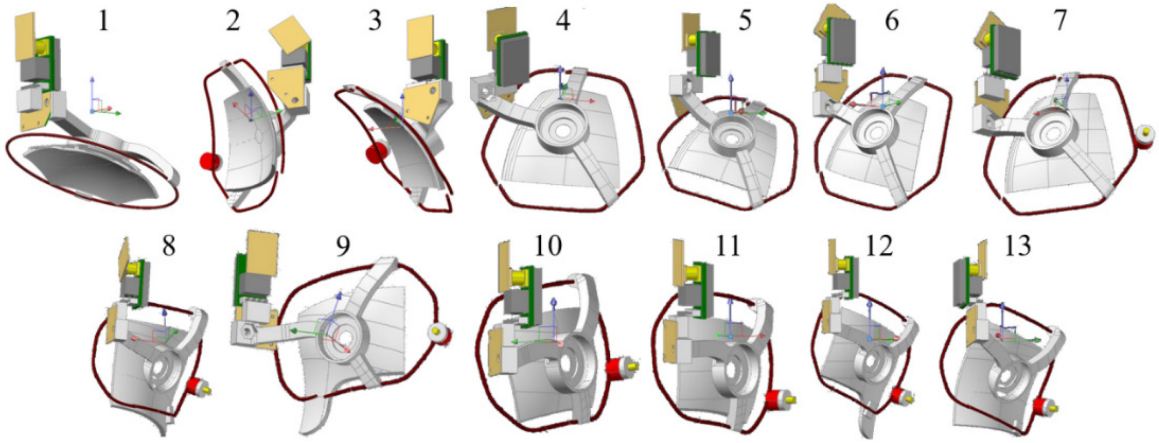

Figure 4.13 3D drawings of all coil elements.

A fixed-size spherical frame, with a helmet-like structure will serve as a base to support all the array elements. This helmet has holes for two purposes: to fix the elements and to allow the free displacement of them during the size adjustments. The free movement of the elements is illustrated in Figure 4.14. In this figure, one coil element (5) in the two extreme positions, is added to a view of the frame. Since the movement is rectilinear, no mechanical interference will occur between the element and the frame.

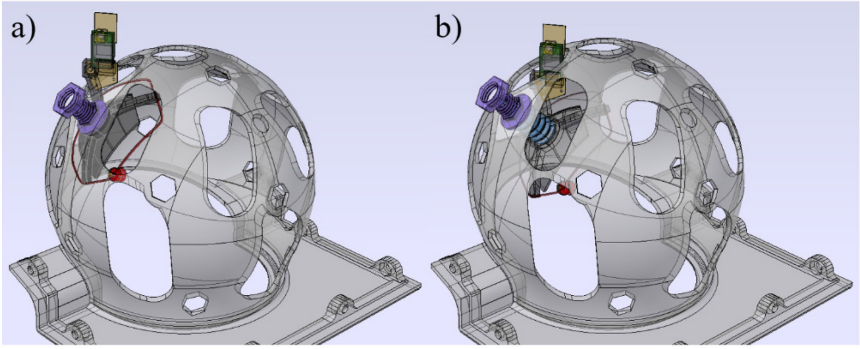

Figure 4.14 X-Ray view of the spherical frame. The element 5 is shown in the retracted (a) and the extended (b) positions.

4.3.1.2 Adjustability

The supports are joined to the spherical frame by a normally-extended plastic bellows. The bellows are accordion-like, flexible tubes with folds that expand and contract when the air pressure is changed inside them. These are very important parts in this design as they provide the coil with adaptability. The required performance of the bellows according to the intended application can be achieved by a custom design with an appropriate selection of parameters, such as the stiffness, flexibility, compressibility, memory, and travel. Some commercially available bellows, including those selected for this study are shown in Figure 4.15.

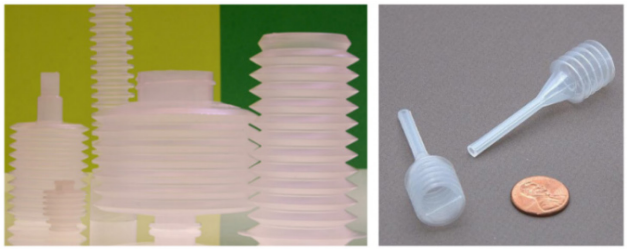

Figure 4.15 Different types of bellows. The parts shown on the right were used for this study as they are commercially available.

4.3.1.3 Pneumatic system

A PVC flexible tubing connected to a vacuum source interconnects all the bellows creating an airtight pneumatic system. A simple hand pump was used in this work since the amount of air that should be extracted from the system is less than 400 ml and the bellows are very flexible. The configuration of the pneumatic system is shown in Figure 4.16. Normally, all the bellows are extended, as the pneumatic system is at atmospheric pressure, and the coil dimensions are the smallest (S). Before placing a subject in the coil, negative pressure must be created in the system to compress all the bellows by means of the vacuum pump. As a result, all elements are pulled away from the coil center at the same time, in unique radial directions, expanding the space inside the coil. The pump handle needs to be pulled only once or twice to completely retract the elements. A check valve holds the vacuum inside the pneumatic system, keeping the coil expanded while the subject is accommodated.

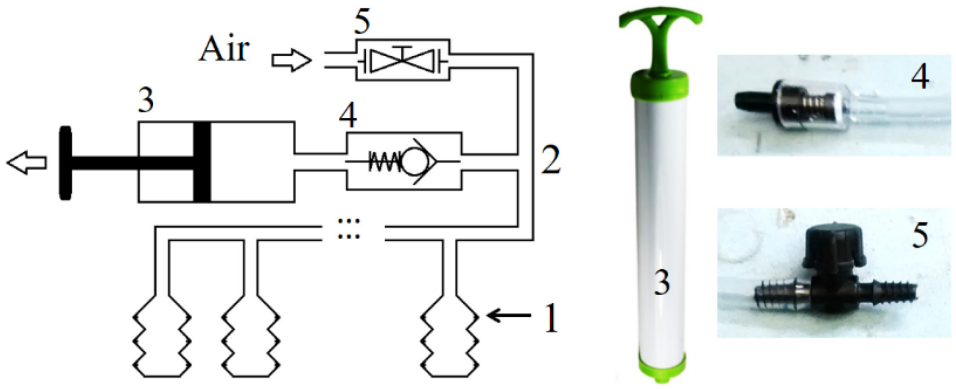

Figure 4.16 Pneumatic system used to move the array. The ensemble of the bellows (1) and the tubing (2) is connected to a vacuum source (3), which in this case was a hand pump. A check valve (4) retains the vacuum inside the system until a manually operated air valve (5) is open.

After the subject is placed in the coil, a pneumatic switch is manually opened to allow the system to return to atmospheric pressure. The coil elements are thus simultaneously and independently moved until they repose on the surface of the subject. In addition, since the bellows are flexible, each element has a relative freedom to tilt around its displacement axis. Thus, the adaptability of the coil increases as the elements adapt their final position to specific head sections, which are not perfectly spherical. The only force applied to the head comes from the intrinsic flexibility of the bellows, which is controlled by design. Figure 4.17 illustrates this movement.

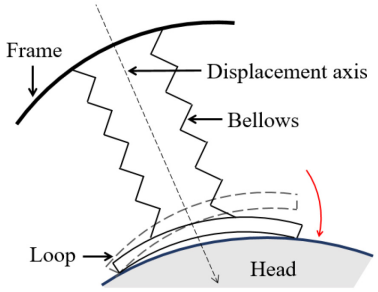

Figure 4.17 Illustration of the tilting movement described by the loops after they touch the surface of the sample. The loop will move parallel to the displacement axis (dashed lines) and will rotate (red arrow) to adapt the head shape.

4.3.1.4 Patient table

Since the dimensions of the coil are adjustable and some discomfort can arise from the back elements touching the back of the head or neck, the patient bed is designed to completely hold the patient. In this way, no body part of the patient will rest on the coil. Consequently, the bed is also provided with a head support that allows to initially place the patient in the bed and then slide the coil, while expanded, from behind. To compensate for the change in coil diameter the bed is provided with a mechanism for height adjustability. Since several very well-known mechanisms have been proposed with this purpose, the design of this part was left outside of this study. A 3D drawing of the external view of the coil with the maximum dimensions and illustrative details of the bed-coil setup are shown in Figure 4.18. The external dimensions were selected to enable the use of the coil inside an MRI compatible incubator.

4.3.1.5 Phantoms

A phantom was designed to perform the tests of the loaded coil. The selected shape was an average of different baby head shapes that results in a geometry mainly formed by the union of two different spheres with diameters $d_2 = 1.15\ d_1$, as shown in Figure 4.19. The model was designed for the medium (M) size coil dimension and scaled to the smallest (S) and largest (L) dimensions. It is made of two parts: the head and a base. The base has a threaded hole that will be used to fill the phantom. The circumferences of the head part of the phantoms are equal to the perimeters of spheres whose diameters are 8, 10 and 12.5 cm.

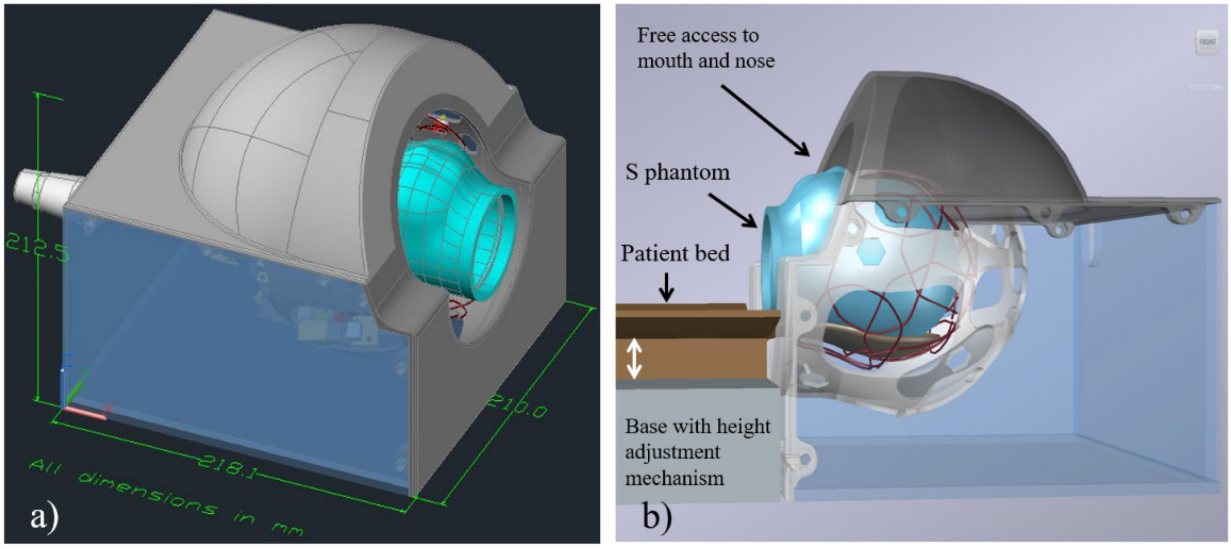

Figure 4.18 External view of the 3D model of the coil. a) Housing with maximum dimensions. b) Detail of the bed holding a phantom (S). Some parts are transparent and other are removed for clarity. The height of the bed can be adjusted (white arrows) according to the size of the patient.

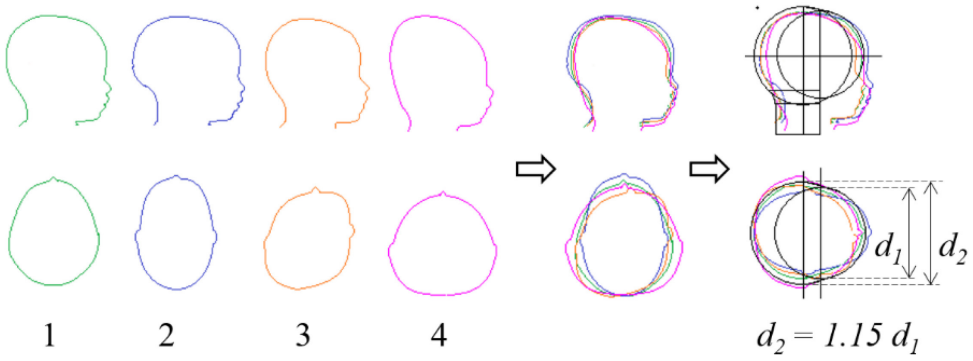

Figure 4.19 Steps followed to select the shape of the phantom. The final shape was similar to the normocephalic head (1), which is the medical term used for babies with normal head dimensions and proportions.

4.3.2 Fabrication

On-site 3D printing technology (Big Builder, Code-p West B. V., The Netherlands) was used to build most coil parts and phantoms with polylactic acid (PLA) material. A few of these parts are shown in Figure 4.20. The main part of the coil housing was made of 5.5mm laser-cut acrylic glass sheets, which were glued together, to strengthen the structure. The cover was 3D printed due to its more complex structure. A picture of the empty housing is presented in Figure 4.21.

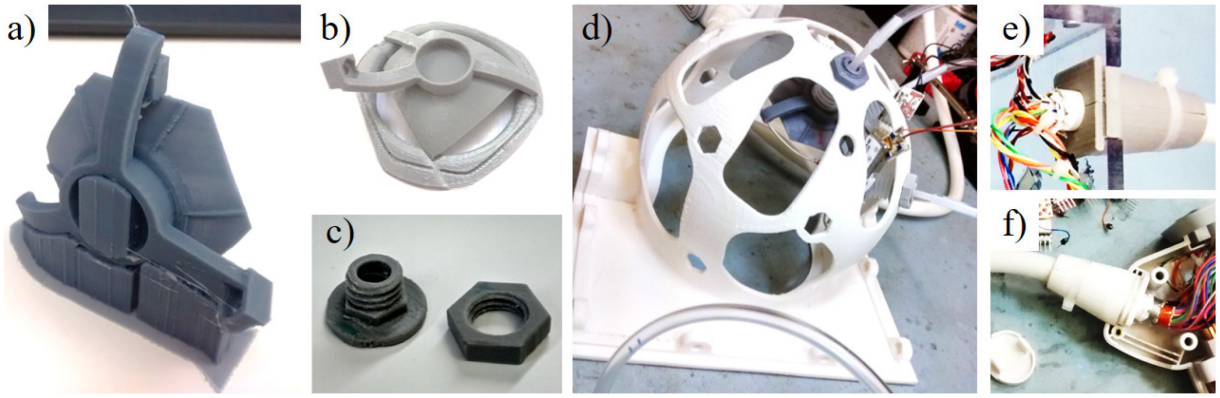

Figure 4.20 Printed plastic parts. a) Element 1 after printing with the required supports. b) Element 3 on top of one of the three molds printed to shape the wires (loops 2 to 7 in this case). c) Hollow screw and nut used to fix the bellows to the spherical frame. d) Spherical frame with three elements already mounted. e, f) Strain reliefs used to protect the cable and reinforce the attachment to the coil housing and the P connector.

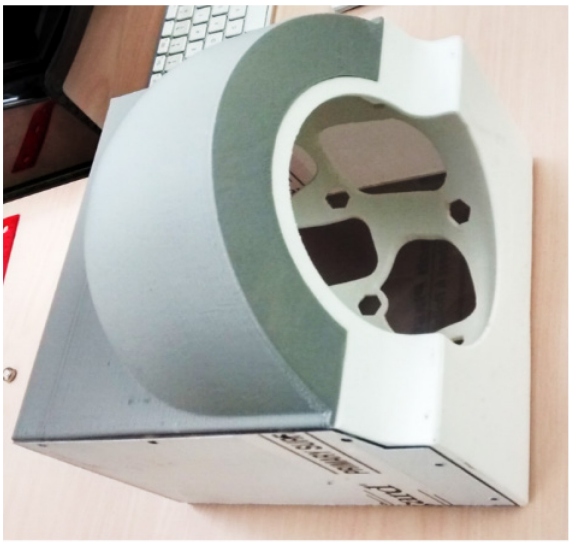

Figure 4.21 Picture of the coil housing with the spherical frame, which is also a part of the external assembly.

Three phantoms with the selected dimensions were printed, waterproofed and filled with a solution containing 3.75 g of NiSO4 x 6H2O + 5g of NaCl per 1000 ml of distilled water (ε_r = 72.84, σ = 1.109 S/m at 3T) [129], [130]. Figure 4.22 shows a picture of these phantoms. A spherical phantom being 10 cm in diameter was used during the preliminary bench tests and scans.

Figure 4.22 Set of phantoms used to test the coil.

4.3.3 Coil assembly

The first step was to build the loops by using the molds (Figure 4.20b) to ensure a good accuracy in terms of shape and dimensions. The goal was to minimize the mechanical interactions between adjacent loops and keep the parameters of the electrical design as close as possible to the simulated model. Then, each loop is soldered to the matching/detuning board and the ensemble of both parts is attached to the support, as shown in Figure 4.23.

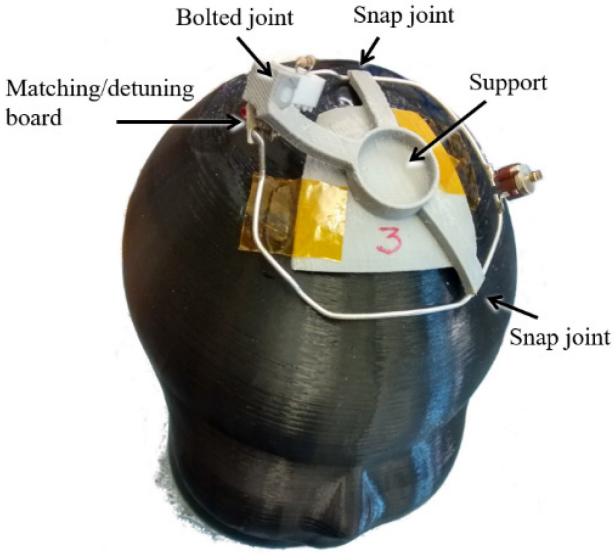

Figure 4.23 Part of element 3 containing the loop soldered to the matching/detuning board and both attached to the support. The three fixing joints are shown.

The other components (tuning/matching capacitors and detuning components) were mounted after the inductance and the quality factors are measured. All loops were subsequently tuned by placing them directly on the M phantom as a load and other tests, that will be detailed in a subsequent section, were performed.

The output boards were subsequently assembled and connected to the coil multiway cable through the cable traps as can be seen in Figure 4.24. Some tests can now be performed such as adjusting and measuring the preamplifier decoupling and the frequency response of the preamplifier, as the preamplifiers can be fed from a designed and constructed test box.

The next step is to complete the assembly of the elements by installing the bellows and attaching them to the spherical frame, as it is presented in Figure 4.25. The bellows are glued to the hollow screws and attached to the supports by a bolted joint. The inclusion of the latter simplified the assembly/disassembly process. The element 1 was mounted first, then the elements 2 to 7 and finally the elements 8 to 13. Kapton tape was used to avoid short circuits between some parts of the wires loops during the size changes. The preamplifiers and the detuning bias cables were then plugged to their respective loops. Finally, the plastic tubbing is connected to all the bellows and the array is placed in the housing. Only one tube leaves the box to be connected to the vacuum pump, the check valve, and the air switch, as shown in Figure 4.16.

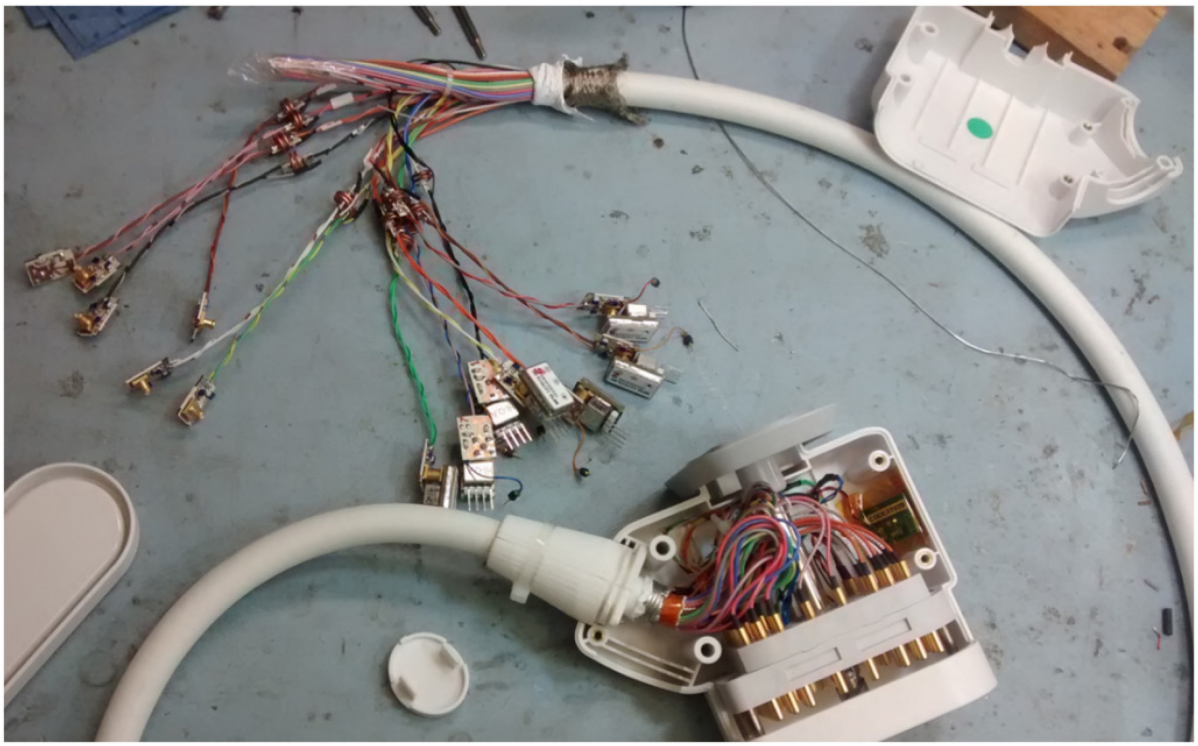

Figure 4.24 Coil cable with all cable traps and output boards connected. Some preamplifiers are plugged to the output boards. The P connector is open showing the coil ID card.

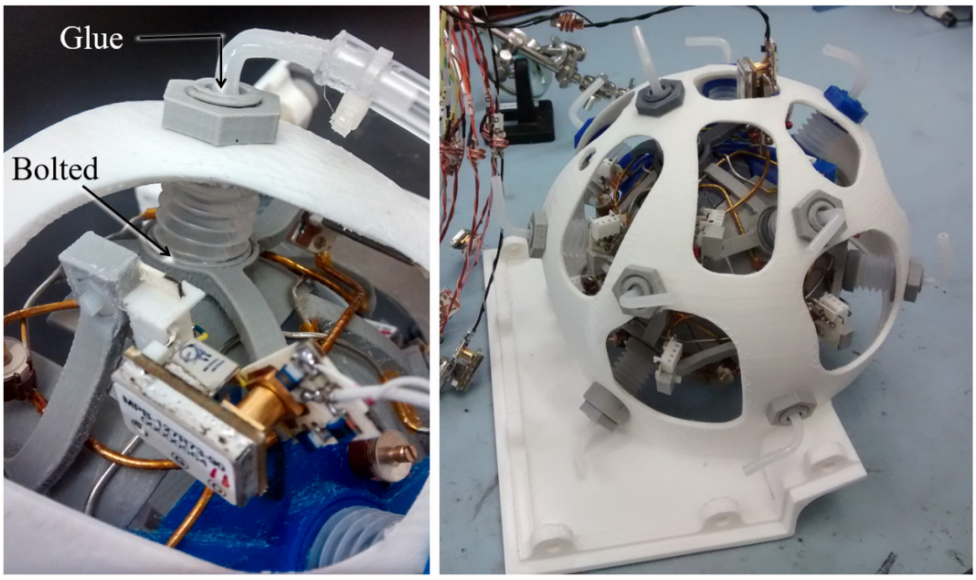

Figure 4.25 Assembly of the coil elements in the spherical frame. The preamplifier of the element 1 is connected on the right picture. The input tubes of the bellows were bent to use the space more efficiently.

4.4 Workbench tests

4.4.1 Accessories

Several accessories are required to perform an adequate coil evaluation in the RF laboratory. A very important device to mimic the receivers of the scanner and the active detuning control signals during the bench tests is the test box, also called test rig. Its purpose is to provide the coil with the DC voltage needed to feed the preamplifiers and a manually switched voltage to control the PIN diodes of the detuning circuits. It is used to selectively detune non-used loops in the array when some adjustment and tests are performed. A 32-channel test box was designed and constructed for this project, which allows to test other coils. It has the same female output connector that will be used in the scanner to connect the coil. Output BNC connectors are also provided to allow the measurement of the output signals of the preamplifiers.

The constructed test box was designed to be fed with three laboratory power supplies, +10V for the preamps, +8V to bias the PIN diodes for detuning the loops and -13V to strongly switch them off. The power supplies can be included in the design if an autonomous test box is needed. Parts of the electrical schematic and the PCB are shown in Figure 4.26 as all 32 channels have the same

circuit. The +10V are directly sent to the P connector while the voltages for the PIN diode are routed through the PCB where they are switched and decoupled from the RF signal. The switches are set to position 3 to send 100 mA to the PIN diodes to detune the loops. In the GE systems, the detuning bias pulses are sent to the coil elements through the inner conductor of the coaxial cables used to receive the RF signals from the preamplifiers. Each coaxial cable is connected to one receiver port in the coil connector, called P connector by GE. A picture of the test box is shown also in Figure 4.26.

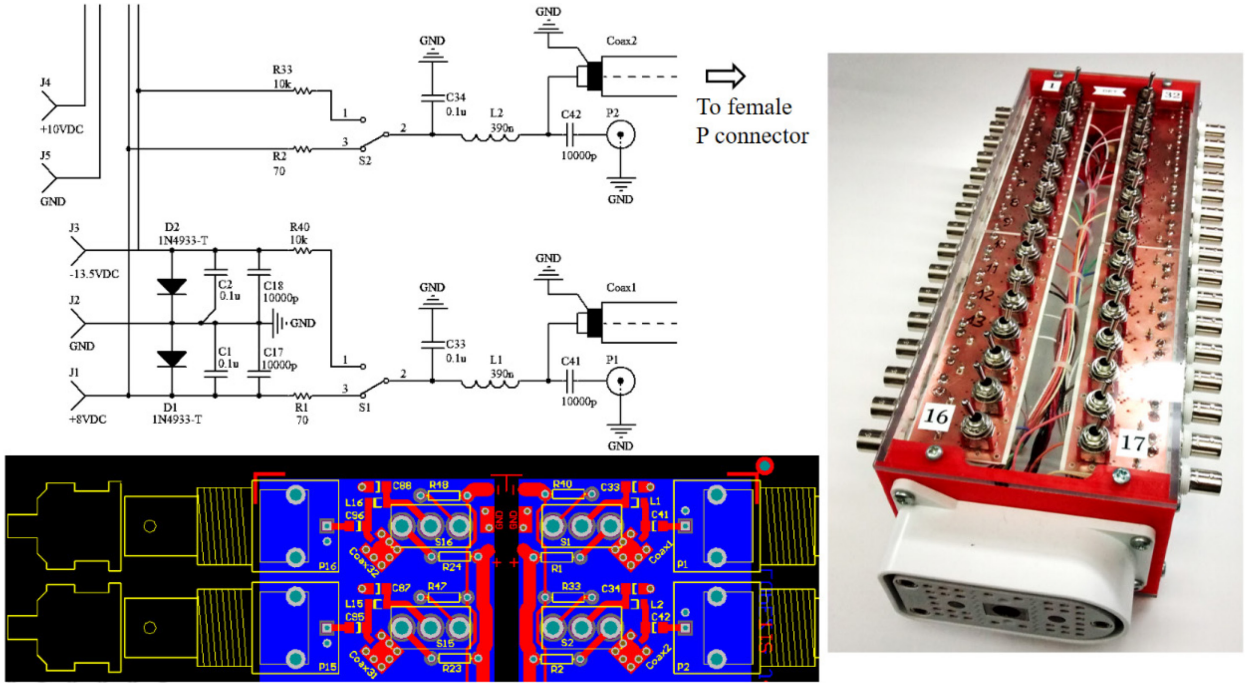

Figure 4.26 Constructed test box. The schematic of channels 1 and 2 with the DC voltage connectors and the PCB of channels 1,2, 31 and 32 are shown. A picture is shown on the right where the P connector is seen at the bottom.

Other important accessories are the probes [67]. Two decoupled double probes, a parallel double probe and a very small sniffing, or pick-up probe were constructed to perform different test that will be described in subsequent sections. They are shown in Figure 4.27.

Finally, some useful devices were built such as a calibration kit to improve the accuracy of the impedance measurement performed on some loops and other parts, a dummy adjustable preamplifier having only the input circuit to evaluate the effect of the preamplifier decoupling on

the loops in a simplified way and some adjustable impedance transformers to adapt the loops to the 50 Ohm of the network analyzer during S_{21} measurements. These devices are shown in Figure 4.28

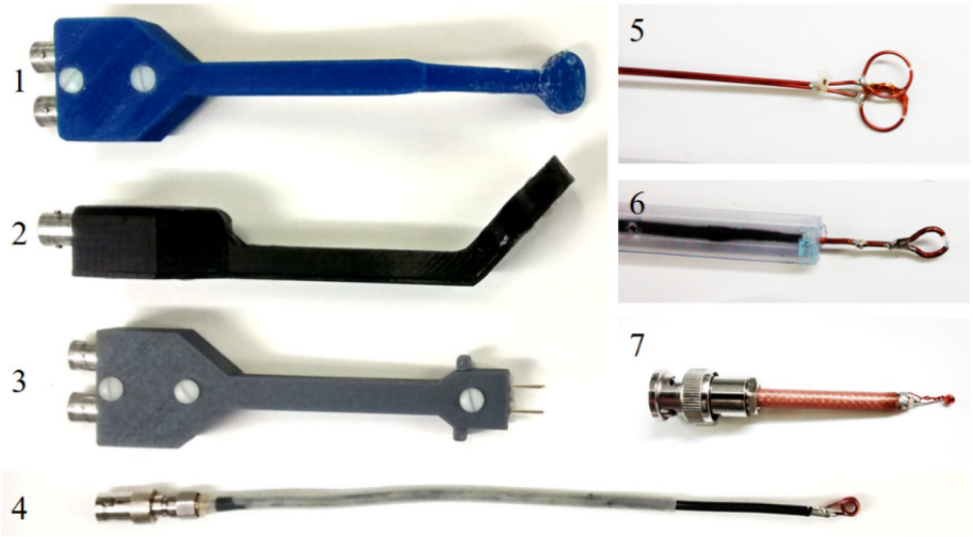

Figure 4.27 Constructed test probes. 1, 2 and 5 are decoupled double probes made of critically overlapped single magnetic field probes, like 6. 1 and 2 have the same structure but the size of the part that contains the loops is different. 3 is a parallel double probe. 4 and 7 are solenoidal probes also called sniffing probes.

.

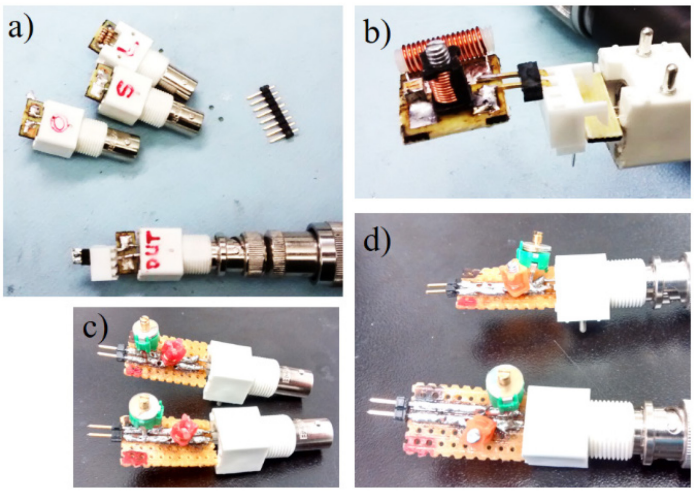

Figure 4.28 Calibration and test devices. a) Calibration kit for improving impedance measurements. b) Dummy preamplifier. c) and d) Impedance L-type transformer networks made with variable components.

4.4.2 Initial studies

4.4.2.1 Small 4-channel array

A 4-channel array was designed, constructed and tested to evaluate the behavior of small elements matched to impedances higher than 50 Ohm and the reachable levels of preamplifier decoupling. The selected preamplifier was the MPB-123R20-0 (Hi-Q.A. Inc., Carleton Place, ON, Canada) which is made for the Siemens 3T Larmor frequency but it was already available and all conditions to test it were created. The package is the same as in Figure 4.4 and the topology of the circuit was as in Figure 4.3 although adapted to the Siemens specifications, in which the detuning signal is provided in a different way. The characteristics of the preamplifier and the electrical schematic used in all channels is shown in Figure 4.29.

	Siemens 3T	Unit
Center Frequency	123.2	MHz
3dB Bandwidth	31±2	MHz
Phase Throughput	93±6	Degrees
Adjustable gain range (S21)	25 (min) to 32 (max)	dB
Input Z - Real (S11)	1.4 (typ) 1.6 (max)	Ohm
Input Z - Reactive Range (S11)	+j3 to +j32	Inductive Z
Output Return Loss (S22)	<-15	dB
Reverse Isolation (S12)	<-70	dB
Noise Figure	0.5 (typ) 0.55(max)	dB
O/P 1dB Compression Point	>+1	dBm
O/P 3rd Order Intercept Point*	>+13	dBm
Current Consumption	<8	mA
Supply Voltage	10 ± 1	VDC
Maximum RF Input Power **	+30	dBm

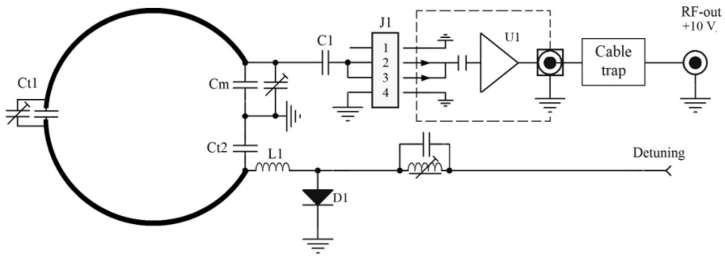

Figure 4.29 Preamplifier specifications and electric design of 4-channel array.

The loops have a diameter of 40 mm and were made of a 16 AWG wire, which resulted in an inductance of 88 nH measured with the network analyzer at the Larmor frequency. In an initial test, the loops were matched to 310 Ohm with calculated capacitances for tuning and matching of 30 pF and 49 pF respectively. Images were acquired with acceptable results even though the noise match was outside the recommended range for the preamplifier.

The noise match was then redefined to 50 Ohm to reevaluate the preamplifier decoupling. The capacitors were recalculated, being the tuning capacitance 21.4 pF (Ct1 = 3-33 pF, Ct2 = 139 pF) and the matching capacitance (Cm) 139 pF. A capacitance in series with the preamplifier input was needed (C1 = 55 pF) to enable the preamplifier decoupling adjustment by means of the control range of the input reactance of the preamplifier. The average Q_U/Q_L ratio of the loops in the array was 239 / 53 = 4.5, which is high enough to obtain sample noise dominance in the images. The load was a 0.5-liter bottle containing a solution of tap water and 2.5 g of salt. This array was adjusted for geometrical decoupling obtaining values between -20.9 dB and -28.8 dB, which

completed an excellent decoupling in the array. The preamplifier decoupling was measured in all channels with the non-tested ones detuned using a typical method described below. The array was mounted in a simple semi-cylindrical structure and wired to an 8-channel Siemens coil connector. The final construction loaded with a phantom is shown in Figure 4.30.

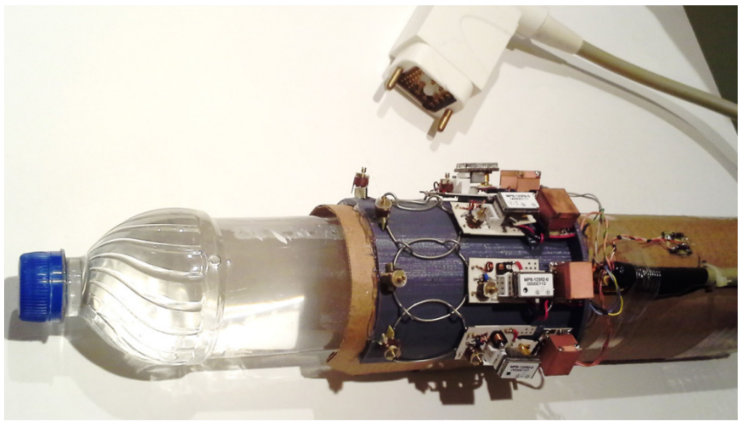

Figure 4.30 Picture of the 4-channel array.

Tests in a scanner were afterward performed. The noise correlation matrix was generated to verify the decoupling in the array and images reconstructed by the Sum-of-squares method (SoS) were acquired with the phantom to compute the SNR map. A non-homogeneous sample was also scanned, in this case a small orange, to evaluate the capacity of detecting fine structures. In addition, a parallel imaging technique was used (MPRAGE) with an acceleration of 3x.

4.4.2.2 150-Ohm WanTcom

The main goal of this test was to study the efficiency of the preamplifier decoupling as a decoupling method when the distance between coil elements changes. A WMM series miniature 6-pin preamplifier (WanTcom Inc., Chanhassen, MN, USA) was selected due to its small footprint and its relatively high impedance noise match (150 Ohm). These features could be exploited to build an array with small dimensions and good decoupling. On the other hand, it is designed for the GE Larmor frequency at 3 T, which makes it a good candidate for the proposed array. To start, the parameters of the preamplifier were measured at 127.73 MHz. It has a low input impedance with an adjustable reactive part that can be used to fine-tune the preamplifier decoupling. A picture of the preamplifier and the PCB used to measure its parameters are shown in Figure 4.31 along with the obtained data.

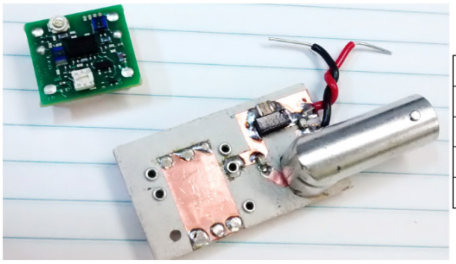

IDC	15	mA
Gain	32.4	dB
Zin (factory setup)	2.15 – j 0.83	Ohm
Zin (max)	2.7 + j 5.84	Ohm
Zin (min)	0.6 – j 18.81	Ohm

Figure 4.31 WMM miniature 6-pin preamplifier and measured parameters.

A small loop with a diameter of 3.7 cm was selected, since a high parallelization was initially intended and the targeted samples are small. Its impedance, measured with the network analyzer, was 0.695 + j65.7 which represents an inductance L = 81.8 nH. The loop was matched to 150 Ohm since that is the noise match specified for the preamplifier. The required tuning capacitance was 22.44 pF and the matching capacitance was 122 pF. A simple architecture was selected as presented in Figure 4.32. In this circuit, the reactance of Cm and Lm must be equal if the preamplifier decoupling is going to be implemented with the factory impedance setup of the preamplifier (0 reactive part). However, it is advantageous to use the capacitor provided in the preamplifier to adjust the preamplifier decoupling as was done before. By combining simple calculations with simulation tools, the values of Ct1 = 27.57 pF, Ct2 = Cm = 122 pF and Lm = 12.73 nH, which satisfy the conditions of providing 150 Ohm and enabling preamplifier decoupling were found. Lm was replaced by a standard value (27 nH, Coilcraft) which in this case requires an adjustment of the reactance of the input circuit of the preamplifier to -j11.45 Ohm to achieve the preamplifier decoupling. Notice that after connecting Lm the impedance at the Larmor frequency, that was adjusted to 150 Ohm, will slightly move to the inductive part of the Smith chart, which is corrected with a very small adjustment of Ct1. The resulting impedance change is only 1.4 Ohm.

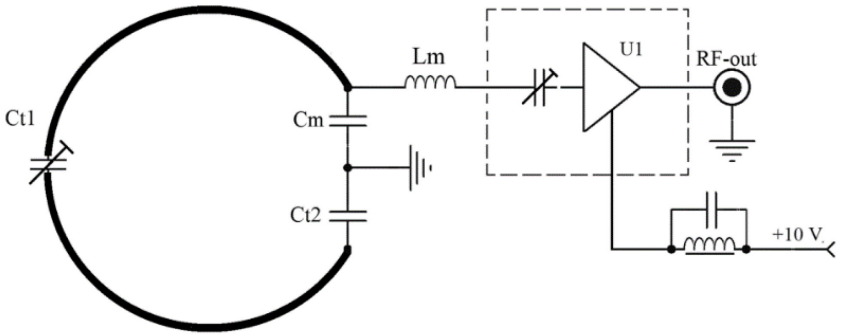

Figure 4.32 Coil element architecture used for 150-Ohm preamplifier.

To study the influence of the preamplifier decoupling in the decoupling, another loop (B) with the same dimensions was built. This loop is not connected to a preamplifier. The setup is represented in Figure 4.33. Initially, the loop B is placed in a fixed position and then tuned and matched to 150 Ohm by means of the components show before. A transformer was afterward connected to adapt its impedance to the 50 Ohm of the network analyzer. The loop with the preamplifier (A) is placed at the desired distance from B. A small magnetic field probe is fixed in a position where it is coupled to loop A. Then, the loop A is removed and S_{21} is taken. Afterward, the loop A is placed in the previously selected position, without moving the probe, and S_{21} is taken again. The difference between both S_{21} values indicates how much field is captured by loop A. The influence of the preamplifier decoupling can also be evaluated by testing the loop A with and without the preamplifier. The distance of the loop A (and the probe) to the loop B is then changed and the process is repeated.

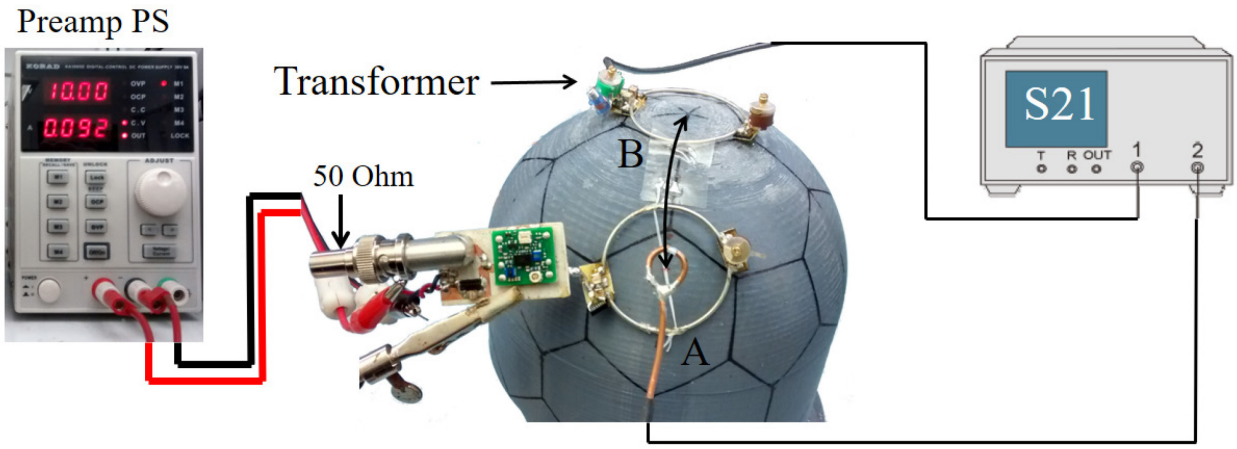

Figure 4.33 Setup to evaluate preamplifier decoupling effect according to distance between loops.

Another test to evaluate the effect of the preamplifier decoupling was performed with the same preamplifier. For this test, two different loops with dimensions closer to the final design were constructed (6.2 cm and 5.2 cm). The loops were again matched to 150 Ohm and all the previous procedures were followed to test the elements. A PCB was designed and built to include the preamplifier and the associated circuits. In this case two complete elements were built. The schematic of Figure 4.3 was used, but C1 was replaced by Lm as in Figure 4.32. The loops were soldered to the multiway cable coil as the connection to the test box was required for the measurements. The values of the used parts are presented in Table 4.1, and a picture of both sides

of the PCB is shown in Figure 4.34. The preamplifier decoupling level reached with this configuration was again around -30 dB with both channels.

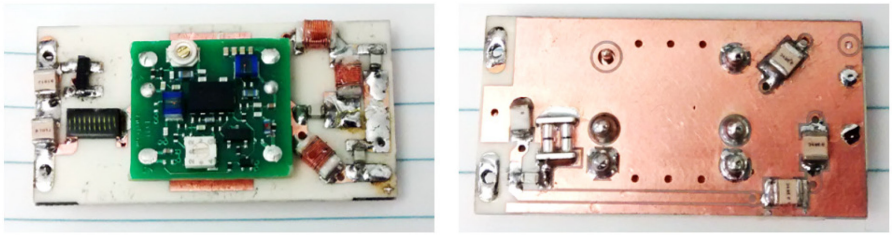

Figure 4.34 PCB for 6-pin miniature preamplifier.

Table 4.1 Part values used to tune and match the loops to 150 Ohm.

	Loop A	**Loop B**	**Units**
Diameter	6.2	5.2	cm
Ct2 = Cm	100	124	pF
Ct1	3-33	3-33	pF
Lm	27	27	nH
L1 (adjustable)	15.5	12.5	nH

The setup for this test is presented in Figure 4.35. Both preamplifiers were fed and the loops were not detuned. The loop B was placed in a fixed position and the loop A was discretely moved with respect to B. An S_{21} measurement in the complete receiver channel B, to read its frequency response, was taken at each position. The trajectory of the movement is represented with the black arrows in Figure 4.35. A small change around the Larmor frequency might be expected if the preamplifier decoupling reaches a high level, which could be useful to build an adjustable array. The output of channel A was loaded with 50 Ohm in the test box.

This test was repeated with the preamplifier shown in Figure 4.4 with very similar results. This was a strong reason to decide that the MPB-127R73-90 preamplifier from Hi-Q.A. Inc. would be used to build the adaptable array. Other aspects were considered in this decision, namely: the possibility to build a complete channel with smaller dimensions and mechanical flexibility, the ease to plug and unplug it (which is important during the development and coil set-up) and the availability.

These tests helped to decide important parameters that could define the performance of the resulting coil. The next step was to design and build the array as explained in previous sections. Once all parts were fabricated the array was tested in the RF laboratory as explained below.

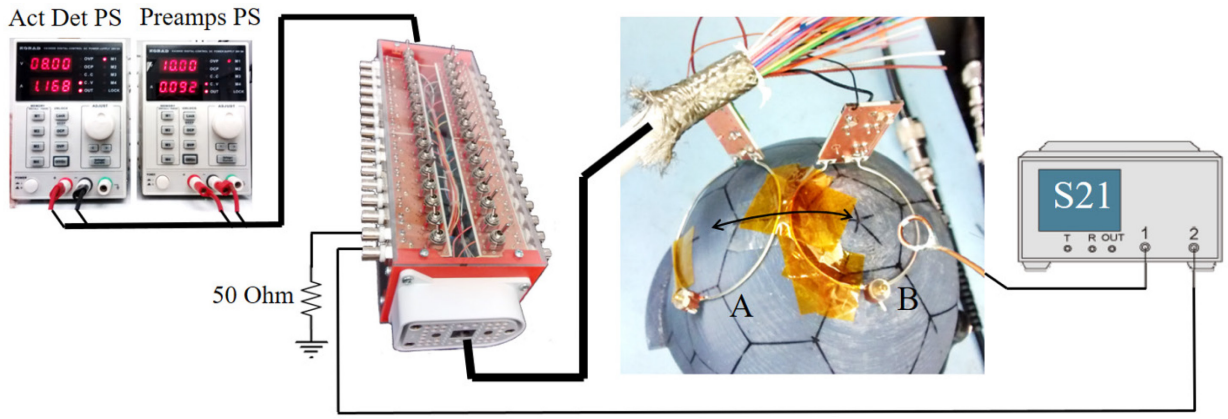

Figure 4.35 Setup to evaluate the effect of the preamplifier decoupling between complete array elements.

4.4.3 Final coil tests

4.4.3.1 Loop impedance

A network analyzer (E5061B, Agilent, Santa Clara, California, US) was used during all the bench tests. The first test was the measurement of the impedance of the wire loops. It is required to find the inductance needed to calculate the tuning and matching capacitors. This test was performed before soldering the tuning and matching capacitors. The loops were mounted in the element support, to keep the same distance from the phantom surface during all measurements, but they were not soldered to the matching/detuning board. Instead, they were soldered to the connector labeled DUT of the kit shown in Figure 4.28a, which was also used to calibrate the analyzer. They were fixed directly on the surface of the M phantom, using Kapton tape, at approximately the position where they will be during the scanner tests. Only one loop from each shape was tested (1, 2 and 11). The used setup, one loop and its impedance curve are shown in Figure 4.36.

4.4.3.2 Tuning and matching

With the obtained loop impedances, the tuning and matching capacitors were calculated. The loops were afterward soldered to the matching/detuning boards and the tuning and matching capacitors were mounted. Notice that for simplicity only three capacitor values were used for the three basic loop shapes. As before, the assembled loops were placed on the M phantom (see Figure 4.23). All

the loops were individually matched to approximately 175 Ohm and tuned to f_0 = 127.73 MHz (GE Larmor frequency for 3T). The analyzer was used in S_{11} mode, as in the previous test, but the calibration was performed after the 2-way connector attached at the end of the test cable, as illustrated in Figure 4.37.

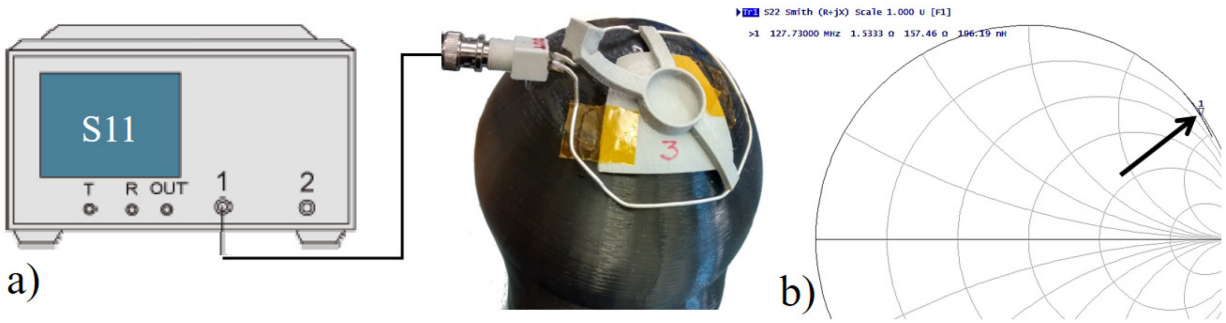

Figure 4.36 Impedance measurement setup to find the loop inductance (a) and one result (b).

The loaded quality factor (Q_L) was also measured in this position and finally Q_U after removing the loops from the phantom. A decoupled double probe (2 in Figure 4.27) was used in this case to perform the S_{21} measurements. The probe was provided with a spacer that facilitated its placement at a constant distance from the tested loops. Q_L and the impedances were also measured for the S and L phantoms. The setup is shown in Figure 4.38 as well as a typical Q measurement result.

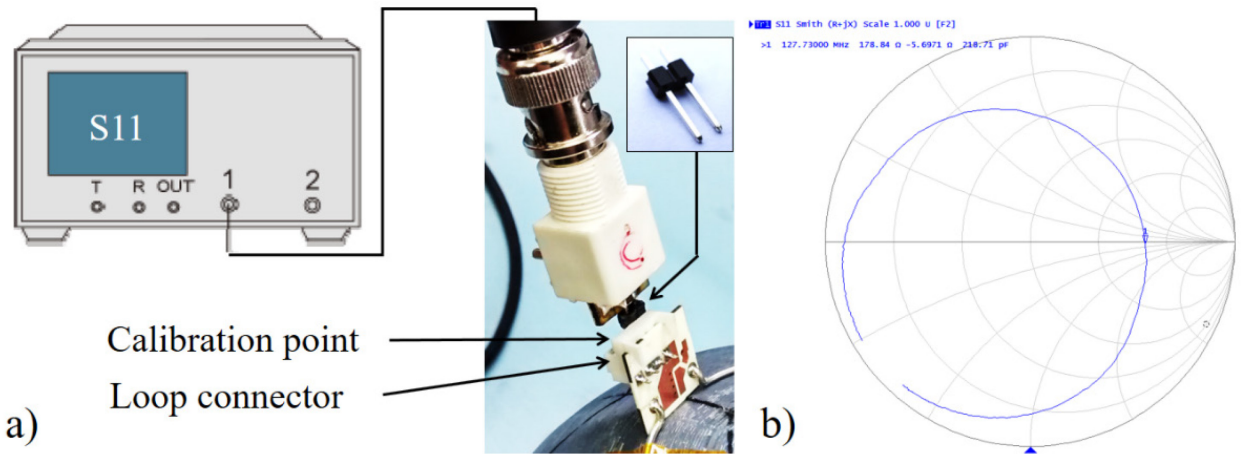

Figure 4.37 Loop output impedance measurement setup (a) and one result after the adjustment(b).

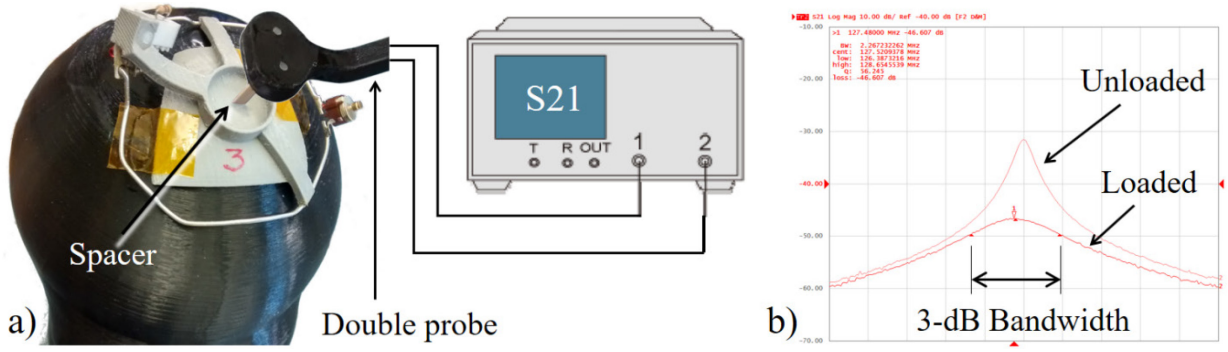

Figure 4.38 Setup used to perform decoupling tests (a) and a typical Q measurement results (b).

4.4.3.3 Active detuning

The active detuning inductor (L1) was a handmade solenoid of a 24 AWG enameled copper wire having three turns with an inner diameter of 1.6 mm. An initial adjustment of the parallel resonant circuit formed by L1 and Ct2 was performed by using a sniffing probe (see 4 in Figure 4.27) slightly coupled to L1 to detect the resonant peak. With this purpose, the loop was open by removing Ct1. The distance between turns was manually adjusted to move the resonant peak to the Larmor frequency.

After re-soldering Ct1 to the loop, the measuring setup shown in Figure 4.38 was used. A resonance peak was taken as a reference without feeding the PIN diode. Then, the PIN diode was fed with 100 mA directly provided by a laboratory power supply. The valley between the two split peaks was tuned to the Larmor frequency by readjusting L1. As an example, the result of one test is shown in Figure 4.39.

4.4.3.4 Preamplifier decoupling

All the elements were completely assembled before this test since the preamplifier must be operating for a proper adjustment of the preamplifier decoupling. The coil cable must be connected to the test box (see Figure 4.26). The preamplifier decoupling was adjusted by using the decoupled double probe [132] and the setup shown in Figure 4.38. The M phantom was used again. It is important to reduce the power output from the network analyzer to less than -30 dBm to protect the preamplifier.

The range of the variable reactance at the input of the preamplifier was not enough to tune the preamplifier decoupling and consequently a series capacitor (C1 = 100 p) was added. This capacitor

mainly was used to cancel the inductance added by the 4-way connector and the rest of the PCB traces which resulted in nearly 16 nH. The change introduced by this capacitor in the loop impedance is negligible (about 0 - j12 Ohm) and it can be compensated by a very small adjustment of Ct1.

To evaluate the level of preamplifier decoupling the first step was to take a reference measurement with a 175 Ohm resistor replacing the preamplifier in the 4-way connector (J1). This resistance is equal to the output impedance of the loop. Then, the resistor was removed, and the preamplifier was plugged and fed. The expected response must have the known M-shape, as can be seen in the example presented in Figure 4.39. The difference between the peak of the reference and the valley of the M-shaped curve is an indication of how good is the preamplifier decoupling.

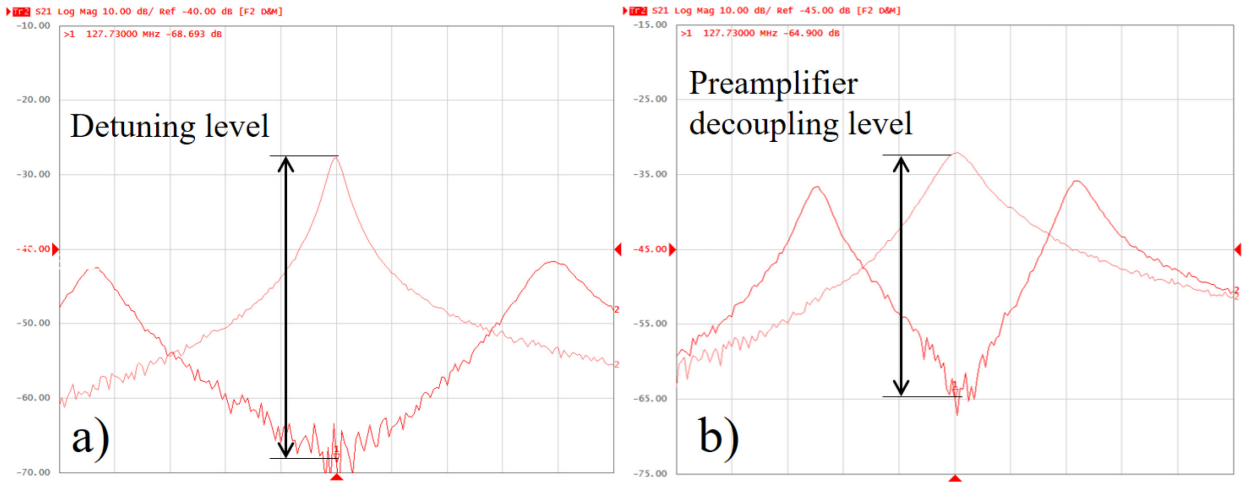

Figure 4.39 Typical results of the active detuning (a) and preamplifier decoupling (b).

4.4.3.5 Array tuning

The loop array was completely assembled, as described before. It was expected that the overall tuning/matching condition would change, since each loop is surrounded by the other loops and metallic parts that introduce additional parasitic capacitances and losses. Consequently, the loops were re-tuned with the M phantom as a load. This was performed on each loop by using the setup of Figure 4.38 and detuning all the other loops from the test box, as typically performed [67]. The preamplifier of the tested loop was unplugged and the corresponding variable tuning capacitor (Ct1) was adjusted. The non-tested preamplifiers were also turned on to increase the decoupling level.

4.4.3.6 Impedance and Q_L in the array

The impedance of each loop was measured immediately after re-tuning to take advantage of the coil setup. This test is useful to evaluate the possible impact of the impedance change on the noise match and the preamplifier decoupling, which could result in the recalculation and change of the matching capacitor. The Q_L was measured again to assess the contribution of the environment to the losses.

Afterward, the detuning current was disabled and a new impedance measurement was performed. In this condition, the decoupling of the tested loop from the others is worse as it relies only on the array geometry and the preamplifier decoupling, which was previously verified. Therefore, the resulting value is the source impedance connected to the preamplifier during normal scans, which is the reason for this test. Since this impedance has an important contribution to the noise performance of the selected preamplifier, it should be kept in the recommended range (50 to 200 Ohm) for all possible array configurations.

The change in tuning frequency and impedance, with respect to the previous test (where all non-tested loops were detuned) were used to assess the effectivity of the preamplifier decoupling, which has a major importance in this array, as explained above. It is expected that a good preamplifier decoupling results in small tuning frequency shift and impedance change.

The impedance and the Q_L were initially measured with the M phantom, as explained, and repeated later for the S and L phantoms without any additional adjustment. The measuring setups were the same described for the independent elements.

4.4.3.7 Array coupling

In array coils with geometrical decoupling, a required test is the measurement of the coupling (S_{21}) between adjacent elements as a part of the adjustment of the critical overlapping. For those arrays, it is recommended to have -15 dB of geometrical decoupling plus -15 dB provided by the preamplifier decoupling [67]. In this project, the geometrical decoupling adjustment is not performed. However, the S_{21} between some pairs of loops was measured to obtain a more complete idea about the total decoupling in the coil.

To measure the S_{21} interaction between pairs of coils, they were connected to the network analyzer by means of LC transformers as those shown in Figure 4.28c, d. The preamplifiers of the tested

elements were unplugged, while the others were used as a part of the detuning current path. The transformers are plugged into the 4-way connectors (J1). The coil was connected to the test box and all the non-tested loops were detuned by means of their corresponding switches. This is a time-consuming test as the transformers must be adjusted to convert the impedance of the loops to the 50 Ohm of the network analyzer while the S_{21} parameter is minimized. Some iterations were normally needed, and different transformers were used for different pairs of loops. The setup is shown in Figure 4.40a along with a typical measurement (b), performed on well-matched elements which are weakly coupled.

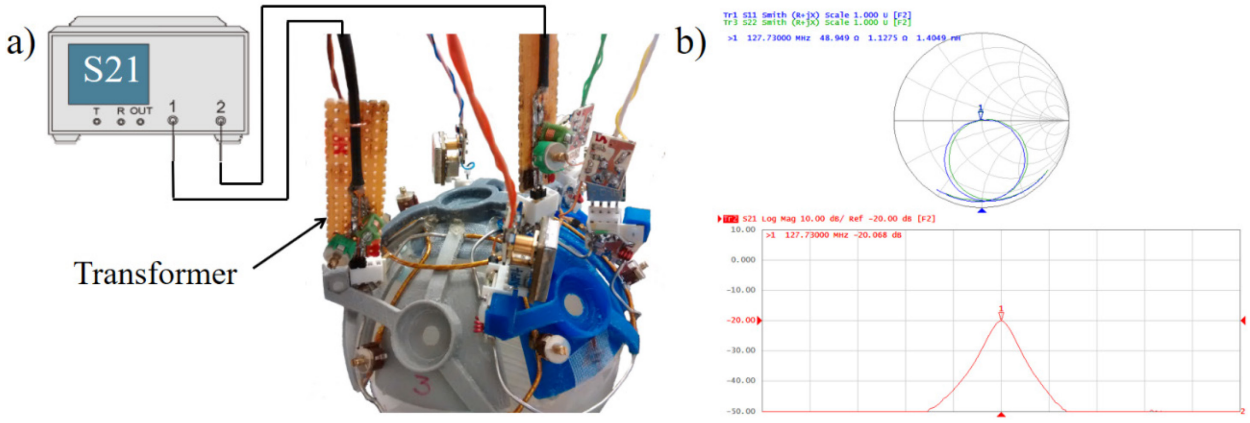

Figure 4.40 Setup used to measure the interaction (S_{21}) between loops (a) and a typical result (b) showing very good matching of both elements (top) and a good decoupling (bottom). The span was 40 MHz.

4.4.3.8 Loop sensitivity profile

The sensitivity profile, or frequency response, of each channel was observed for the three phantoms by an S_{21} measurement. It was expected to obtain the typical "dog-ear" shape in the network analyzer [69]. A magnetic field probe (1 in Figure 4.27), connected only to Port 1 of the network analyzer, was used to transmit a very low RF magnetic field to the loop under test. It was placed behind the loops, as centered as possible and at a constant distance guaranteed by a spacer attached to the probe. The output of the tested channel was connected to Port 2 and all other channels were loaded with 50 Ohm through the test box. The power of the network analyzer was reduced to less than -30 dBm. The used setup and one measurement performed on an isolated channel are presented in Figure 4.41.

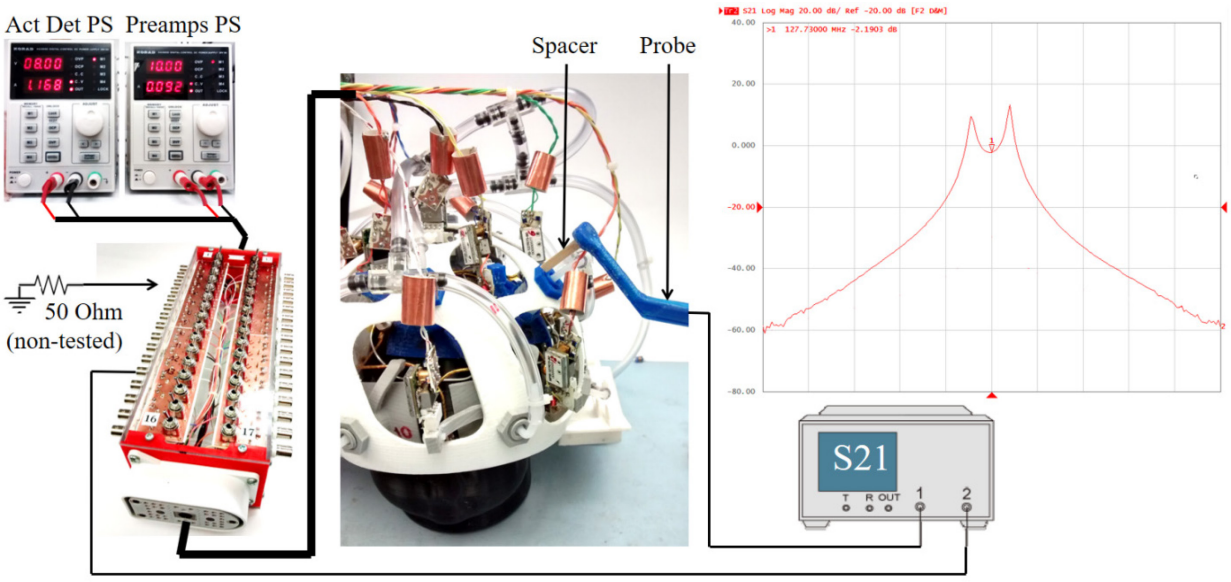

Figure 4.41 Setup used to measure the frequency response of the array elements (a) and typical dog-ear shape obtained from an isolated channel.

The stability was also evaluated with this setup by replacing the field probe with a 50 Ohm load directly plugged in Port 1. The coil dimensions were continuously varied through the whole range for this test by means of the vacuum pump.

4.4.4 Scanner tests

The final validation of the coil was performed on a Signa MR750 3T MRI scanner (GE Healthcare, Chicago, IL, US). A 32-channel commercial head coil made for adults was used as reference for comparisons. This coil is frequently used to scan neonates. The three constructed phantoms were scanned with the proposed coil and with the commercial coil. They were placed at the geometrical center of the coils, which coincided with the magnet isocenter.

Axial and sagittal Spoiled Gradient Recalled (SPGR) pulse sequences were used to acquire the phantom images. The parameters of the sequences were: TE = 5.5, TR = 500, Flip angle = 10º, Slice Thickness = 5 mm, Matrix = 256 x 256 and FOV = 150 mm.

4.4.4.1 Noise correlation matrix

The noise correlation matrices provide a good measure of the quality of the coil in terms of general decoupling and is useful to perform other calculations. For this reason, all the phantom acquisitions

were immediately repeated with the RF excitation power set to zero and the obtained noise images were used to compute the noise correlation matrices in all selected conditions. For this purpose, a simple MatLAB function was used to read the image files and calculate the noise covariance matrix by using [20], [68]:

$$\boldsymbol{\Psi}_{i,j} = \langle n_i n_j^* \rangle \tag{4.8}$$

where n_i and n_j are the complex noise variances of the i^{th} and j^{th} coil elements. Afterward, the noise correlation matrix, which is basically a normalization of the noise covariance matrix, was calculated by:

$$\boldsymbol{\Psi}_{i,j}{}^{corr} = \frac{\boldsymbol{\Psi}_{i,j}}{\sqrt{\left(\boldsymbol{\Psi}_{ii}\boldsymbol{\Psi}_{jj}\right)}} \tag{4.9}$$

where $\boldsymbol{\Psi}_{ii}$ and $\boldsymbol{\Psi}_{jj}$ are the noise autocovariances of the i^{th} and j^{th} coil elements.

4.4.4.2 SNR maps

The SNR maps were calculated with the method usually recommended for array coils [133]. It involves the acquisition of noise reference by recording complex-valued data during the zero-transmit-power acquisition. The noise covariance matrix is then calculated with this data. With the complex data acquired with each channel, with the loaded coil, and the calculated noise covariance matrix, the SNR map is computed by using the root-sum-of-squares (rSoS) reconstruction [8]. If the rSoS reconstruction is performed with the magnitude image of each individual channel, a correction on a pixel-by-pixel basis for the SNR bias introduced by the magnitude detection, must be performed [133].

CHAPTER 5 RESULTS

5.1 Simulations

5.1.1 Loop impedance

The impedance of the wire loops alone (no tuning and matching capacitors present), with the M size sphere as a load, are shown in Table 5.1, second column. Therefore, the resistive part includes the coil resistance and the sample resistance. The capacitance values required to tune and match the loops to 175 Ohm are shown in the third column. These are the values found by means of a Smith chart tool after the verification of the calculated values. Finally, the capacitors used for the simulations, after being readjusted in FEKO, are shown in the last column. The tuning curves of the three groups of loops, detected with the decoupled probes, can be seen in Figure 4.41. Here the tuning capacitance was divided in two capacitors (Ct1 and Ct2).

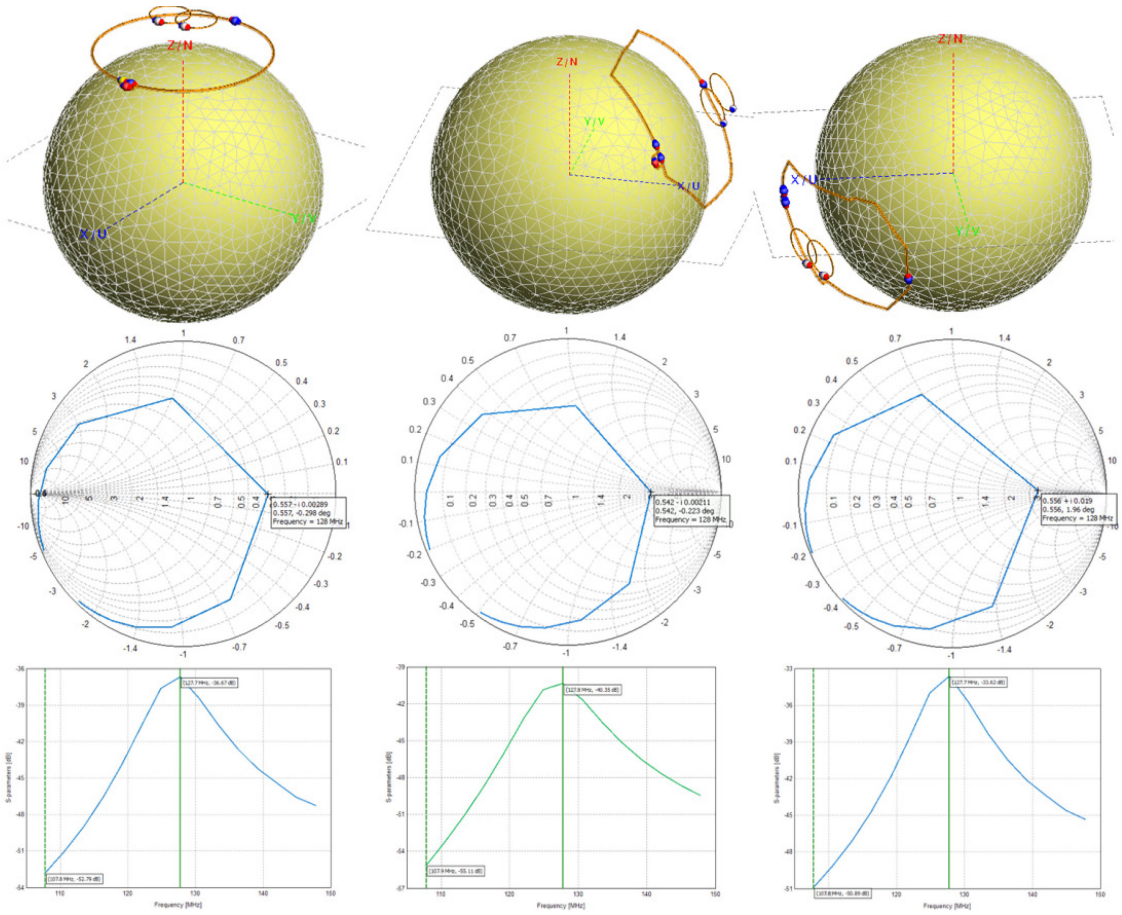

Figure 5.1 Impedance and tuning curves of the three types of loops.

Table 5.1 Loop impedance and tuning/matching capacitors.

Loops	**Z loop measured** (FEKO)	**Caps Tune/Match** (Smith chart)	**Caps Tune/Match** (FEKO)
1	2.24 + j141 (L = 176 nH)	10.27 p / 62.7 p	10.73 (13.11-59) p / 59 p
2-7	2.9 + j140 (L = 174 nH)	10.59 p / 55 p	10.94 (13.72-54) p / 54 p
8-13	1.7 + j137 (L = 171 nH)	10.78 p / 75 p	10.91 (13.11-65) p / 65 p

In table Table 5.2 the impedances measured in FEKO at the loops outputs are presented. Notice that they were adjusted to nearly 175 Ohm for the M size load (10.25 cm) and were preserved for the other sample dimensions. The resulting values decrease while the sample size is larger. Also, the impedances for the S load are outside the recommended range but some reduction is expected due to the addition of the other components of the coil. The shapes of all the curves obtained from the simulations were very similar to the samples shown in Figure 5.1.

Table 5.2 Impedance of the tuned/matched loops for all sample dimensions.

Loops	**8 cm (S)**	**9.1 cm**	**10.25 cm (M)**	**11.4 cm**	**12.5 cm (L)**
1	237.7+j47.5	216.6+j12.7	175.7-j1.5	147.3-j6.8	126.6-j8.4
2-7	261.7+j54.9	201.6+j17.1	168.3-j1.0	141.5-j7.6	123.3-j5.7
8-13	266.1+j49.9	215.5+j15.5	176.8+j0.0	150.1-j6.2	130.8-j8.8

5.1.2 Active detuning

Figure 5.2 shows the S_{21} curve measured on a detuned loop (1) with the double probe. Similar curves were obtained from the other loops. A decoupling level of around -37 dB allowed to effectively detune selected loops when desired.

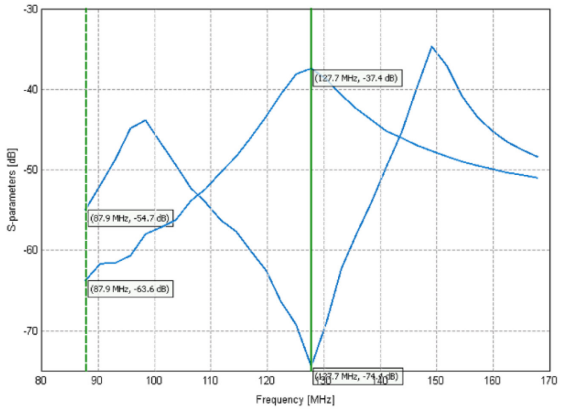

Figure 5.2 Simulated active detuning.

5.1.3 Critical overlapping

The overlapping between pairs of loops was adjusted with the goal of reaching decoupling levels below -15 dB. However, when three loops were adjusted together that goal could not be achieved and the values among them ranged from -13.4 to -15.9 dB. Good matching levels were always achieved as can be seen in Figure 5.3.

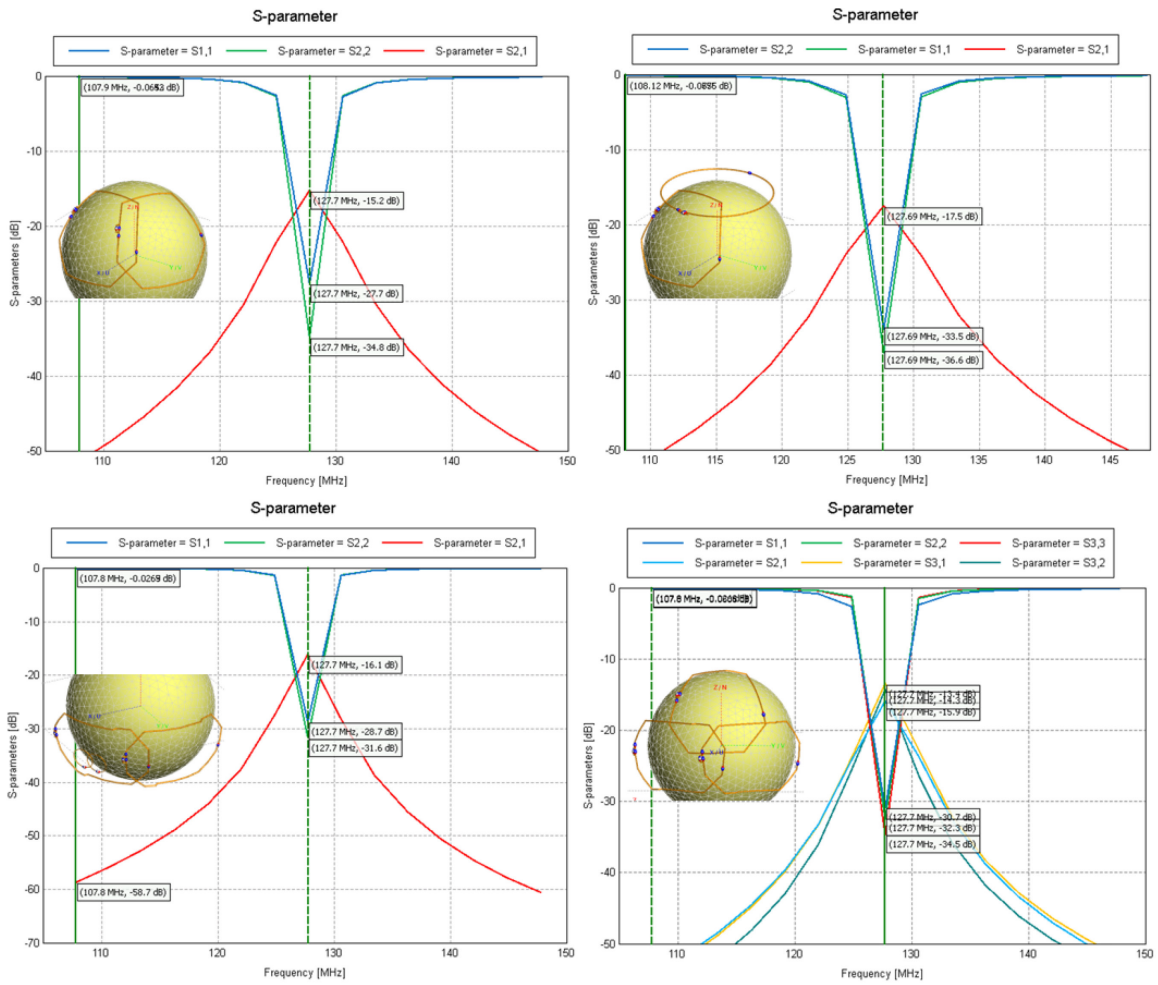

Figure 5.3 S_{21} achieved between loops by geometrical decoupling. The adjusted loops are shown in each graph along with the S_{11} curve for each loop.

5.1.4 S-parameters matrix (tuned/matched array)

After a complete model of the coil was created, with all the previous geometry changes included, the tuning and matching capacitors were readjusted to the values shown in Table 5.3 to match the loops to 175 Ohm again. The S-parameters matrix computed afterward, with the M size load,

resulted in an S_{21} average of -14.58 dB with a maximum value of -14.32 dB and a minimum of -21.56 dB. The matrix is shown in Figure 5.4.

Table 5.3 Tuning and matching capacitances for geometrical decoupling.

Loops	Caps Tune/Match
1	8.6 (19.96-40) p / 40 p
2-7	10.7 (13.41-53) p / 53 p
8-13	10.48 (12.42-67) p / 67 p

The S-parameters matrix was calculated for the other selected sample sizes. They are presented also in Figure 5.4 with the corresponding mean values of all the off-diagonal elements, the maximum and the minimum S_{21} values.

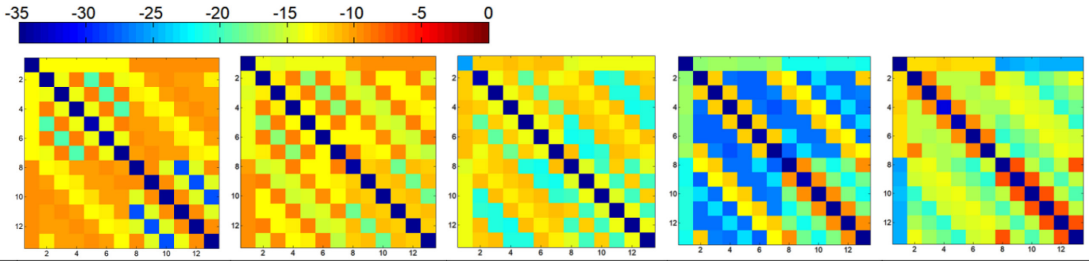

S21	8 cm (S)	9.1 cm	10.25 cm (M)	11.4 cm	12.5 cm (L)
Mean (off-diag)	-12.28 dB	-12.42 dB	- 14.58 dB	- 19.94 dB	- 15.48 dB
Max	- 9.2 dB	- 9.07 dB	- 14.32 dB	- 9.38 dB	- 7.47 dB
Min	- 28.42 dB	- 18.1 dB	- 21.56 dB	- 28.32 dB	- 25.39 dB

Figure 5.4 S-parameters matrices of the simulated geometrically decoupled array.

Since the mechanical design was not possible with the geometrically decoupled configuration and the structure of the array had to be readjusted, new simulations were performed. The tuning capacitors shown in Table 5.1 were readjusted to compensate the capacitance introduced by the other loops. The new values are shown in Table 5.4. The matching capacitors were not changed. The resultant S-parameters matrices of the final configuration are presented in Figure 5.5.

Table 5.4 Tuning and matching capacitances of the final configuration.

Loops	Caps Tune/Match
1	10.66 (19.96-59) p / 59 p
2-7	10.88 (13.41-54) p / 54 p
8-13	10.85 (12.42-65) p / 65 p

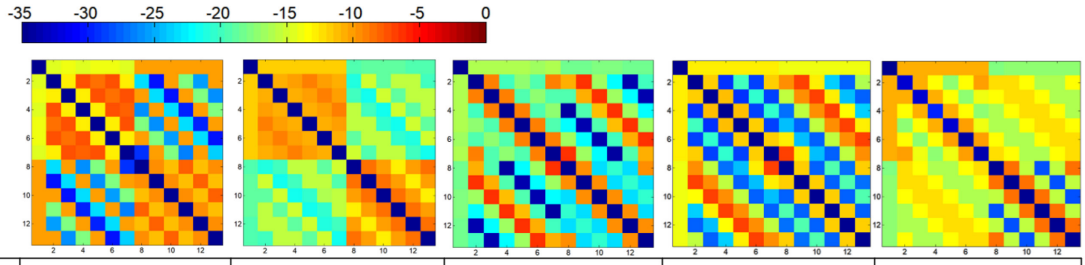

S21	8 cm (S)	9.1 cm	10.25 cm (M)	11.4 cm	12.5 cm (L)
Mean (off-diag)	-14.66 dB	-14.47 dB	-17.25 dB	-17.18 dB	-14.07 dB
Max	-7.45 dB	-8.46 dB	-6.47 dB	-6.84 dB	-8.47 dB
Min	-30.53 dB	-21.61 dB	-34.2 dB	-29.32 dB	-28.29 dB

Figure 5.5 S-parameters matrices of the final simulated array.

5.1.5 Preamplifier decoupling

The preamplifier model resulted in decoupling values of -30.7 dB (loop 1), -31.8 dB (loops 2 to 7) and -34.1 dB (loops 8 to 13), as can be seen from left to right in Figure 5.6. These values were obtained with the loops in isolated conditions. The matching inductors (Lm) were 22.32 nH, 26.5 nH and 21.5 nH respectively.

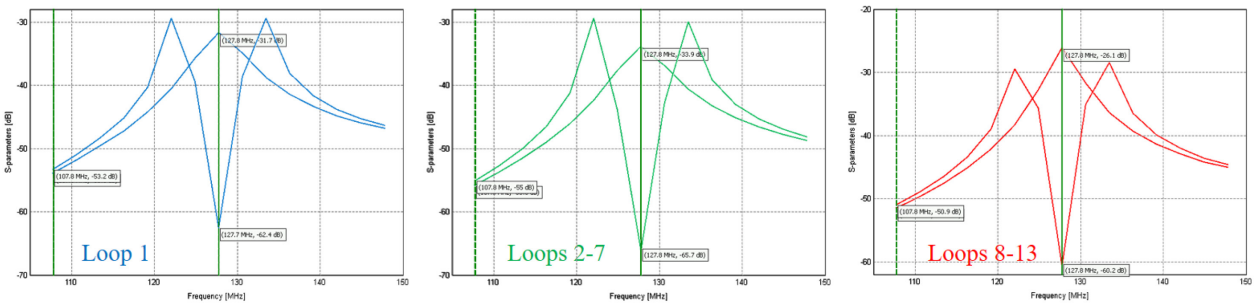

Figure 5.6 Preamplifier decoupling evaluation by simulations.

After the equivalent circuits of the preamplifier were included in the complete array, the isolation matrices were calculated again for the selected load diameters. High average levels of isolation between channels were obtained. The matrices are shown in Figure 5.7, along with the average values of the off-diagonal elements, the minimum and the maximum values. The values of the main diagonal were intentionally converted to zero.

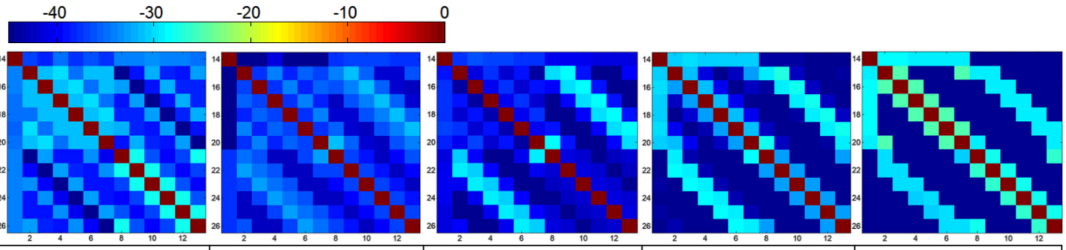

S21	8 cm (S)	9.1 cm	10.25 cm (M)	11.4 cm	12.5 cm (L)
Mean (off-diag)	-36.23 dB	-38.31 dB	-39.63 dB	-39.49 dB	-41.26 dB
Max	-27.84 dB	-31.14 dB	-28.34 dB	-27.4 dB	-24.67 dB
Min	-57.69 dB	-61.82 dB	-45.71 dB	-48.59 dB	-53.89 dB

Figure 5.7 S-parameter matrices after the inclusion of the preamplifiers.

5.1.6 Magnetic field simulations

The initial tests confirmed that the selected preamplifier models could minimize the coupling between array elements. Results obtained with two loops on a rectangular-shaped sample with average brain tissue (ε_r = 63, σ = 0.46 S/m) are shown in Figure 5.8. The S-parameters of the loops in the critical overlapping configuration are shown on top. They demonstrate a good matching (< -20 dB) and the optimized decoupling between loops. The field maps at the bottom show that a magnetic field with very low intensity is induced in the receiver loop in this condition. After the non-fed loop was moved to the strongly-coupled position, a magnetic field was observed in its sensitivity region. When the preamplifier was included in the non-fed loop, the field that was induced due to the coupling with the fed loop was considerably reduced by the preamplifier decoupling effect.

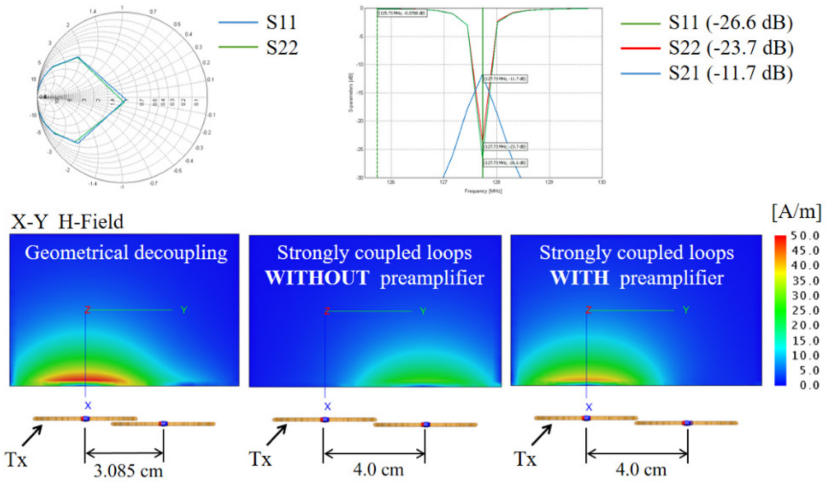

Figure 5.8 Preamplifier decoupling test on two loops.

The test with the complete array resulted in a similar efficacy for the preamplifier decoupling. Examples of the magnetic field maps are presented in Figure 5.9. In this test, the array was set to the L size to create a setup where the loops were strongly coupled and the element 12 was fed with a matched source. Initially, all the other loops were provided with the preamplifier models. In these conditions, the general decoupling relied mostly in the preamplifier decoupling. As a result, a very low induction in the non-fed loops occurred, as evidenced by the undetectable magnetic field outside of the sensitivity region of the loop 12. This result can be observed in the top row of Figure 5.9. To verify the efficacy of the preamplifier decoupling, the preamplifier circuit connected to the loop 13 was replaced by a matched load. Consequently, a magnetic field appeared in the sensitivity region of this loop due to the coupling with the fed loop, as can be seen in the bottom row of the figure.

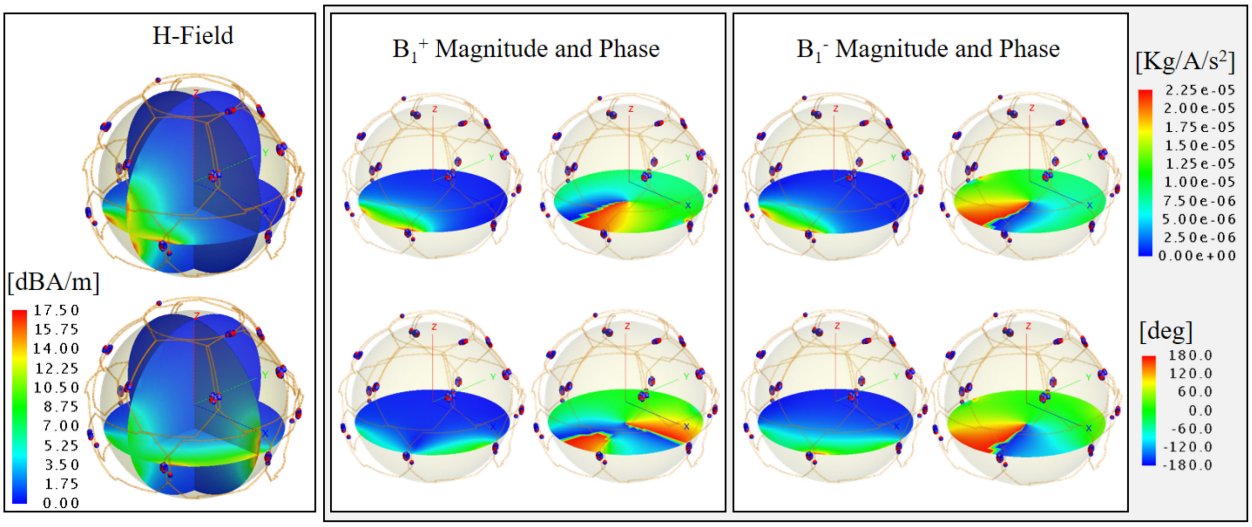

Figure 5.9 Sample of the preamplifier decoupling evaluation in the complete array.

The magnetic field intensity maps, obtained with the complete array, without and with preamplifiers are shown in Figure 5.10. Four axial slices were selected: at the center of the sphere, at a quarter of the diameter above the center, at a quarter below the center and at one eight of the diameter above the center. A sagittal and a coronal slice, both centered, were also selected. The color scales are the same for all maps. A general improvement in uniformity and symmetry in the complete coil size range is observed. A contribution to the non-uniformity in both conditions was obtained due to the 20-degree tilt of the coil. Some cancellations were reduced or eliminated.

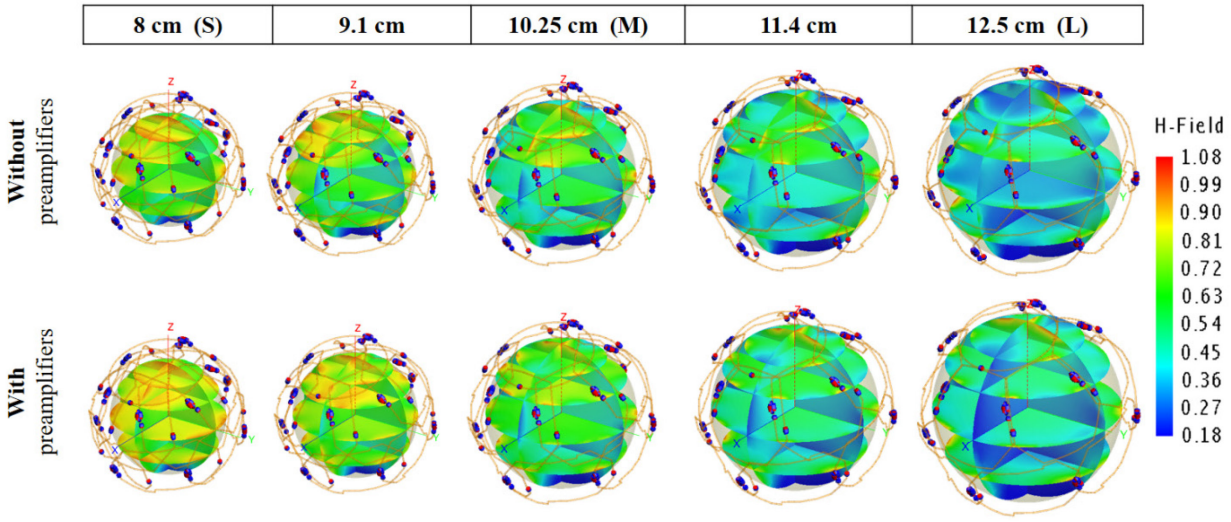

Figure 5.10 Magnetic field intensity maps comparison.

The B_1^- maps computed at three axial positions (a quarter of the diameter above the center of the sphere, the center, and a quarter below the center) are shown in the following figures. The color scaling was the same again for all the maps. The uniformity is lower in the upper slices for both configurations, as can be seen in Figure 5.11. The other two slices show a better uniformity. Figure 5.12 and Figure 5.13 present top views of those slices. The array was tilted 20 degrees from the *z*-axis during those simulations, as in the real configuration.

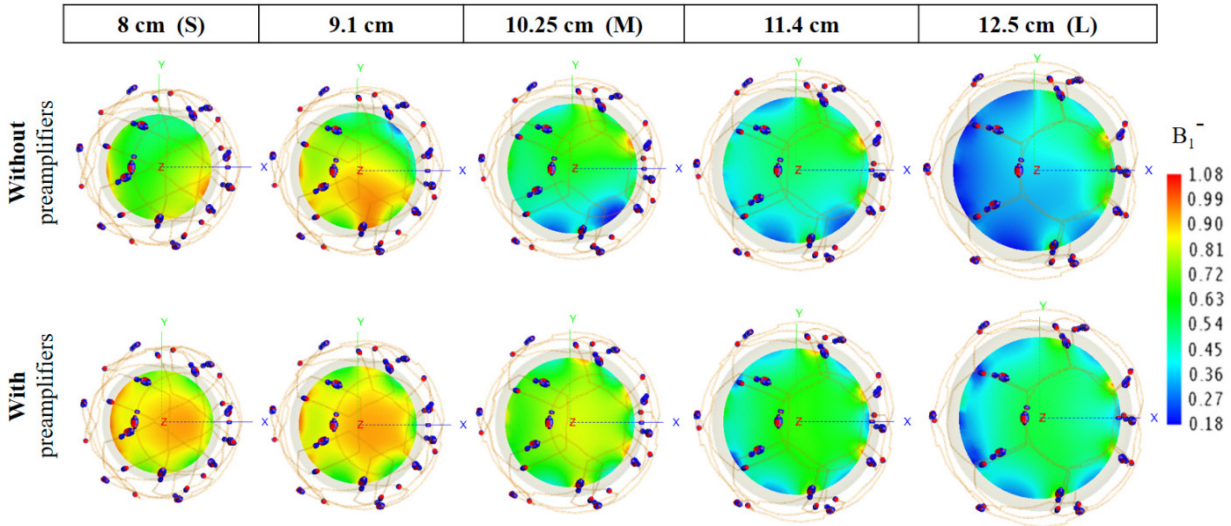

Figure 5.11 Axial B_1^- maps at a quarter of the sphere diameter above the center plane.

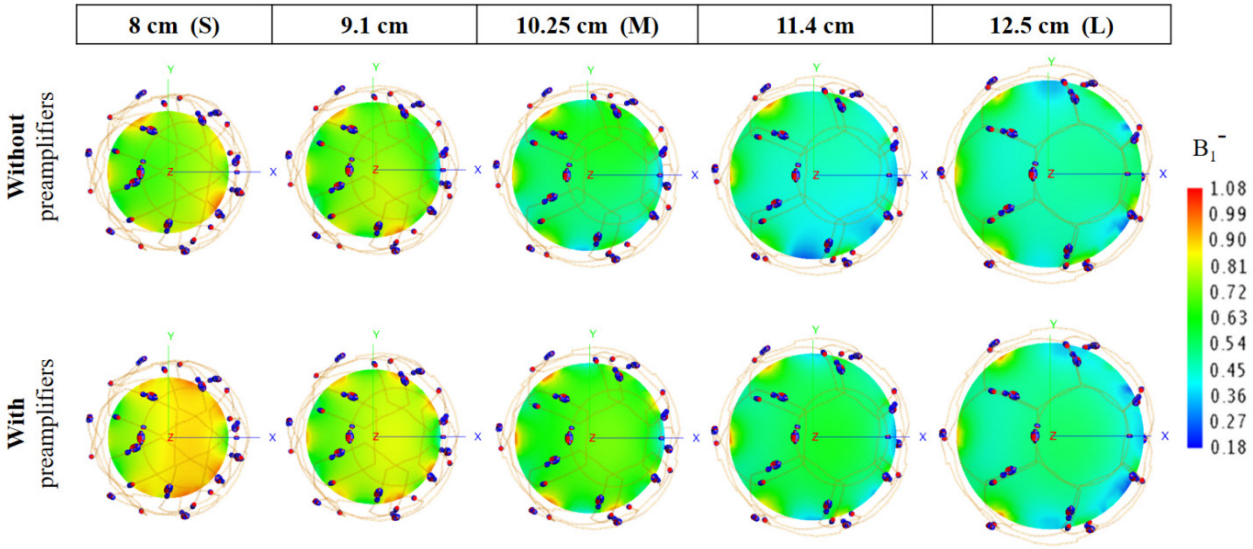

Figure 5.12 Axial B_1^- maps at the center plane.

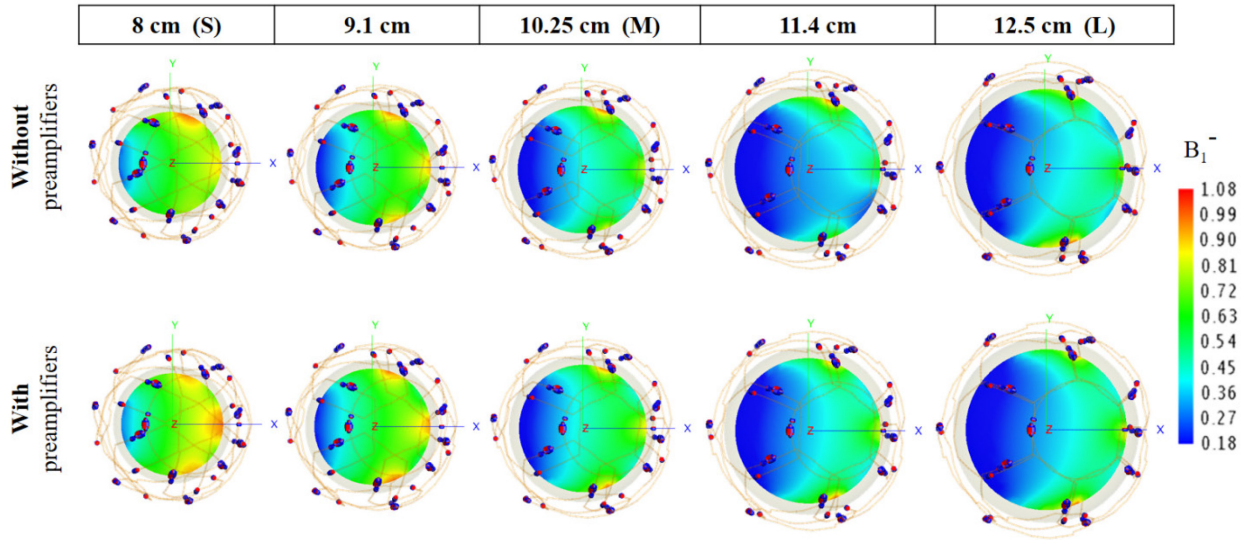

Figure 5.13 Axial B_1^- maps at one quarter of the sphere diameter below the center plane.

5.2 Construction

The coil operated appropriately in the complete size range after construction. Figure 5.14 shows pictures taken with the empty coil in both extreme dimensions. In the smallest dimension (a), the manually operated air valve (1) is open, the pneumatic system is at atmospheric pressure and the bellows (2) are extended. When vacuum is created in the system, by means of the hand pump (3), the bellows shrink and the elements are retracted until the coil gets to its largest dimensions (b). The air valve must remain closed while the subject is accommodated in the coil, and the vacuum

is kept by the check valve (4). The air valve must be open to let the coil adapt to the shape of the subject. A closer view, corresponding to the black rectangle, is shown in Figure 5.14c.

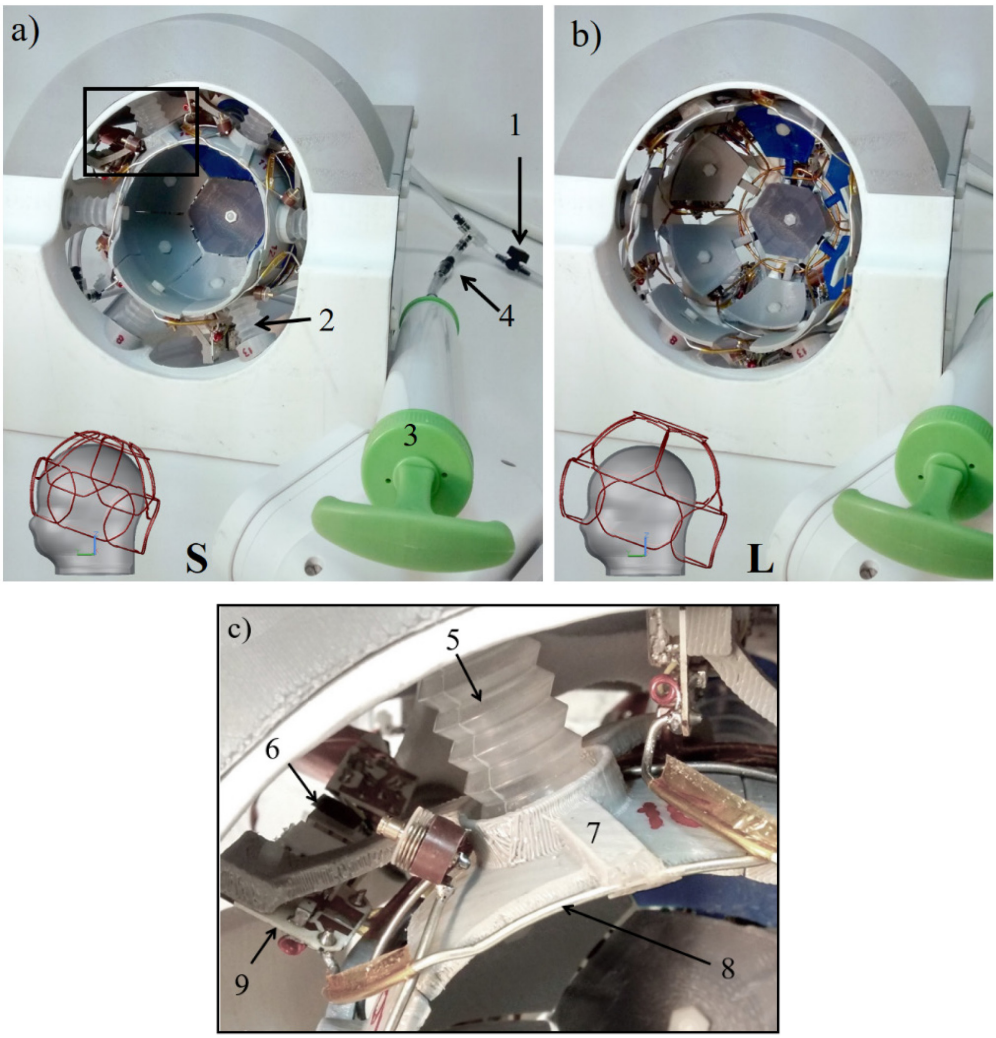

Figure 5.14 Photographs of the constructed coil in the extreme dimensions. Some important parts such as the manually operated air valve (1), the bellows (2), the hand pump (3) and the check valve (4) are shown in the working assembly. 3D drawings of the loops distributions are presented in the corresponding lower left corners of the coil pictures. c) Closed (S) coil detail on the element 10 showing the bellows (5), the preamplifier (6), the support (7), the wire loop (8) and the matching board (9).

The internal volume of the complete pneumatic system is small compared to the size of the hand pump. In consequence, the pump needs to be actuated only twice to completely open the coil, which takes a very short time. The pneumatic system could also be connected to a centralized vacuum

system normally available in scanner rooms or a vacuum pump used to operate holding systems for babies. In that case, the check valve would be replaced by another manual operated valve if needed.

5.3 Bench tests

5.3.1 Preliminary studies

5.3.1.1 Small 4-channel array

The initial test, with the loops matched to 310 Ohm, resulted in preamplifier decoupling values in the range of -37 dB, as can be seen in Figure 5.15.

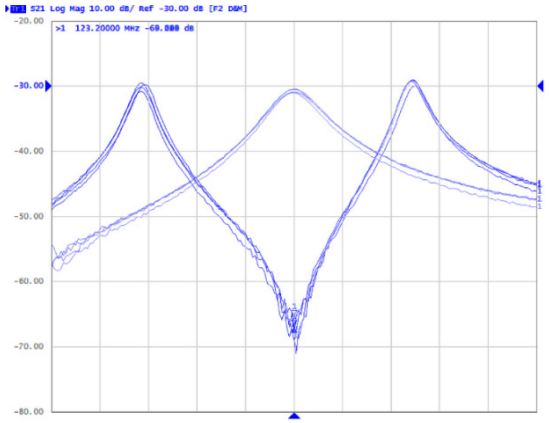

Figure 5.15 Preamplifier decoupling evaluation of the 4-channel array prototype.

In Figure 5.16 the results obtained after the noise match was adjusted to 50 Ohm are presented. The S_{11} magnitude in all channels was below -20 dB, before adding C1 (a). Consequently, the preamplifier decoupling was reduced to levels between -20.5 dB and -21.9 dB (b). Other parameters that reflect the quality of the array are the obtained decoupling between adjacent loops due to critical overlapping, which was below -20 dB (c), and the frequency response of all channels showing the typical dog-ear shape without the presence of oscillations.

5.3.1.2 150-Ohm WanTcom

The selected circuit allowed to adjust the impedance of the loop to nearly 150 Ohm before connecting Lm as can be seen in Figure 5.17a. The preamplifier decoupling level (b) was nearly -34 dB and the frequency response (c) was clean in terms of oscillations.

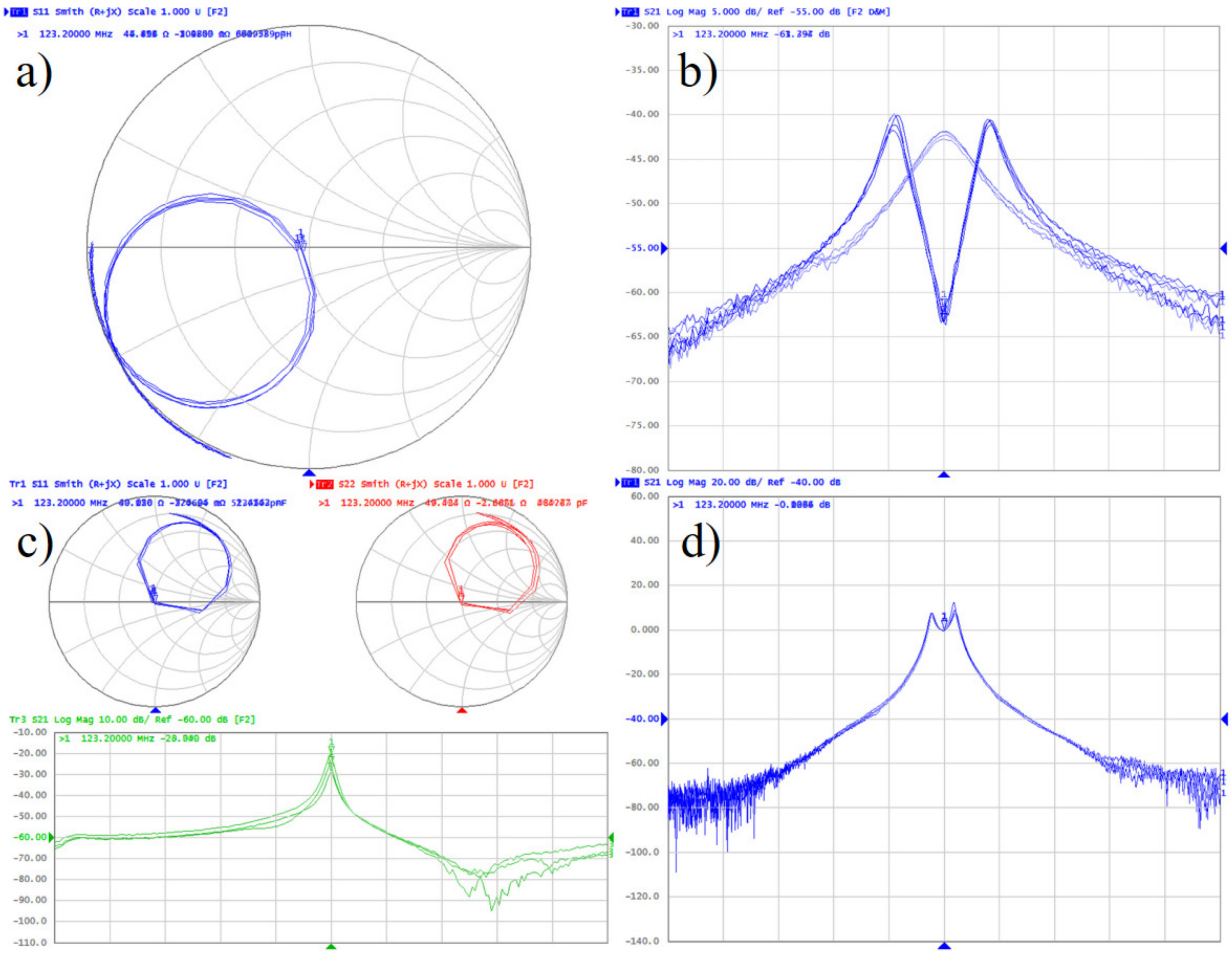

Figure 5.16 Bench test results of the Siemens 4-channel array with 50 Ohm noise match.

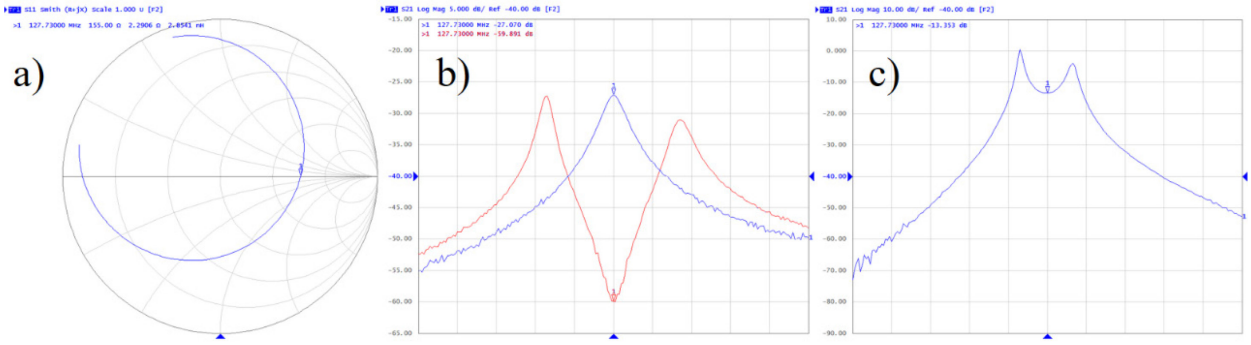

Figure 5.17 Parameters measured of the coil element made with the150-Ohm WanTcom preamplifier. The frequency span was 40 MHz.

In Figure 5.18 some results of the isolation test are shown. The S_{11} parameter measured in loop B before (a) and after (b) the connection of the transformer demonstrate the good impedance matching achieved. The S_{21} curves measured without the presence of the loop A is shown as a reference curve (light red) in c) and d). In c) the dark red curve is the S_{21} taken with the loop A loaded with 150 Ohm instead of the preamplifier. Here the tuning/matching condition of the loop B was affected due to the mutual inductance with loop A, as can be seen in the Smith chart. This obviously reduced the S_{21} value. If an exact S_{21} value is needed the transformer can be adjusted to match the new impedance to 50 Ohm. Finally, the preamplifier was plugged in the loop A, replacing the loading resistor, and a new S_{21} measurement was performed (d). In this case, the resulting value at the Larmor frequency was same as the reference, which means that B does not induce any current in A because of the preamplifier decoupling.

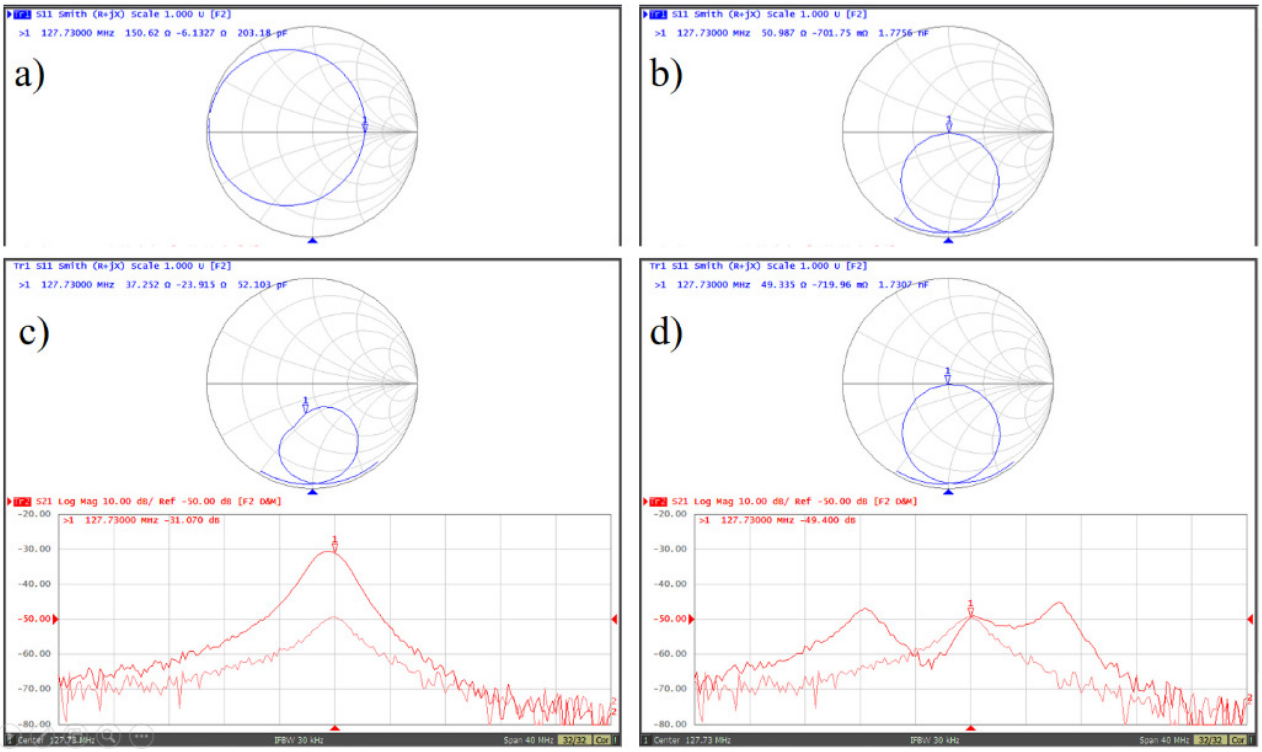

Figure 5.18 Results of preamplifier decoupling effectiveness test.

The results of the decoupling test performed with two complete receiver channels are shown in Figure 5.19 where the reference curve (light red) was taken only with the loop B present. Some changes in the curve were detected in frequencies which are separated from the Larmor frequency. However, the shape of the curve and the gain were not affected around the Larmor frequency

independently of the relative position between loops. This result means that, if the presence of the other channel is not affecting the output signal, an array with this kind of element might not need geometrical decoupling.

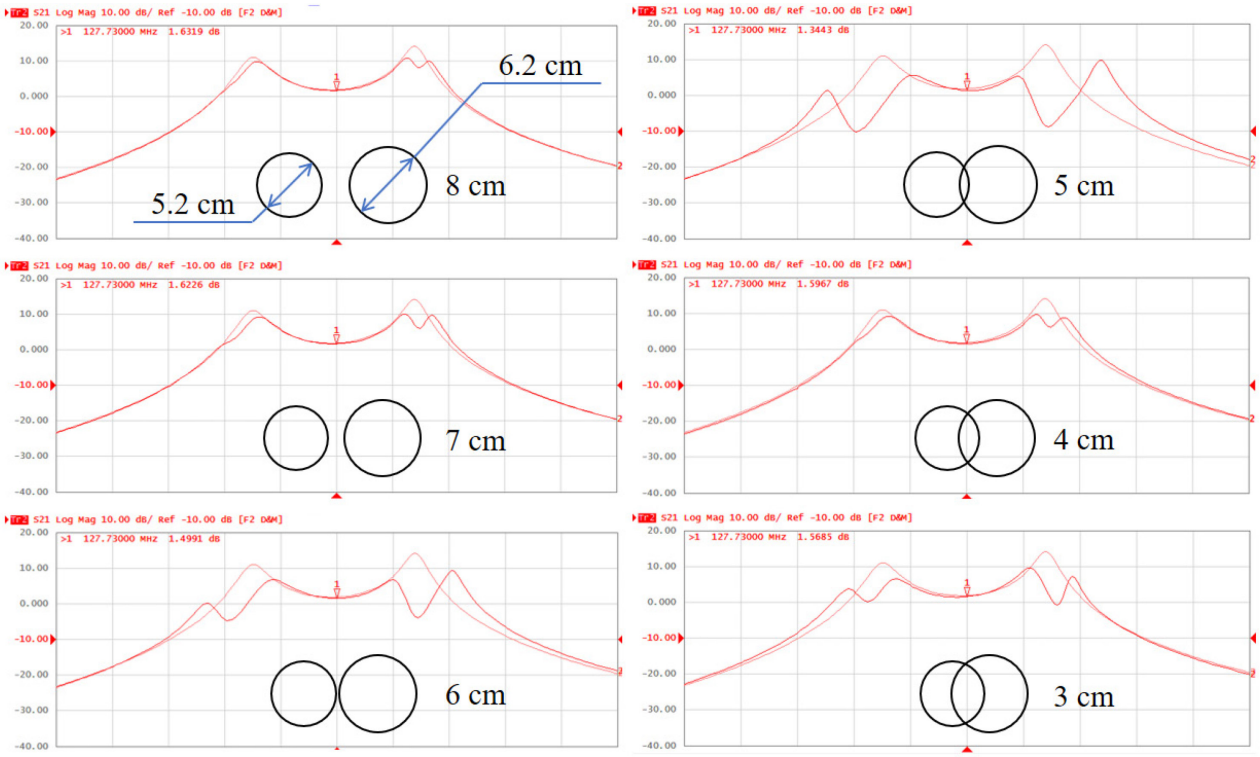

Figure 5.19 Preamplifier decoupling related to the distance between loop centers. A WanTcom WMM series miniature 6-pin preamplifier was used. The frequency span was 40 MHz.

The results of this test when repeated with the MPB-127R73-90 preamplifier were similar as can be observed in Figure 5.20. Two more measurements were performed around the geometrical decoupling position. Notice that the curves obtained near the geometrical decoupling in both tests (4 cm between loop centers) were less affected as expected.

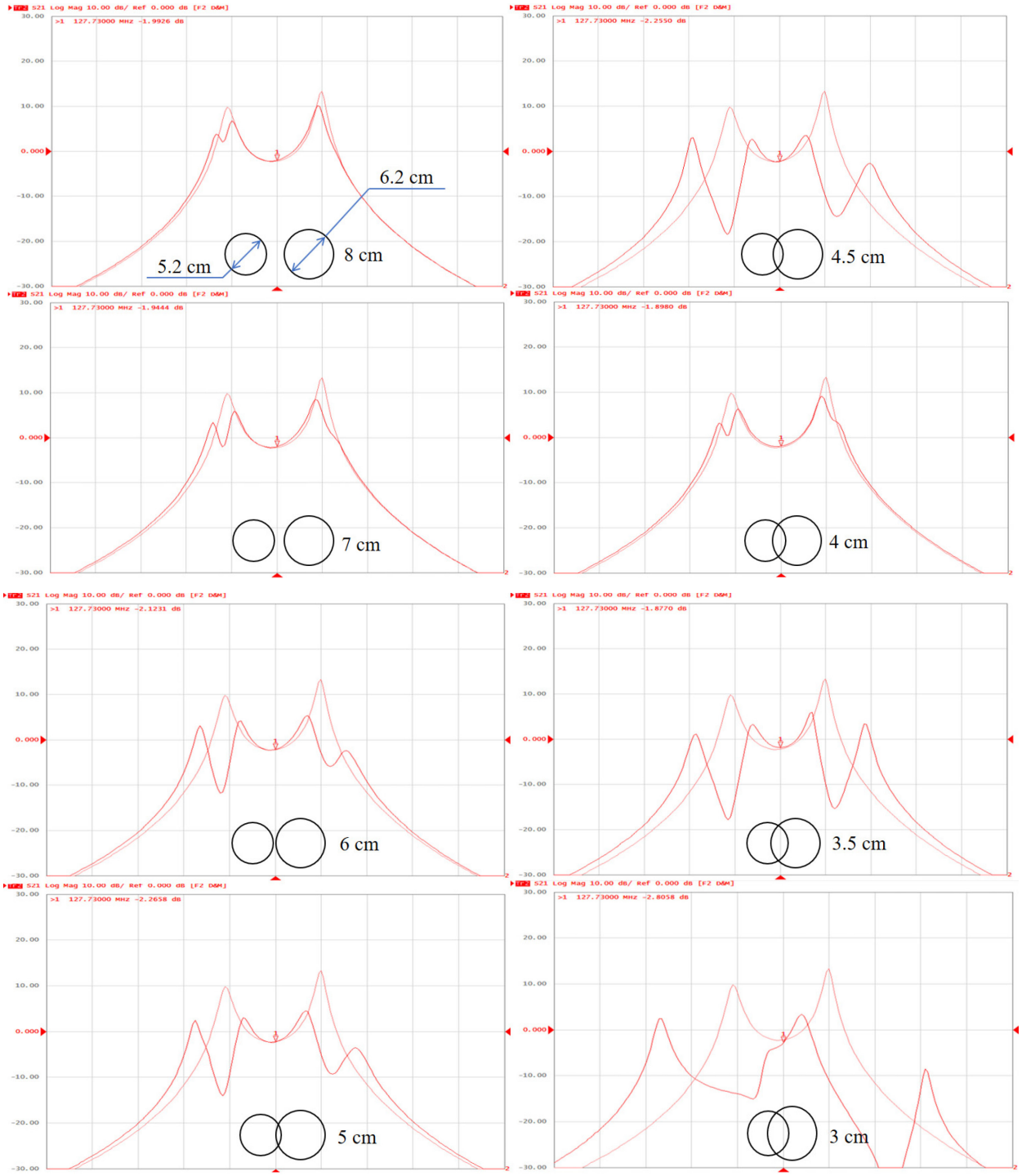

Figure 5.20 Preamplifier decoupling evaluation regarding the distance between loop centers with the MPB-127R73-90. The frequency span was 40 MHz.

5.3.2 Final coil tests

5.3.2.1 Loop impedance measurements

The measured impedance values of the selected loops are shown in the second column of Table 5.5. The capacitance values required to tune and match the loops to 175 Ohm are shown in the third column. As in the simulations, the presented values were found by means of a Smith chart tool after the verification of the calculated values. In the fourth column, the real capacitors used to tune and match loops, are presented. As mentioned before, only these three capacitor sets were used to assemble the loops according to their shape. The same variable capacitor (Ct1) was used to fine-tune the loops.

Table 5.5 Actual loop impedances and tuning/matching capacitors.

Loops	***Z* measured** (Network Analyzer)	**Caps Tune/Match** (Smith chart)	**Caps Tune/Match** (Used in array)
1	1.84 + j154 (L = 192 nH)	9.15 p / 69 p	(3-33 var) - 48 p / 48 p
2	1.53 + j157 (L = 196 nH)	8.86 p / 75 p	(3-33 var) - 43 p / 43 p
11	1.64 + j148 (L = 184 nH)	9.50 p / 73 p	(3-33 var) - 50 p / 50 p

5.3.2.2 Tuning and matching

In Table 5.6 the impedances measured at the tuned/matched loops outputs are presented. Notice that they were adjusted with the M phantom and were measured with the S and L phantoms without performing any adjustment. The impedances for the S and M loads were outside the recommended range but some reduction is expected due to the addition of the other components of the coil.

The loaded quality factor (Q_L), which were measured during this test to take advantage of the positioning of the elements, are shown in Table 5.7 and the maximum tuning frequency shift experienced by the loops when the load was added is presented in Table 5.8. The unloaded quality factor (Q_U) measured in the isolated loops is also shown. Using the mean values to calculate the Q_U/Q_L ratio for the S, M and L phantoms results in 3.88, 5.39 and 7.77 respectively, which guarantees that most of the noise present in the images will be generated by the sample and not by the coil. The measurements performed on the element 7 are shown in Figure 5.21 as an example.

Table 5.6 Impedance of the tuned/matched loops for all phantoms.

	S	M	L
1	321 – j14	245	157 – j5
2	306 – j41	237	161 + j39
3	299 – j36	239	148 + j31
4	328 + j24	239	154 – j27
5	315 + j30	239	157 + j21
6	365 – j42	270	187 + j11
7	314 – j39	257	159 + j7
8	286 + j19	223	162 + j31
9	257 – j16	213	157 – j3
10	279 + j15	225	155 – j40
11	283 – j38	249	167 – j20
12	263 – j21	219	173 + j5
13	275 – j42	258	166 – j19
Mean	299 – j15	239	162 + j2
σ	30 28	16	10 24

Table 5.7 Quality factors of the independent loops.

Loop	Q_U	Q_L		
		S	M	L
1	293.8	98.3	62.5	44.3
2	287.1	78.2	54.8	35.2
3	320.2	79.2	52.5	35.5
4	331.1	82.3	53.5	35.6
5	330.7	82.1	53.9	35.6
6	323.9	81.3	55.8	34.7
7	312.8	73.9	56.5	35.7
8	302.1	72.6	61.4	44.1
9	291.2	68.2	51.8	38.5
10	289.9	78.7	55.5	41.7
11	290.3	78.5	57.0	42.2
12	289.3	75.5	56.2	43.8
13	296.7	71.3	63.5	43.5
Mean	304.5	78.5	56.5	39.2
σ	16.8	7.4	3.7	4.0

Table 5.8 Tuning frequency shift due to the loading.

	S	M	L
f_0 shift MAX (MHz)	-0.39	-0.35	-0.69

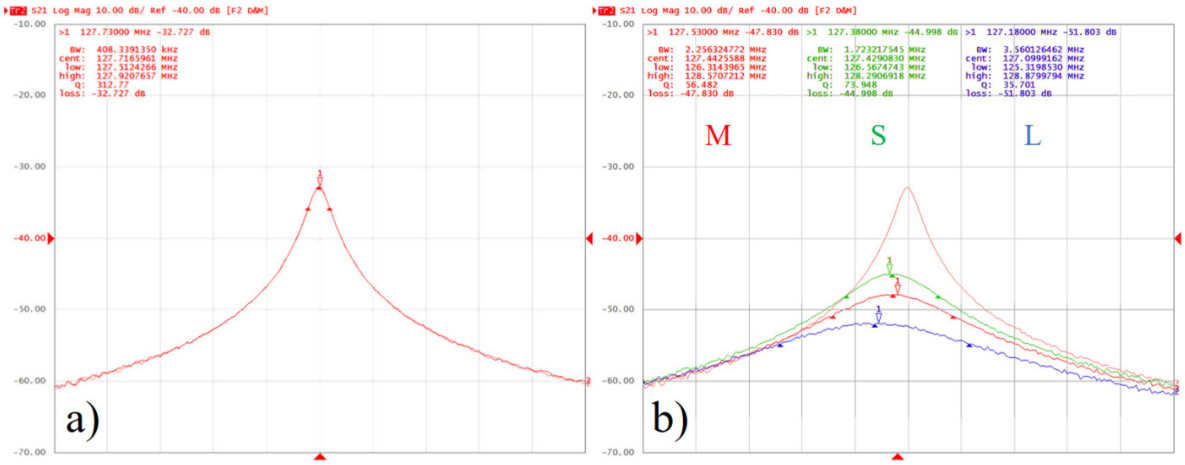

Figure 5.21 Sample of Q measurement (loop 7). a) Q_U. b) Overlapped Q_L measurements with the three phantoms. The frequency span was 10 MHz.

5.3.2.3 Active detuning

The active detuning level in all channels was always better than -40 dB, as shown in the example of Figure 4.39, which was enough to minimize the mutual inductance between selected loops.

5.3.2.4 Preamplifier decoupling

Adequate levels of preamplifier decoupling were achieved as they were always between -24.3 and -27.8 dB. These levels were measured taking as a reference the curve obtained with a 180Ohm resistor replacing the preamplifier. The curves detected in all elements were very similar and they all showed the known M-shape. All the measured curves are presented overlapped in Figure 5.22.

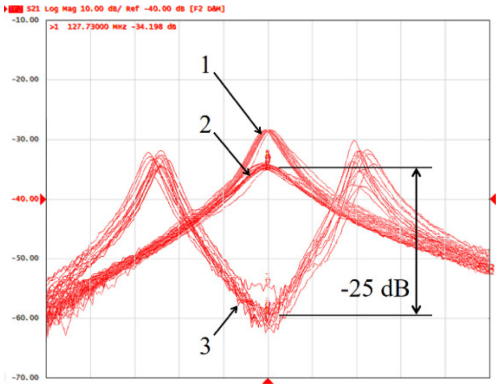

Figure 5.22 Preamplifier decoupling assessment of all channels. An average of -25 dB was achieved. 1) Curves measured with the loop terminals open. 2) Loops terminals loaded with a 180Ohm resistor. 3) Preamplifiers connected to the loops.

5.3.2.5 Impedance and Q_L in the array

After the array was assembled, and all loops were re-tuned with the M phantom, their impedances were measured. The resulting values are presented in Table 5.9 in two conditions: with the non-tested elements detuned and non-detuned. The values for the other coil sizes are also included. The curves corresponding to those measurements are shown in Figure 5.23. The impedance of the loops with the M phantom could not be adjusted to exactly 175 Ohm when the non-tested elements were detuned, which is the condition that better resembles the isolated loops.

After turning off the bias current of the PIN diodes, the shape of the curves changed, as could be expected. This shape change was substantial at frequencies that are far from the Larmor frequency. However, around this frequency, the shape was not largely affected although the impedance values were more dispersed. In addition, the impedance at the Larmor frequency was in the recommended range of noise match (50 to 200 Ohm), except for three cases. The maximum tuning frequency shifts, which were not important, were also recorded and shown in Table 5.10.

Table 5.9 Impedance measurements after the assembly of the array.

	S		**M**		**L**	
	Detuning	**No detuning**	**Detuning**	**No detuning**	**Detuning**	**No detuning**
1	206 – j166	188 – j104	201 – j9	187 + j17	148 – j42	142 – j31
2	205 – j17	172 – j66	165 – j7	95 – j49	120 – j24	78 – j47
3	286 – j8	232 – j15	181 – j17	132 – j54	129 – j3	107 – j32
4	222 + j40	188 + j58	158 – j6	150 – j35	122 – j21	142 – j51
5	225 + j68	181 + j125	180 + j5	235 – j23	130 – j20	166 – j49
6	280 + j15	219 – j30	185 – j8	159 – j94	150 – j19	129 – j74
7	229 – j14	152 + j11	175 – j3	150 – j62	131 – j20	104 – j64
8	232 + j2	164 – j31	194 – j6	140 – j60	138 – j22	94 – j47
9	235 + j 29	123 + j27	183 – j7	121 – j37	134 – j17	94 – j37
10	236 + j 26	144 + j16	189 – j7	126 – j23	139 – j17	99 – j24
11	238 + j 14	146 – j4	219 – j10	177 – j7	154 – j28	155 – j36
12	234 – j4	164 + j36	186 – j3	128 – j17	135 – j34	104 – j37
13	212 + j 52	127 + j 31	179 – j6	145 + j15	138 – j25	114 – j18
Mean	234 + j3	169 + j4	184 – j6	150 – j34	136 – j23	118 – j42
σ	25 57	33 57	15 5	35 30	10 9	27 16

Table 5.10 Frequency shift with respect to the tuning condition (M size).

	S		**M**		**L**	
	Detun.	**No detun.**	**Detun.**	**No detun.**	**Detun.**	**No detun.**
f_0 shift MAX (MHz)	-0.5	0.5	0	-1.11	-0.2	-0.87

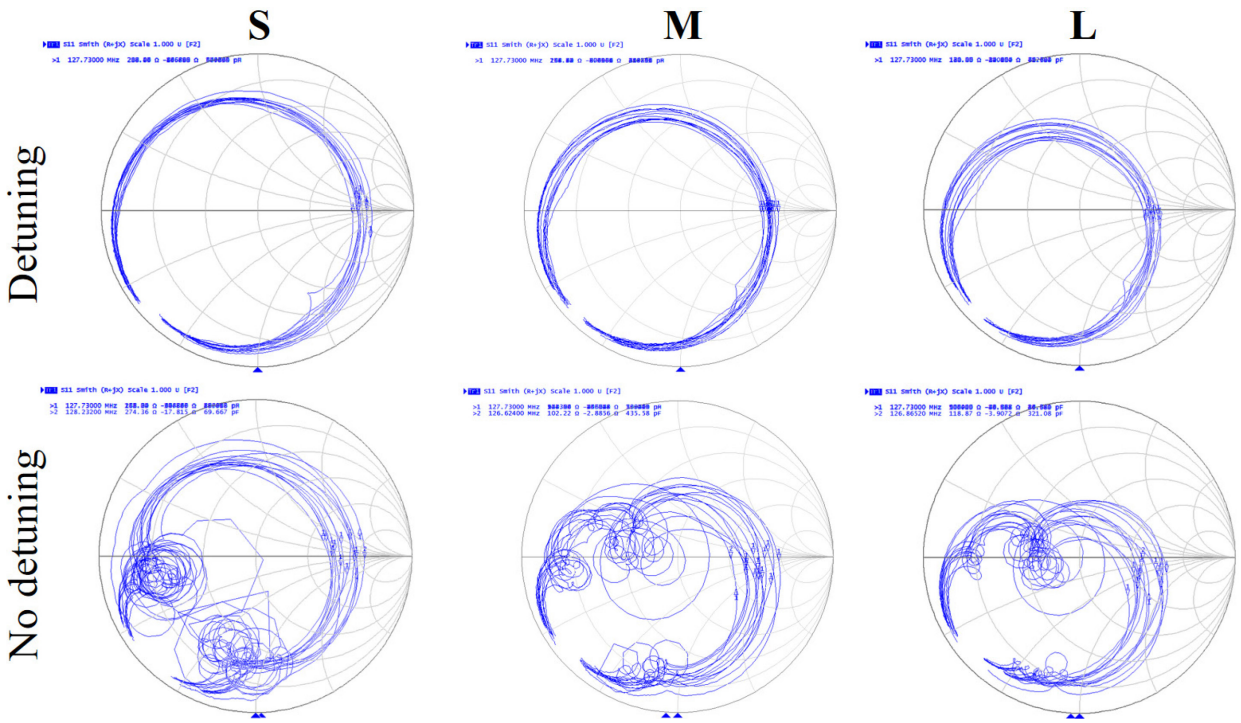

Figure 5.23 Impedance measurements in the assembled array. The curves of the 13 elements are overlapped. The frequency span is 40 MHz.

The Q_L measurements performed during this test in the completely assembled array are shown in Table 5.11. A general reduction compared to the Q values obtained with the isolated loops is observed. These reductions were 17.1 %, 14.5 % and 8.4 % for the S, M and L phantoms respectively.

5.3.2.6 Array coupling

The result of the general coupling in the array was limited to the elements 1 to 7 to reduce the test time. To quickly obtain an idea, S_{21} matrices were created with the three loads. They are presented in Figure 5.24. Low decoupling was obtained in general, including with the M phantom where the configuration was closer to critical overlapping.

Table 5.11 Q_L test in the array.

	Q_L		
	S	**M**	**L**
1	84.7	48.3	35.7
2	65.5	46.1	36.1
3	66.4	45.3	32.5
4	59.4	39.7	31.0
5	65.1	46.4	34.4
6	62.9	43.3	34.4
7	57.3	47.0	34.2
8	67.6	54.8	37.8
9	59.3	48.2	36.6
10	56.3	48.8	37.2
11	64.3	55.4	39.8
12	68.1	51.0	38.0
13	69.0	53.4	39.1
Mean	65.1	48.3	35.9
σ	6.9	4.3	2.5

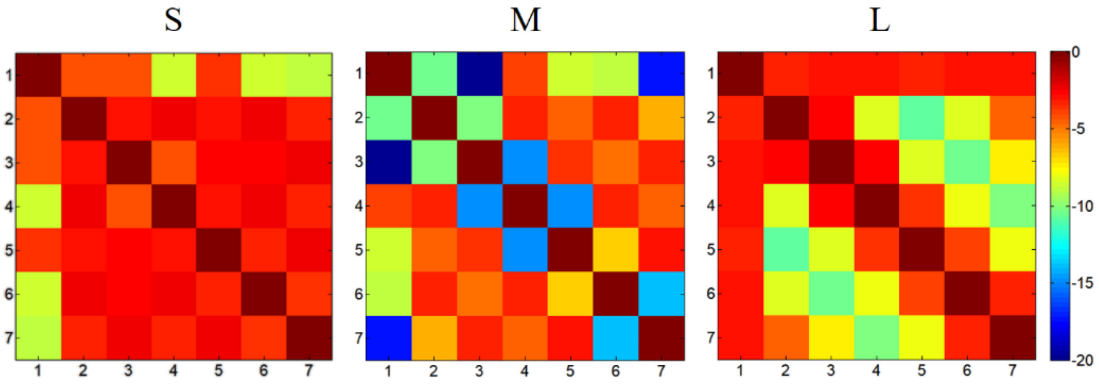

Figure 5.24 S_{21} values between pairs of loops (1 to 7) presented as color matrices.

5.3.2.7 Loop sensitivity profile

The sensitivity profiles (S_{21}) of all channels with all phantoms are shown in Figure 5.25. They showed that the typical "dog-ear" shape was not severely distorted, particularly in the proximities of the Larmor frequency. In addition, the high stability of the amplifiers was achieved, since oscillation peaks were not detected, with and without loads, in the full range of the network analyzer (100 kHz to 3 GHz).

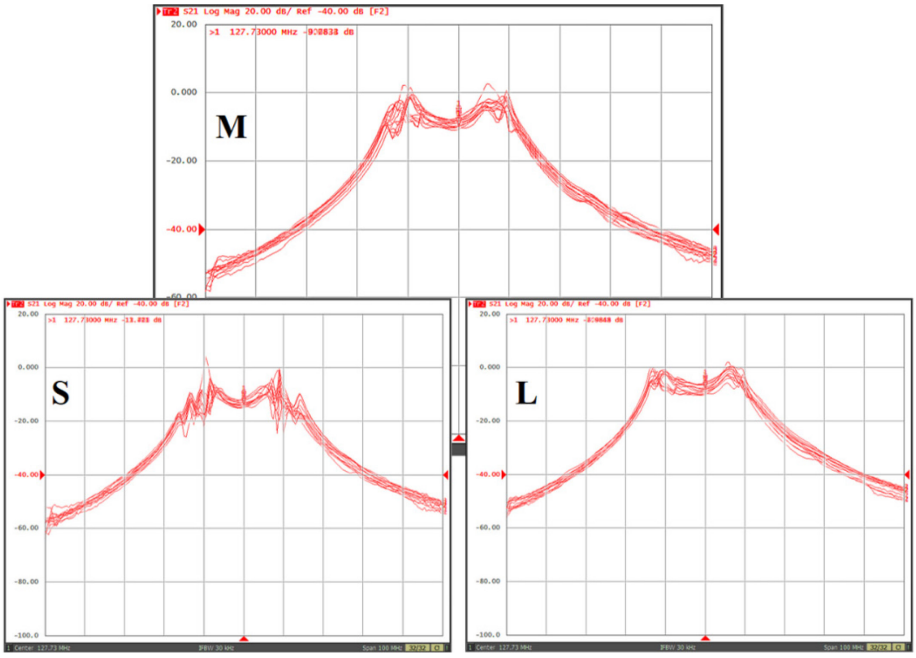

Figure 5.25 Overlapped sensitivity profiles of all coil elements for each load size.

5.4 Scanner tests

5.4.1 Preliminary studies (small 4-channel array)

The scanner tests results of the small 4-channel array are shown in Figure 5.26. The noise correlation matrix (a) confirms that the array has a good decoupling. The image (b) obtained from the phantom used during the bench tests shows a uniform pattern, corresponding to an array of small elements, with no cancellations or artifacts caused by coupling. This image was used to compute the SNR map (c) which also shows the typical pattern.

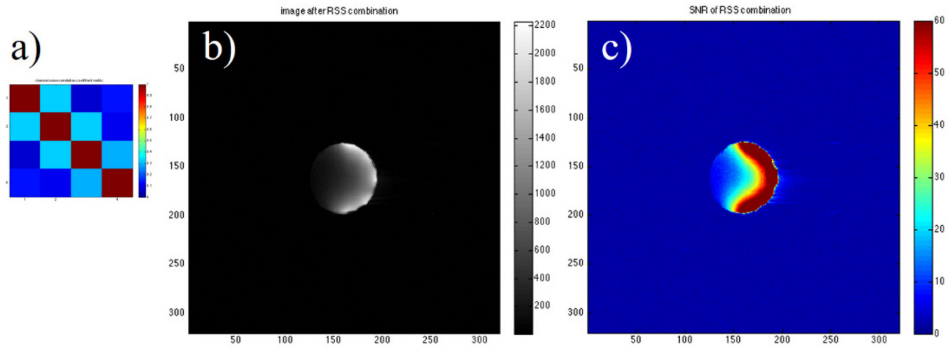

Figure 5.26 Noise correlation matrix and SNR map of the 4-channel array.

The results of the scans performed with the non-homogeneous sample are shown in Figure 5.27. Small details can be seen in the individual channel images (a) and the reconstruction (b). It can be noticed also that the parallel image (c), has acceptable quality and the acceleration artifacts are not visible.

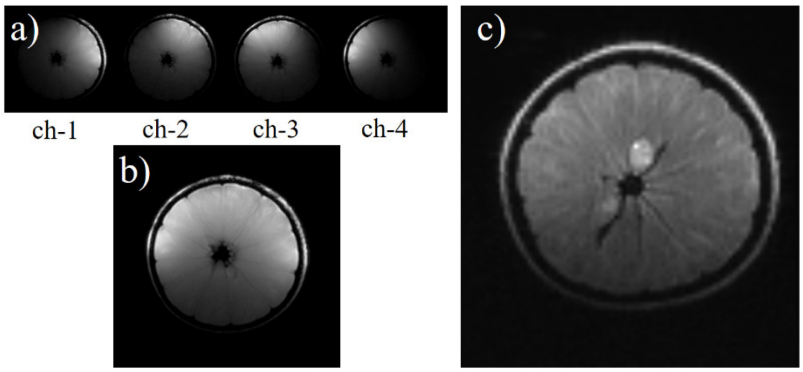

Figure 5.27 Images acquired on a non-homogeneous sample.

5.4.2 Final coil tests

5.4.2.1 Phantom images

The preliminary scanner tests of the final coil, performed with the 10cm spherical phantom, resulted in improvements in SNR compared to the commercial head coil made for adults (32-channel) as can be seen in Figure 5.28. However, some line-shaped and dot-shaped artifacts, caused by oscillations, were observed in some images. In addition, low signal regions, likely provoked by the lack of decoupling, are also observed in both slices.

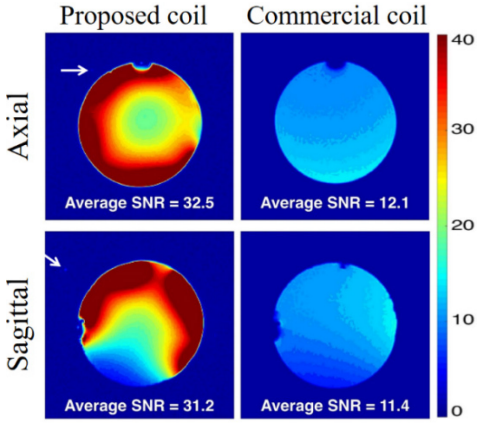

Figure 5.28 Axial and sagittal SNR maps computed for the 10cm spherical phantom. Small dot-shaped oscillation artifacts are pointed with white arrows.

Additional tests performed with the three head-shaped phantoms and both coils lead to similar results. A noise correlation matrix that shows a substantial degree of coupling between channels is presented in Figure 5.29 (top center). This matrix was computed from the axial slice of the M-phantom. The matrix elements with high correlation were caused by oscillations detected in channels 2-5, 7 and 13 for this coil dimension. The noise acquired from each channel and the reconstruction are presented also in Figure 5.29 (bottom). Oscillation artifacts are clearly observed in the affected channels. For the other dimensions, the noise correlation matrices show adequate results.

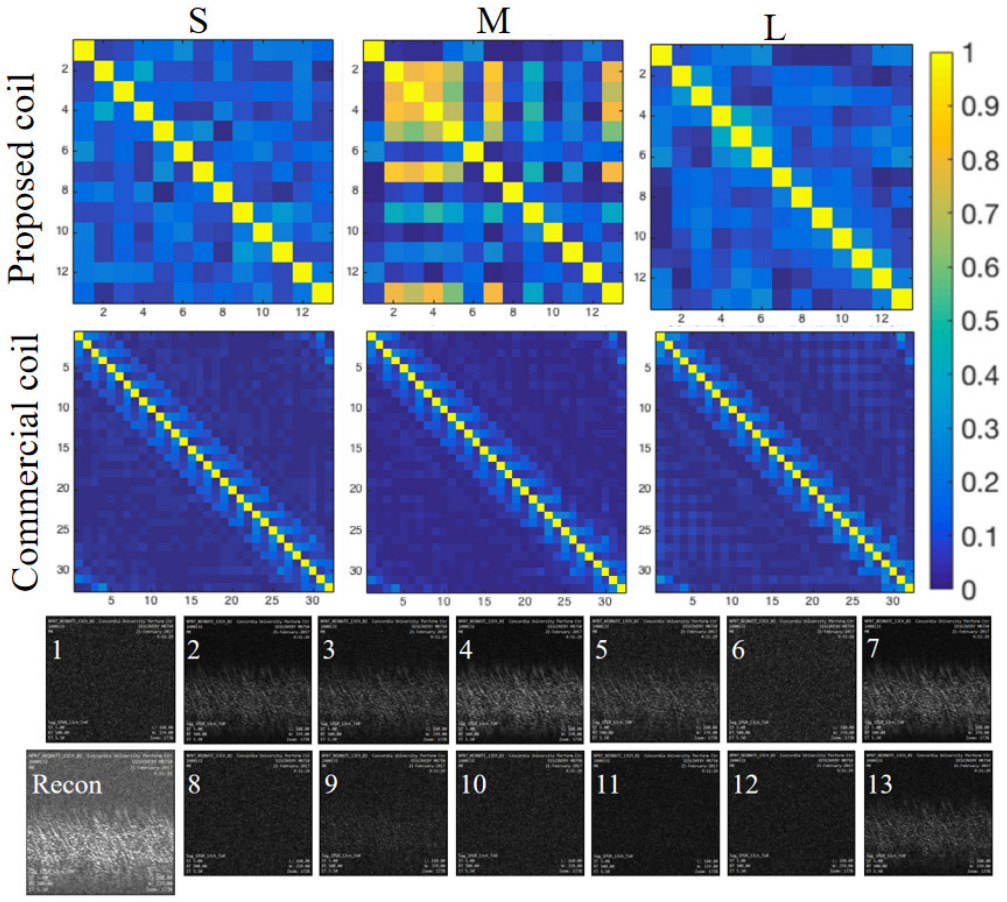

Figure 5.29 Noise correlation matrices computed for all phantoms and both coils and noise acquisition from each channel of the proposed coil with the M phantom.

Axial and sagittal images acquired with the M phantom are presented in Figure 5.30. The uniformity pattern observed in the reconstructions is not as anticipated. Some oscillation artifacts are observed in the axial images. Comparing to the noise acquisitions, the artifacts are present in different channels (3, 4, 7, 11-13). Notice that the channels with higher sensitivity contribution to

the axial slice (2, 6, 7, 9, 10, 11 and 12) do not have similar intensity distributions. The same behavior is observed in the loops that contribute to the sagittal slices (1, 4, 7, 8, 10, 11 and 13). While some of these loops had a very low intensity, other loops contributed to the images helping to improve the distributions.

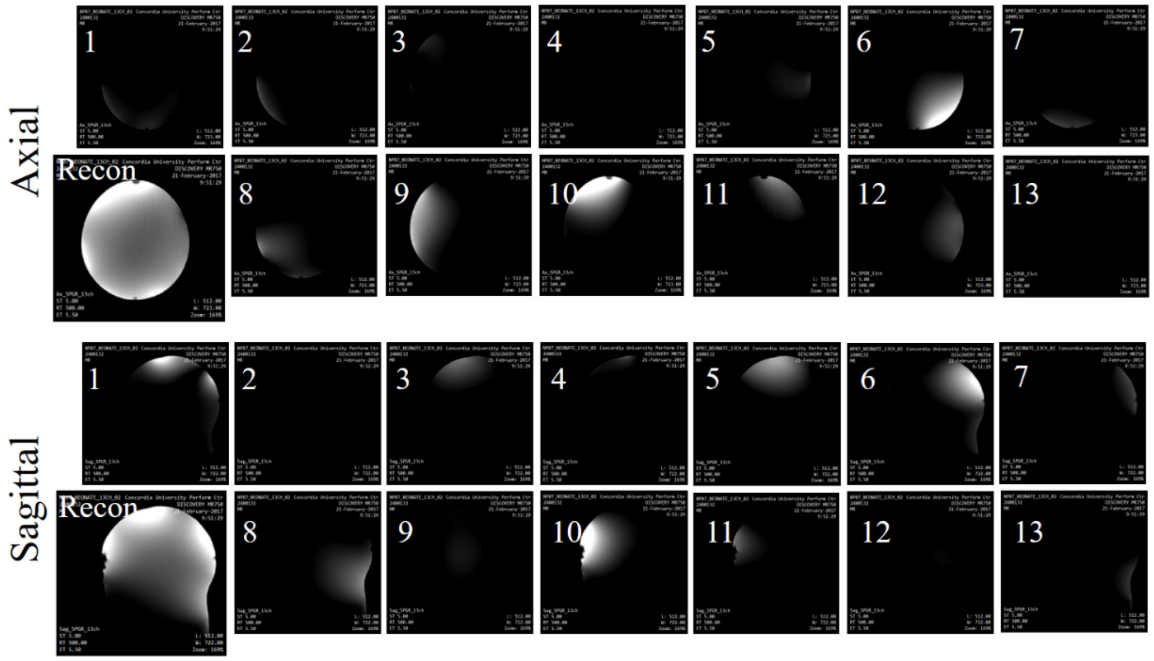

Figure 5.30 Axial and sagittal slices acquired with the proposed coil loaded with the M phantom.

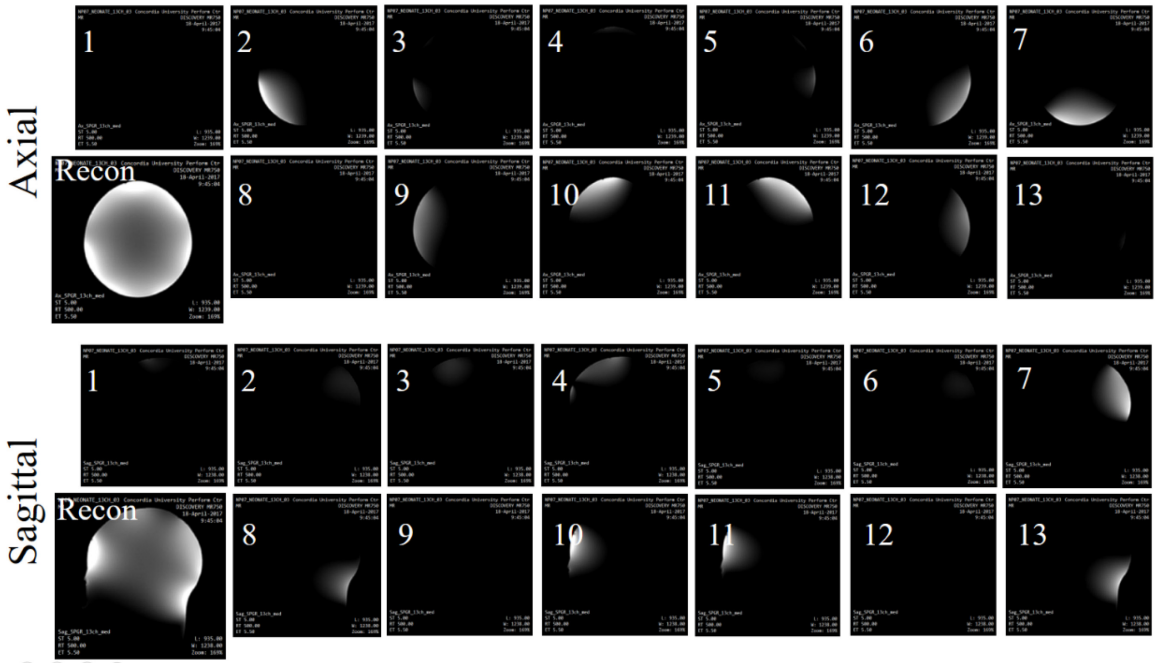

Figure 5.31 Previous axial and sagittal acquisitions repeated after some improvements.

After some technical changes implemented on the coil, the same set of images showed improvements. The new acquisitions are shown in Figure 5.31. Notice that the channels that contribute to both slices have a more even distribution of intensities. However, channels 1 and 4 show lower than expected contribution to the sagittal slice.

The final scanner tests confirmed that the constructed coil exhibits satisfactory parameters compared to the commercial coil. Axial and sagittal Spoiled Gradient Recalled (SPGR) images are shown in Figure 5.32 and Figure 5.33 respectively. All images have the same intensity and contrast adjustment. As can be observed, there are not visible oscillation artifacts and the images are clean of total cancellations due to coupling among elements. However, the intensity patterns near the edges of the images are not totally symmetric.

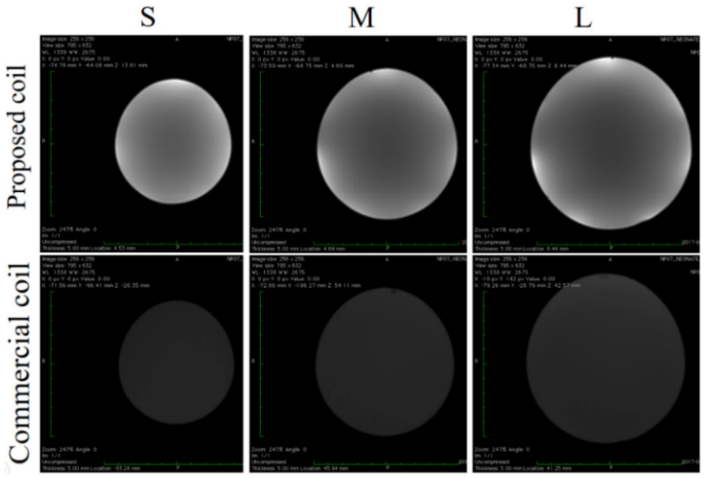

Figure 5.32 Axial images of the three constructed phantoms. The intensity scaling is the same everywhere.

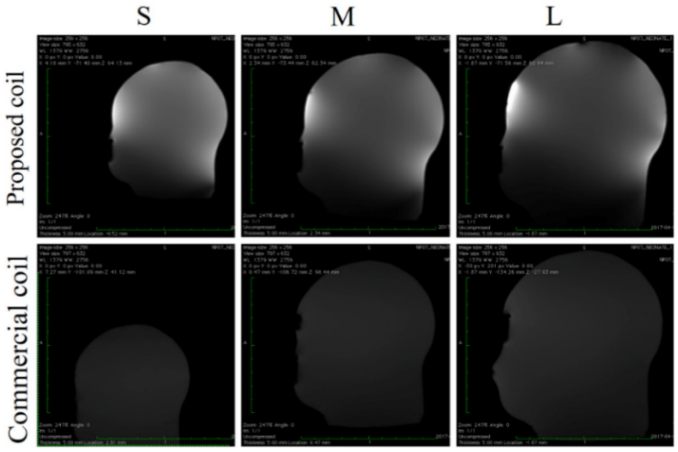

Figure 5.33 Sagittal images of all phantoms. The intensity scaling is the same everywhere.

5.4.2.2 Noise correlation matrix

The noise correlation matrices computed from the zero-transmit-power acquisitions showed acceptable decoupling in all studied dimensions as can be observed in Figure 5.34. They show low levels of noise correlation obtained with the proposed coil, as the maximum average value was 0.14. A maximum correlation of 0.31 is observed for the S size, while for the commercial coil the maximum was 0.28 for the L size. A table containing the average values of all off-diagonal elements is included in Figure 5.34. As could be anticipated, the average correlations are higher in the proposed coil (1.9 to 3.5-fold) being higher as the dimensions decrease. For the commercial coil, the average correlation slightly increases when the sample dimension is larger, as expected.

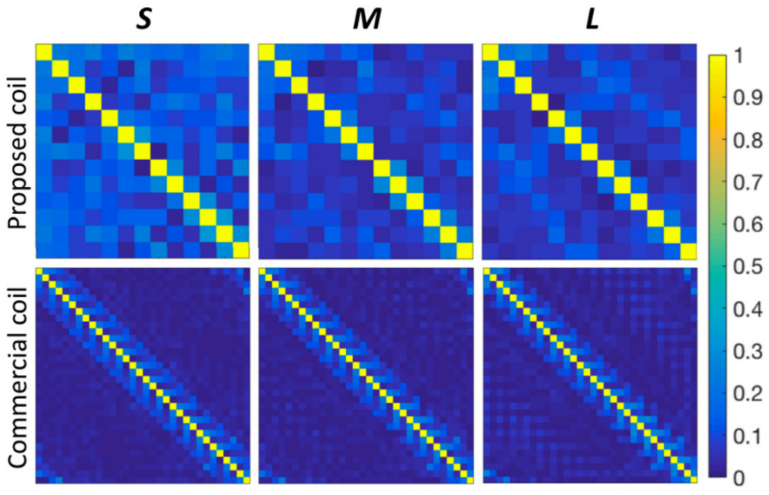

	S	M	L
Proposed coil	0.140	0.091	0.087
Commercial coil	0.040	0.041	0.046

Figure 5.34 Noise correlation matrices computed for both coils and off-diagonal averages.

5.4.2.3 SNR maps

The SNR maps computed according to covariance weighted root sum of squares method on the images presented above are shown in Figure 5.35 (axial) and Figure 5.36 (sagittal). Increased values for the proposed coil in almost all studied configurations, mainly in the cortex region, were revealed. The average SNR, computed in the whole axial slices acquired with the proposed coil were 68%, 35% and 16% higher for the S, M and L phantoms respectively. In the sagittal slices, the average SNR values inside a selected region of interest comprising the head part of the phantoms, resulted in increases of 48% and 14% for the S and M phantoms respectively. However,

a decrease of 2% was obtained with the L phantom. Darker than expected regions are observed in the proximities of elements 1 and 4. They are more evident in the sagittal images of the M and L phantoms. A similar pattern is observed in both image groups.

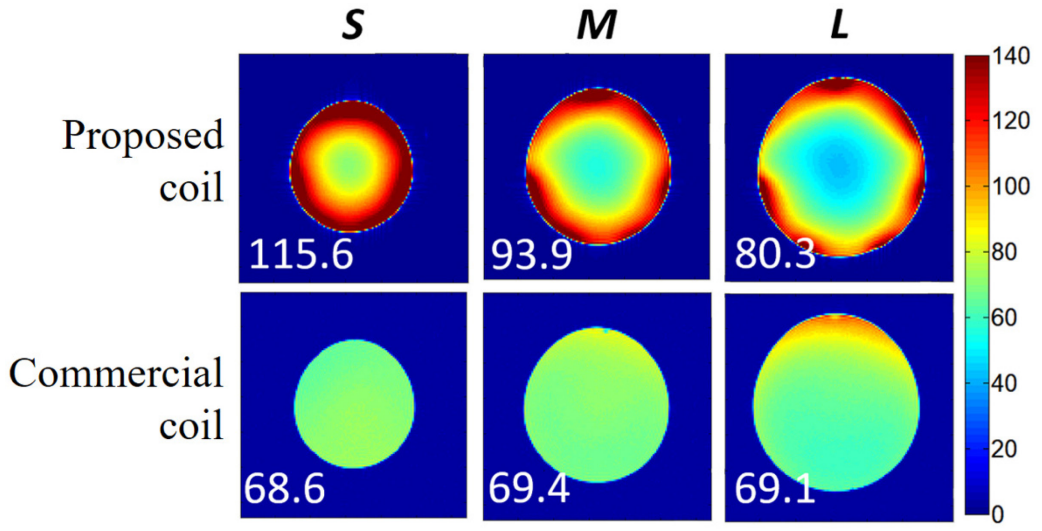

Figure 5.35 Axial SNR maps of all the three constructed phantoms.

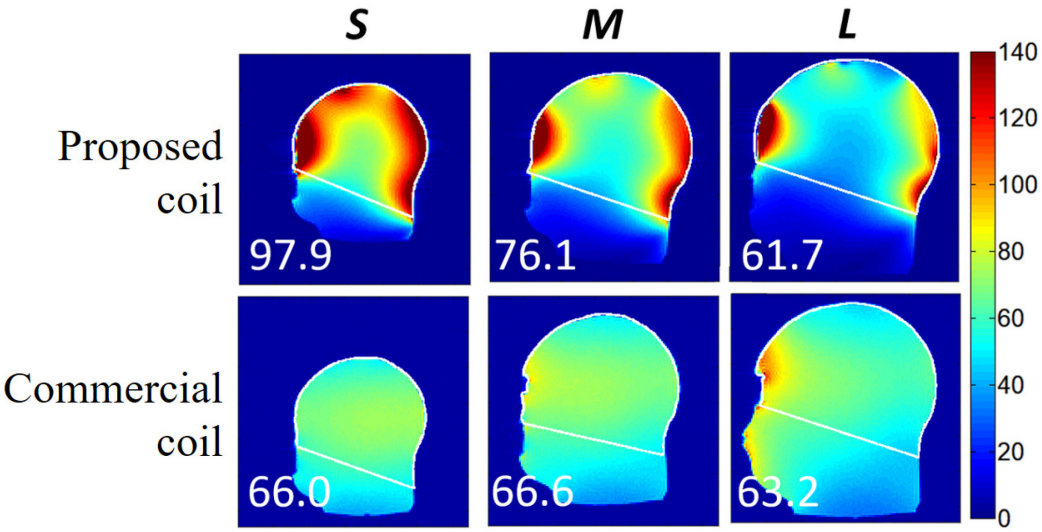

Figure 5.36 Sagittal SNR maps of all phantoms. The edges of the masks used to select the region of interest are shown in each image.

CHAPTER 6 GENERAL DISCUSSION

The quality of some important MRI studies of the neonatal brain is currently limited by the low availability of optimized coils. The low number of existent commercial coils do not perform optimally for all head sizes due to their fixed size, while adjustable size coils are not commercially available. On the other hand, some presented solutions show weaknesses that reduce the likelihood of becoming a standard coil. An important difficulty to overcome is the high variability of the neonatal head. The development of a coil that operates in an optimal way with different head sizes may facilitate the diagnosis and treatment of a variety of neonatal brain injuries. This work presents a new receiver RF array coil, that can adapt its dimensions to neonate heads ranging from premature of 27 weeks to 1.5-month-old babies.

6.1 Coil structure

The proposed coil has a complex and mobile structure. All elements are moved independently and simultaneously, keeping a nearly spherical structure in the complete range. For these reasons, it was extremely important to perform a careful modelling and simulation stage. Notice that two conditions must be simultaneously satisfied in the complete adjustability range: an adequate performance of the coil and the non-existence of mechanical interferences among electric, pneumatic and support parts. Not performing this stage, could lead to several design-building iterations, which would be more time consuming.

The isolation between channels and magnetic field distribution, obtained by simulations, helped to predict that the proposed structure could be a suitable alternative approach to previously proposed adjustable head arrays [11], [12], [13], [14]. There is evidence of the implementation of only one of these ideas [12], but no evidence was found about its availability as a commercial coil. One advantage of the proposed coil is the better adaptability to approximately spherical structures, such as the head, through the selected size range. This peculiarity makes it possible to obtain high SNR values in the complete cortex region for different head sizes. For a fixed-size coil the SNR in the cortex region depends on the size of the head and its position inside the coil. A poorer SNR distribution could be expected from arrays divided in sections, such as those mentioned before, where the relative position between different sections could create gaps between them or cubic coil shapes.

The proposed coil reduces costs and may simplify imaging protocols compared to the use of multiple coils [9]. It is worth mentioning that the price of a preamplifier could be around $1,000, which added to the other components and the additional expenses make a single coil costly.

It is also advantageous that the proposed array does not apply active force on the infant head. Different actuators were proposed by the authors of the mentioned adjustable arrays to push the elements toward the head. Since a mechanical failure event is a main concern in these cases, the implementation of a safety system to protect the fragile head of the neonates from excessive pressure is mandatory, which increases costs and complexity. In the method proposed in this work, the elements are only driven by the bellows, which can be designed and manufactured with parameters that ensure safety. Thus, the maximum pressure applied on the neonate head will be limited to the known flexibility of the bellows. In consequence, an expensive safety system including sensors, control loops, calibration, etc., is not required.

A simple pneumatic system was proposed here to control the shape of the bellows and the coil size. The system consists of tubes and valves that control the air flow only during the positioning and removal of the patient. In those moments, a vacuum is created inside the system to hold the coil elements in the retracted position. During the scan, the system is open to the atmospheric pressure and resting. A small hand pump was used during the development of the coil but other vacuum sources, such as the vacuum system already present in the scan rooms, could be used in a final product. In terms of time consumption, the operation of the vacuum source will only add a few seconds to the workflow of the MRI study. The previously presented ideas do not show a real implementation of a mechanism for moving the coil sections, probably because of the complexity of the proposed actuators and control systems.

The project was focused on a coil for the neonate head due to the importance of this age group. Nevertheless, the proposed method can be applied to coils dedicated to other body parts with a large variability in terms of dimensions, such as knees and breasts, or even for the head in other age groups when optimized SNR is required. The problem addressed in this work is the same for these cases: a reduced SNR is obtained when a small part is scanned with a standard coil made to scan as much as possible from the general population.

6.2 Coil modelling

The modelling of the coil elements helped to find approximate values for the tuning and matching components. The inductances of the simulated loops were in the range of 88 to 92% of the measured inductance on the real loops. A contribution to the differences may be caused by the use of the network analyser to measure the impedance of the loops. Even though a calibration was performed it is known that lower accuracy is expected when the measured impedance is close to the zero-resistance circle. The values of the matching capacitors were between 77 and 83% of the final values. This difference is expected, since the simulated array only includes the wire loops. In addition, the final capacitor values were selected to obtain the desired impedance while all the other parts of the array were present. Since the preamplifiers are connected directly to the loops, the density of metallic parts around the array of loops is high, which adds additional capacitance. Consequently, the final values were empirically found in the workbench after the array was assembled.

The study by simulations of the impedance of the isolated loops with different loads reported values that were out of the recommended impedance range (according to the selected preamplifier) for the two smallest coil sizes. They were 26-33% higher for the smallest size (8cm) and 17-19% higher for the next size (9.1cm). Since some impedance reduction was expected from the inclusion of the other parts of the array, the 175 Ohm impedance for the M size coil was kept for the next simulations. The impedances for the largest samples were smaller but they remained inside the recommended range (50 to 200 Ohm).

MRI coil designers frequently choose critical overlapping to adjust the geometry of the coils. For this reason, the loops were initially geometrically decoupled for the M size load. This was a time-consuming stage even though optimization searches were performed. Some iterations were needed because each geometric adjustment produces an impedance change and a shift in the tuning frequency which required modifications of the component values to keep the same impedances. In the final step three loops were involved adding more complexity to the process. The goal of this adjustment is to reduce the overall coupling in the coil. S-parameters simulations, performed with each loop matched to the source, revealed good decoupling between isolated pairs of loops and also acceptable levels for the complete array when loaded with the M size load. The maximum S_{21} value (-14.32 dB) was also acceptable considering that -15 dB is recommended for critically

overlapped loops. However, when the size of the coil and the sample were changed the maximum dispersion of S_{21} values augmented having a maximum S_{21} values between -9.38 dB and -7.47 dB. Since even a small dimension change created a considerable dispersion in S_{21} parameters, as observed between 10.25 and 11.4 cm, and considering that the probability of having the coil operating in the geometrical decoupling condition was very low, it was concluded that the critical overlapping adjustment makes no sense in an adjustable array where all the elements are moved independently. This conclusion was somehow in agreement with other size varying array concepts [99], [100], [101], [102]. In these arrays however, the change experienced by the ratio between the overlapping area and the loop area is less dramatic than in the array proposed in this work. In those concepts both areas are modified at the same time while in the array proposed here only the overlapping area changes.

The previous conclusion provided more flexibility for the mechanical design allowing a more convenient placement of all the supporting structures, PCBs and pneumatic parts. The displacements of the elements caused changes in the S-parameters of the complete array. Reductions of 2.38, 2.05 and 2.67 dB in the average S_{21} values were observed for the two smallest and the M-size respectively, while increases of 2.76 and 1.41 dB were observed for the largest sizes. These values were in correspondence with the geometry changes which were not substantial. However, the dispersion of S_{21} values for the M-size sample suffered a considerable increase due to the loss of the critical overlapping condition that was adjusted for this coil size. For the other dimensions, the dispersion increase was not significant either. As a conclusion, the coil was not considerably degraded in terms of decoupling in the complete size range, being improved for the largest dimensions.

The values of preamplifier decoupling obtained for all the isolated elements, being between -30.7 and -34.1 dB allowed to increase the levels of decoupling in the simulated array in a considerable amount. Improvements of 21.57, 23.84, 22.38, 22.31 and 27.19 dB were respectively obtained for all five dimensions. The average and the maximum values were also similar, which suggested that the array could behave in a stable way across the complete range.

The near field simulations resulted in magnetic field maps (B_1^-) showing improved distributions compared to the versions of the array where the preamplifier circuits were not included. However, the field maps were not as expected for all the selected slices. A strong contribution to the total

field was observed from the loop 1 (located on top), being progressively attenuated from top to bottom in the coil. For that reason, a more realistic field distribution was observed in the lower slice, where the field was mainly induced by the elements 8 to 13.

6.3 Coil parameters

The coil showed satisfactory parameters during the bench tests. The obtained values were comparable to fixed-size coils made with critical overlapping.

The isolated loops were matched to an average impedance of 239 Ohm with the M phantom to leave a margin for the expected reduction after the introduction in the array. For that reason, the capacitors selected for matching were around 20% lower that the values obtained by simulations. The final capacitance values resulted in an average loop impedance, with the M-phantom and the array completely assembled, of 184 Ohm which is relatively close to the target impedance of 175 Ohm. This impedance was measured with the other loops detuned, which is the usually recommended method [67]. It is worth to mention that the impedance measured in this way is not the real impedance “seen” by the preamplifier during the normal operation of the coil.

During image acquisitions, all elements are receiving at the same time. In this case the detuning signal is not active and the interaction between channels affects the impedance of all the loops. In this work, it was preferred to measure also the impedance in these more realistic conditions. The test reported values of nearly 150 Ohm for the M phantom, while for the S and L phantoms the values were about 169 and 118 Ohm respectively. All these values were in the range recommended by the preamplifier manufacturer (50 to 200 Ohm). The impedance reduction and the shape changes of the impedance curves from one method to the other provided an idea about the effectiveness of the preamplifier decoupling as the unique decoupling method in the proposed coil. It can be concluded from this results that the designed circuits could provide adequate decoupling between channels since the impedance changes between detuning and non-detuning conditions were not significant. However, there is still a margin that can be used to improve the decoupling in this coil, which can be achieved by increasing the impedance of the loops.

The previous values were possible due to a preamplifier decoupling level of around -25 dB. This value was about 17% worse than the simulated ones. During simulations, the resistances introduced

by the physical circuits (PCB traces, solder joints, 4-way connector, etc.) were not considered, which provided over-dimensioned isolation levels in the coil.

A dispersion was observed in the impedance values of the loops. An important part of the differences can be attributed to the geometry of the phantoms that was not a perfect sphere as in the simulations. In addition, the loops of the bottom row (8 to 13) were restructured to better conform to the shape of the phantoms and potential patients. If required the loops could be individually adjusted by using different matching capacitors for each loop, but this is not a practical solution.

The unloaded-to-loaded quality factors ratio guaranteed sample load dominance for all loops and coil dimensions. The loaded Q decreased, as expected, when the loops were all placed in the coil and all the other components were connected. The reductions were 17.1, 15.5 and 8.4% for the S, M and L phantoms respectively. The same numbers represent the resistance increases contributed by the array components, which were always between 0.39 and 0.53 Ohm. The loading effect of the array components decreased with the increase of the coil size due to the lower concentration of metallic parts. Tuning frequency shifts, with respect to the adjustments made for the M phantom, were not substantial considering that the Q spoiling produced by the preamplifier input circuit reduces the detuning effect [37].

High coupling levels were measured between pairs of loops, even though only the loops 1 to 7 were tested as performing the measurements in the complete coil is overly time-consuming. However, this test provides the decoupling base values and can be completed if they are needed to determine the level of preamplifier decoupling required to obtain the required overall decoupling.

The preliminary tests to find the impact of the distance between loops on the frequency response of two coil channels were used as a base to compare the final measurements similarly performed on the assembled coil. The final “dog-ear” shaped curves, which were very similar to the preliminary obtained curves, were an additional confirmation of the reduced interaction among coil elements, mainly in the proximities of the Larmor frequency. The distortion of these curves was negligible near the operating frequency and non-severe at more separated frequencies. Specifically, the worst distortions were observed at the frequencies where the tuning split peaks created by the preamplifier connection interact but they are irrelevant since they are more than 5MHz apart. This

result is consistent with previous findings [89]. High stability was achieved in the final coil as no oscillation peaks were detected in a very wide frequency range.

6.4 Scanner tests

Images with higher total SNR for almost all phantoms, compared to the reference coil, were obtained with the proposed coil. This result could be expected due to the tight fitting of the elements to the different loads. The intensity distribution was also similar for all the studied phantoms, which means that the coil operates in a consistent way across the size range. The pattern with the intensity decreasing as the distance from the surface increases is expected from a receiver array coil with elements closely positioned around the samples.

The total levels of decoupling observed during the bench tests were confirmed by the noise correlation values obtained from the zero-excitation scans of all phantoms. This means that the preamplifier decoupling compensated the significant overall mutual coupling that exists in this array. Even though the average correlation values are higher in the proposed coil, they remain acceptable considering the lack of critical overlapping and that a higher coupling exists between non-adjacent elements that are relatively close due to their dimensions. Notice that the maximum values obtained for both coils are very similar and they correspond to adjacent elements in the commercial coil. A factor that promoted the lower correlation levels in the commercial coil was the relative size between the coil and the phantoms and the longer distance that in general exists between non-adjacent elements.

Some regions with lower than expected intensities were observed in the proximities of the phantom surface. They were attributed to feedback paths that could exist between the output circuits and the loops that become active when an MR signal is present. This assertion is based in two facts: first, the noise correlation matrices are clean of high correlation values and they were computed on a zero-excitation acquisition. The correlation values are similar to those obtained with the commercial coil and to other adaptable arrays that do not preserve the critical overlapping across all the range [99]. Second: after the detection of oscillations during a preliminary scan test, some minor improvements were implemented in the output circuits that resulted in a reduction of the low-intensity regions and other changes in the intensity distribution. Specifically, the output cables of all channels were rerouted, and a partial shielding was added to the cable traps. As a result, the

oscillations disappeared for all coil conditions and dimensions, even when the elements were touched. This means that geometry-dependent feedback loops existed in the coil. These loops created the oscillation of the preamplifiers and could also create image cancellation regions. Since there are still non-shielded parts in the output circuits, it could be concluded that some remaining coupling could be leading to small image uniformity issues.

6.5 Room for improvement

The structure of the coil was intentionally designed without introducing too much complexity since the project was already risky. After the feasibility of the concept was proved, it can be concluded that the coil can be further improved.

The physical preamplifier structure was relatively small and convenient for developing the coil compared to the other sample tested. However, it contributed to make the design of the input circuit more complex as the 4-way input connector added some reactance (mainly inductive) and resistance due to connection contacts. A smaller preamplifier, especially designed for this application, which can also be integrated in the matching board, would reduce these parasitic components and improve decoupling. It can also facilitate the increase in number of channels as more space can be available. This solution might be investigated in partnership with GE, which recently developed miniaturized preamplifiers and are willing to collaborate with us for this application. Another possibility could be integrating the loop, the matching/detuning circuit and a custom-made preamplifier in a single PCB for each channel. A thinner structure is possible using PCB, which could help to ease sliding the loops and placing them nearer to the sample, which will further increase the SNR. Notice that in the current design the loops are separated by about 10 mm from the surface of the sample.

Adding elements to the coil can improve SNR near the head surface without considerably degrading it in the centre of the sample [52], [54]. This change can reduce the coupling between non-adjacent elements, mostly between those located ones in front of the others, which also contribute to couple the adjacent loops. On the other hand, simple calculations show that a very small gain in size range is achieved if the number of elements is increased, since the loops and overlapping areas should be scaled down to cover the same region.

The shielding of the output circuits (output PCB, cable traps, cables) can be improved to reduce possible residual output-to-input destructive coupling among elements, which arises when the magnetic resonance signal is present. Specifically, channels 1 and 4 have shown reduced levels of signal. The decoupling of those channels could be more problematic as the preamplifier of channel 1 is very close to the loop of channel 4. An obvious solution can be separate the preamplifier of channel 1 from the loop 4 in addition to improving the shielding.

CHAPTER 7 CONCLUSION AND RECOMMENDATIONS

The present work was focused on the development of an adjustable receiver RF coil for the neonate head to be used in a 3T GE scanner.

7.1 Conclusions

- A new pneumatic-based size-adjustable array coil was designed, built and evaluated.
- It was demonstrated the feasibility of constructing an adaptable coil with fixed-size loops that move simultaneously and independently, having considerable changes in the overlapping area between all adjacent loops. To the best of our knowledge, this is the first constructed array showing this set of features.
- The proposed approach resulted in up to 68% in the head region and 122% in the cortex region compared to a 32-channel commercial head coil which is frequently used to scan infants.
- Reasonably constant SNR values were obtained in the cortex region across the coil size range, which allows to scan a variety of head dimensions with stable results.
- The coil is easy to operate and only a few seconds are needed to complete the backward and forward displacement of the elements during the placement of the subject and the adaptation to the head shape.
- The method can help to restrict head motion if proper padding is used since no free space remains between the head and the coil.
- The design has potential applications to other age groups and size-varying body parts, such as breast and limbs.

The novelty of the proposed adjustable coil and the applicability range made possible the filing of a provisional patent application (Appendix B). In addition, the preliminary results were presented at the ISMRM 25th annual meeting & exhibition (2017) where it was selected for an oral presentation (http://cds.ismrm.org/protected/17MPresentations/abstracts/1053.html).

7.2 Recommendations

The next step in the development of this coil must be performing in vivo experiments to confirm the phantom results and demonstrate the feasibility in more real conditions. The possibility to detect small biological structures must be explored, even though the high SNR values obtained with the phantoms indicate so.

Before this coil can be used in human neonates the complete Safety and Regulatory Requirements protocol established by GE must be fulfilled. An important test is the known loading test, which consists in performing body coil acquisitions without the coil and with the detuned coil to compare RF power values for the same flip angle, must be performed. This test will give an additional idea about how efficient is the decoupling since any difference means that some power is absorbed by the receiver coil. That power could heat some coil parts or could harm the patient by creating hot spots and burns. Another safety-related test that should be performed is running a demanding sequence in terms of gradients during some time and measure the temperature in some coil components afterward.

Since parallel imaging capability is critical for neonatal brain studies, the coil should be tested in acceleration experiments to determine how much the scan times could be reduced without losing diagnosis quality. Comparison of G factor maps for different reduction factors obtained from both coils could provide a more complete idea about the quality of the coil.

In order to bring the project to a higher degree of completion, an adapted patient bed could be designed and constructed. The bed must be provided with a height control mechanism to place the patient in the geometrical center of the coil as the dimensions of the latter vary symmetrically around its center. In a similar manner, the height control mechanism could be included in the mechanical design of the coil.

BIBLIOGRAPHY

[1] J. J. Volpe, "Brain injury in premature infants: a complex amalgam of destructive and developmental disturbances," *Lancet Neurol,* vol. 8, no. 1, pp. 110-124, 2009/01/01/ 2009.

[2] S. A. and C. J.B., "Neonatal Brain Injury," in *Common Neurosurgical Conditions in the Pediatric Practice*New York, USA: Springer, 2017, pp. 47-59.

[3] S. Shankaran *et al.*, "Acute Perinatal Sentinel Events, Neonatal Brain Injury Pattern, and Outcome of Infants Undergoing a Trial of Hypothermia for Neonatal Hypoxic-Ischemic Encephalopathy," *J. Pediatr.,* vol. 180, no. Supplement C, pp. 275-278.e2, 2017/01/01/ 2017.

[4] M. A. Rutherford, 4 ed. W.B. Saunders, 2002.

[5] S. P. Miller *et al.*, "Abnormal brain development in newborns with congenital heart disease," *N Engl J Med,* vol. 357, no. 19, pp. 1928-38, Nov. 2007.

[6] E. J. Hughes *et al.*, "A dedicated neonatal brain imaging system," *Magn Reson Med,* vol. 72, no. 2, pp. 794–804, Sep. 19 2016.

[7] SREE Medical Systems. (2013). *Infant Head Spine Array* [Online]. Available: http://advimg.com/infant_head_spine_array.html

[8] P. B. Roemer, W. A. Edelstein, C. E. Hayes, S. P. Souza, and O. M. Mueller, "The NMR phased array," *Magn Reson Med,* vol. 16, no. 2, pp. 192-225, Nov. 1990.

[9] B. Keil *et al.*, "Size-optimized 32-channel brain arrays for 3 T pediatric imaging," *Magn Reson Med,* vol. 66, no. 6, pp. 1777-87, Jun. 2011.

[10] A. Mareyam *et al.*, "Brain arrays for neonatal and premature neonatal imaging at 3T," in *ISMRM-21*, Salt Lake City, USA, 2013, p. 4386.

[11] D. Driemel, "MRI adjustable head coil," US Patent 8,190,237 B2, 2012.

[12] V. Taracila, M. Navarro, D. Gregan, S. Ortman, and R. Fraser, "Adaptive Head Array," in *ISMRM-22*, Milan, Italy, 2014, p. 4883.

[13] V. Taracila, M. Navarro, D. Gregan, K. Juhasz, S. Leversee, and R. Fraser, "Adjustable MRI head coil apparatus and MRI system," US Patent 2013/0076358A1, 2013.

[14] M. Banerjee *et al.*, "Optimized Pediatric Suite with head array adjustable for patients 0-5 yrs of age," in *ISMRM-22*, Milan, Italy, 2014, p. 4383.

[15] Z.-P. Liang and P. C. Lauterbur, *Principles of Magnetic Resonance Imaging*. New York, USA: IEEE Press, 2000.

[16] D. I. Hoult, "The principle of reciprocity in signal strength calculations—A mathematical guide," *Concepts Magn Reson,* vol. 12, no. 4, pp. 173-187, Jun. 2 2000.

[17] C. N. Chen and D. I. Hoult, *Biomedical Magnetic Resonance Technology*. New York, USA: Taylor & Francis, 1989, p. 250.

[18] D. G. Nishimura, *Principles of Magnetic Resonance Imaging*. Stanford University, USA, 1996.

[19] D. I. Hoult and R. E. Richards, "The signal-to-noise ratio of the nuclear magnetic resonance experiment," *J Magn Reson,* vol. 213, no. 2, pp. 329-343, Dic. 01 1976.

[20] K. P. Pruessmann, M. Weiger, M. B. Scheidegger, and P. Boesiger, "SENSE: Sensitivity Encoding for Fast MRI," *Magn Reson Med,* vol. 42, pp. 952–962, Nov. 1999.

[21] E. B. Boskamp, "Improved surface coil imaging in MR: decoupling of the excitation and receiver coils," *Radiology,* vol. 157, no. 2, pp. 449-452, Nov. 1985.

[22] W. A. Edelstein, C. J. Hardy, and O. M. Mueller, "Electronic decoupling of surface-coil receivers for NMR imaging and spectroscopy," *J Magn Reson,* vol. 67, no. 1, pp. 156-161, Mar. 1986.

[23] W. A. Edelstein, "Radiofrequency Systems and Coils for MRI and MRS," in *Encyclopedia of nuclear magnetic resonance*: John Wiley & Sons, Ltd, 2007.

[24] J. S. Hyde, R. J. Rilling, and A. Jesmanowicz, "Passive decoupling of surface coils by pole insertion," *J Magn Reson,* vol. 89, no. 3, pp. 485-495, Oct. 1990.

[25] J. Mispelter, M. Lupu, and A. Briguet, "Balancing the Probehead," in *NMR probeheads for biophysical and biomedical experiments : theoretical principles & practical guidelines.*1st ed. London, UK: Imperial College Press, 2009, pp. 93-129.

[26] J. Mispelter, M. Lupu, and A. Briguet, "Magnetic Field Amplitude Estimation," in *NMR probeheads for biophysical and biomedical experiments : theoretical principles & practical guidelines.*1st ed. London, UK: Imperial College Press, 2009, pp. 261-300.

[27] S. B. King, S. Varosi, D. A. Molyneaux, and G. R. Duensing, "The Effects of Ultra Low Input Impedance Preamplifiers on Phased Array Coil Design," in *ISMRM-10*, 2002.

[28] R. G. Oppelt, "Weekend Educational Course: Introduction to preamplifiers," in *ISMRM-17*, Stockholm, Sweden, 2010.

[29] T. W. Redpath, "Noise correlation in multicoil receiver systems," *Magn Reson Med,* vol. 24, no. 1, pp. 85-89, Mar. 28 1992.

[30] C. C. Guclu and P. Seteen, "A noise correlation measurement tool for multi-channel RF coils," in *ISMRM-8*, Denver, USA, 2000.

[31] C. E. Hayes and P. B. Roemer, "Noise correlations in data simultaneously acquired from multiple surface coil arrays," *Magn Reson Med,* vol. 16, no. 2, pp. 181-191, Nov. 1990.

[32] *Characterization of Phased Array Coils for Diagnostic Magnetic Resonance Images*, MS 9-2008 (R2014), 2008.

[33] *Determination of Signal-to-Noise Ratio and Image Uniformity for Single-Channel Non-Volume Coils in Diagnostic MR Imaging*, MS-6 (R2014), 2008.

[34] *Determination of Signal-to-Noise Ratio (SNR) in Diagnostic Magnetic Resonance Imaging*, MS-1 (R2014), 2008.

[35] H. Gudbjartsson and S. Patz, "The Rician distribution of noisy MRI data," *Magn Reson Med,* vol. 34, pp. 910-914, Dic. 1995.

[36] R. M. Henkelman, "Measurement of signal intensities in the presence of noise in MR images," *MED PHYS,* vol. 12, no. 2, pp. 232-233, Mar./Apr. 1985.

[37] B. Keil and L. L. Wald, "Massively parallel MRI detector arrays," *J Magn Reson,* vol. 229, pp. 75-89, Apr. 2013.

[38] C. E. Hayes, N. Hattes, and P. B. Roemer, "Volume imaging with MR phased arrays," *Magn Reson Med,* vol. 18, no. 2, pp. 309-319, Apr. 1991.

[39] C. E. Hayes, M. J. Dietz, B. F. King, and R. L. Ehman, "Pelvic imaging with phased-array coils: Quantitative assessment of signal-to-noise ratio improvement," *J Magn Reson Imaging,* vol. 2, no. 3, pp. 321-326, May.-Jun. 1992.

[40] C. E. Hayes, J. S. Tsuruda, and C. M. Mathis, "Temporal lobes: surface MR coil phased-array imaging," *Radiology,* vol. 189, no. 3, pp. 918-920, Dec. 1993.

[41] C. D. Constantinides, C. R. Westgate, W. G. O'Dell, E. A. Zerhouni, and E. R. McVeigh, "A phased array coil for human cardiac imaging," *Magn Reson Med,* vol. 34, no. 1, pp. 92-98, Jul. 1995.

[42] C. E. Hayes, C. M. Mathis, and C. Yuan, "Surface coil phased arrays for high-resolution imaging of the carotid arteries," *J Magn Reson Imaging,* vol. 6, no. 1, pp. 109-112, Jan.-Feb. 1996.

[43] J. R. Porter, S. M. Wright, and A. Reykowski, "A 16-element phased-array head coil," *Magn Reson Med,* vol. 40, no. 2, pp. 272-279, Aug. 1998.

[44] J. W. Carlson, "An algorithm for NMR imaging reconstruction based on multiple RF receiver coils," *J Magn Reson,* vol. 74, no. 2, pp. 376-380, 1987.

[45] M. Hutchinson and U. Raff, "Fast MRI data acquisition using multiple detectors," *Magn Reson Med,* vol. 6, no. 1, pp. 87-91, 1988.

[46] D. Kwiat, S. Einav, and G. Navon, "A decoupled coil detector array for fast image acquisition in magnetic resonance imaging," *MED PHYS,* vol. 18, no. 2, pp. 251-265, Mar.-Apr. 1991.

[47] J. B. Ra and C. Y. Rim, "Fast imaging using subencoding data sets from multiple detectors," *Magn Reson Med,* vol. 30, no. 1, pp. 142-145, Dec. 1993.

[48] D. K. Sodickson and W. J. Manning, "Simultaneous acquisition of spatial harmonics (SMASH): Fast imaging with radiofrequency coil arrays," *Magn Reson Med,* vol. 38, no. 4, pp. 591-603, Oct. 1997.

[49] M. A. Ohliger, A. K. Grant, and D. K. Sodickson, "Ultimate intrinsic signal-to-noise ratio for parallel MRI: Electromagnetic field considerations," *Magn Reson Med,* vol. 50, no. 5, pp. 1018-1030, Nov. 2003.

[50] F. Wiesinger, P. Boesiger, and K. P. Pruessmann, "Electrodynamics and ultimate SNR in parallel MR imaging," *Magn Reson Med,* vol. 52, no. 2, pp. 376-390, Aug. 2004.

[51] F. Wiesinger, P.-F. Van de Moortele, G. Adriany, N. De Zanche, K. Ugurbil, and K. P. Pruessmann, "Parallel imaging performance as a function of field strength—An experimental investigation using electrodynamic scaling," *Magn Reson Med,* vol. 52, no. 5, pp. 953-964, Nov. 2004.

[52] F. Wiesinger, N. De Zanche, and K. P. Pruessmann, "Approaching Ultimate SNR with Finite Coil Arrays," in *ISMRM-13*, South Beach, USA, 2005, p. 672.

[53] R. Lattanzi *et al.*, "Performance evaluation of a 32-element head array with respect to the ultimate intrinsic SNR," *NMR Biomed,* vol. 23, no. 2, pp. 142-51, Nov. 10 2010.

[54] G. C. Wiggins, J. R. Polimeni, A. Potthast, M. Schmitt, V. Alagappan, and L. L. Wald, "96-channel receive-only head coil for 3 Tesla: design optimization and evaluation," (in English), *Magn Reson Med,* Journal Article vol. 62, no. 3, pp. 754-762, Sep. 2009.

[55] B. Keil *et al.*, "A 64-channel 3T array coil for accelerated brain MRI," *Magn. Reson. Med. (USA),* vol. 70, no. 1, pp. 248-58, Jul. 2013.

[56] R. F. Lee, C. J. Hardy, D. K. Sodickson, and P. A. Bottomley, "Lumped-element planar strip array (LPSA) for parallel MRI," *Magn Reson Med,* vol. 51, no. 1, pp. 172-183, Jan. 2004.

[57] G. Adriany *et al.*, "Transmit and receive transmission line arrays for 7 Tesla parallel imaging," *Magn Reson Med,* vol. 53, no. 2, pp. 434-445, Feb. 2005.

[58] W. Driesel, T. Mildner, and H. E. Möller, "A microstrip helmet coil for human brain imaging at high magnetic fields," *Concepts Magn Reson Part B Magn Reson Eng,* vol. 33B, no. 2, pp. 94-108, Apr. 8 2008.

[59] G. Adriany *et al.*, "A 32-channel lattice transmission line array for parallel transmit and receive MRI at 7 tesla," *Magn Reson Med,* vol. 63, no. 6, pp. 1478-85, Jun. 2010.

[60] O. C. Morse and J. R. Singer, "Blood Velocity Measurements in Intact Subjects," *Science,* vol. 170, no. 3956, pp. 440-441, Oct. 23 1970.

[61] J. J. H. Ackerman, T. H. Grove, G. G. Wong, D. G. Gadian, and G. K. Radda, "Mapping of metabolites in whole animals by 31P NMR using surface coils," *Nature,* vol. 283, no. 5743, pp. 167-170, 1980.

[62] D. Hoult, "The NMR receiver: A description and analysis of design," *Prog Nucl Magn Reson Spectrosc,* vol. 12, no. 1, pp. 41-77, 1978.

[63] A. Kumar, W. A. Edelstein, and P. A. Bottomley, "Noise figure limits for circular loop MR coils," *Magn Reson Med,* vol. 61, no. 5, pp. 1201-1209, May. 2009.

[64] R. F. Lee, R. O. Giaquinto, and C. J. Hardy, "Coupling and decoupling theory and its application to the MRI phased array," *Magn Reson Med,* vol. 48, no. 1, pp. 203-213, Jul. 2002.

[65] B. Wu, P. Qu, C. Wang, J. Yuan, and G. X. Shen, "Interconnecting L/C components for decoupling and its application to low-field open MRI array," *Concepts Magn Reson Part B Magn Reson Eng,* vol. 31B, no. 2, pp. 116-126, Apr. 5 2007.

[66] G. C. Wiggins, C. Triantafyllou, A. Potthast, A. Reykowski, M. Nittka, and L. L. Wald, "32-channel 3 Tesla receive-only phased-array head coil with soccer-ball element geometry," *Magn Reson Med,* vol. 56, no. 1, p. 17, Jul. 2006.

[67] B. Keil, "Weekend Educational Course: Constructing of Receive Arrays," in *ISMRM-21*, Salt Lake City, USA, 2013.

[68] B. Keil *et al.*, "A 20-channel receive-only mouse array coil for a 3 T clinical MRI system," *Magn Reson Med,* vol. 66, no. 2, pp. 584-95, Aug. 2011.

[69] H. Fujita, T. Zheng, X. Yang, M. J. Finnerty, and S. Handa, "RF surface receive array coils: the art of an LC circuit," *J Magn Reson Imaging,* vol. 38, no. 1, pp. 12-25, Jul. 2013.

[70] J. A. de Zwart, P. J. Ledden, P. van Gelderen, J. Bodurka, R. Chu, and J. H. Duyn, "Signal-to-noise ratio and parallel imaging performance of a 16-channel receive-only brain coil array at 3.0 Tesla," *Magn Reson Med,* vol. 51, no. 1, pp. 22-26, Jan. 2004.

[71] G. C. Wiggins, C. Triantafyllou, A. Potthast, A. Reykowski, M. Nittka, and L. L. Wald, "A 32 Channel Receive-only Phased Array Head Coil for 3T with Novel Geodesic Tiling Geometry," in *ISMRM-13*, 2005.

[72] P. J. Ledden, A. Mareyam, S. Wang, P. van Gelderen, and J. H. Duyn, "Twenty-Four Channel Receive-Only Array for Brain Imaging at 7T," in *ISMRM-14*, Seattle, USA, 2006, p. 422.

[73] P. J. Ledden, A. Mareyam, S. Wang, P. van Gelderen, and J. Duyn, "32 Channel Receive-Only SENSE Array for Brain Imaging at 7T," in *ISMRM-15* Berlin, Germany, 2007, p. 242.

[74] V. Alagappan, G. C. Wiggins, J. R. Polimeni, and L. L. Wald, "A 32-channel Receive Array Coil for Pediatric Brain Imaging at 3T," in *ISMRM-17*, Honolulu, USA, 2009, p. 108.

[75] B. Keil, C. Triantafyllou, M. Hamm, and L. L. Wald, "Design Optimization of a 32-Channel Head Coil at 7T," in *ISMRM-18*, Stockholm, Sweden, 2010, p. 1493.

[76] J. Cohen-Adad, A. Mareyam, B. Keil, J. R. Polimeni, and L. L. Wald, "32-Channel RF coil optimized for brain and cervical spinal cord at 3 T," *Magn Reson Med,* vol. 66, no. 4, pp. 1198-1208, Mar. 23 2011.

[77] G. C. Wiggins *et al.*, "A 96-channel MRI System with 23- and 90-channel Phase Array Head Coils at 1.5 Tesla," in *ISMRM-13*, Miami Beach, USA, 2005, p. 671.

[78] B. Keil *et al.*, "A 64-Channel Array Coil for 3T Head/Neck/C-spine Imaging," in *ISMRM-19*, Montréal, Québec, Canada, 2011, p. 160.

[79] Y. Zhu *et al.*, "Highly parallel volumetric imaging with a 32-element RF coil array," *Magn Reson Med,* vol. 52, no. 4, pp. 869-77, Oct. 2004.

[80] C. J. Hardy, H. E. Cline, R. O. Giaquinto, T. Niendorf, A. K. Grant, and D. K. Sodickson, "32-Element receiver-coil array for cardiac imaging," *Magn Reson Med,* vol. 55, no. 5, pp. 1142-9, May. 2006.

[81] D. Spencer *et al.*, "Design of a 32 Channel Cardiac Array for Parallel Imaging," in *ISMRM-13*, Miami Beach, USA, 2005, p. 911.

[82] T. Lanz, P. Kellman, M. Nittka, A. Greiser, and M. Griswold, "A 32 Channel Cardiac Array Optimized for Parallel Imaging," in *ISMRM-14*, Seattle, USA, 2006, p. 2578.

[83] C. J. Snyder, L. De la Barre, G. Metzger, K. Ugurbil, and J. Vaughan, "32-Channel Receive Only Array for Cardiac Imaging at 7T," in *ISMRM-19*, Montréal, Canada, 2011, p. 165.

[84] M. Schmitt *et al.*, "A 128-channel receive-only cardiac coil for highly accelerated cardiac MRI at 3 Tesla," *Magn Reson Med,* vol. 59, no. 6, pp. 1431-1439, Jun. 2008.

[85] C. J. Hardy *et al.*, "128-channel body MRI with a flexible high-density receiver-coil array," *J Magn Reson Imaging,* vol. 28, no. 5, pp. 1219-25, Nov. 2008.

[86] G. Adriany *et al.*, "A geometrically adjustable 16-channel transmit/receive transmission line array for improved RF efficiency and parallel imaging performance at 7 Tesla," *Magn Reson Med,* vol. 59, no. 3, pp. 590-597, Jan. 28 2008.

[87] T. S. Ibrahim *et al.*, "20-to-8 Channel Tx Array with 32-channel Adjustable Receive-Only Insert for 7T Head Imaging," in *ISMRM-21*, Salt Lake City, USA, 2013, p. 4408.

[88] N. De Zanche, J. A. Massner, C. Leussler, and K. P. Pruessmann, "Modular design of receiver coil arrays," *NMR Biomed,* vol. 21, no. 6, pp. 644-54, Jul. 2008.

[89] J. A. Nordmeyer-Massner, N. De Zanche, and K. P. Pruessmann, "Mechanically adjustable coil array for wrist MRI," *Magn Reson Med,* vol. 61, no. 2, pp. 429-38, Feb. 2009.

[90] R. Brown *et al.*, "A flexible nested sodium and proton coil array with wideband matching for knee cartilage MRI at 3T," *Magn Reson Med,* vol. 76, no. 4, pp. 1325-1334, Oct. 2016.

[91] T. Zhang *et al.*, "A semiflexible 64-channel receive-only phased array for pediatric body MRI at 3T," *Magn Reson Med,* vol. 76, no. 3, pp. 1015-1021, Sep. 29 2015.

[92] M. H. Deppe, J. Parra-Robles, H. Marshall, T. Lanz, and J. M. Wild, "A flexible 32-channel receive array combined with a homogeneous transmit coil for human lung imaging with hyperpolarized 3He at 1.5 T," *Magn Reson Med,* vol. 66, no. 6, pp. 1788-1797, Dec. 2011.

[93] I. Hancu, E. Fiveland, K. Park, R. O. Giaquinto, K. Rohling, and F. Wiesinger, "Flexible, 31-Channel breast coil for enhanced parallel imaging performance at 3T," *Magn Reson Med,* vol. 75, no. 2, pp. 897-905, Feb. 2016.

[94] K. M. Gilbert *et al.*, "A geometrically adjustable receive array for imaging marmoset cohorts," *NeuroImage,* vol. 156, no. Supplement C, pp. 78-86, 2017/08/01/ 2017.

[95] D. Mager *et al.*, "An MRI receiver coil produced by inkjet printing directly on to a flexible substrate," *IEEE Trans Med Imaging,* vol. 29, no. 2, pp. 482-487, Feb. 2 2010.

[96] J. R. Corea, A. C. Arias, A. M. Flynn, G. C. Scott, P. J. Shin, and M. Lustig, "Screen Printed Flexible 2-Channel Receive Coil Array," in *ISMRM-21*, Salt Lake City, USA, 2013, p. 133.

[97] J. R. Corea *et al.*, "Design and Implementation of Flexible Printed Receive Coils Arrays," in *ISMRM-22*, Milan, Italy, 2014, p. 1314.

[98] J. R. Corea *et al.*, "Screen-printed flexible MRI receive coils," *Nat Commun*, vol. 7, Mar. 10. doi: 10.1038/ncomms10839 [Online]. Available: http://dx.doi.org/10.1038/ncomms10839

[99] J. A. Nordmeyer-Massner, N. De Zanche, and K. P. Pruessmann, "Stretchable coil arrays: Application to knee imaging under varying flexion angles," *Magn Reson Med,* vol. 67, no. 3, pp. 872-879, Mar. 2012.

[100] B. Gruber and S. Zink, "Anatomically adaptive local coils for MR Imaging Evaluation of stretchable antennas at 1.5T," in *ISMRM-24*, Singapore, 2016, p. 543.

[101] B. Gruber, K. Jahns, and S. Zink, "Adaptive MR local coil," US Patent 2017/0089991A1.

[102] G. C. Wiggins, B. Zhang, and B. Dornberger, "Size-adaptable “Trellis” receive array concept for knee imaging," in *ISMRM-24*, Singapore, 2016, p. 493.

[103] S. S. Vasanawala *et al.*, "Millimeter Isotropic Resolution Volumetric Pediatric Abdominal MRI with a Dedicated 32 Channel Phased Array Coil," in *ISMRM-19*, Montréal, Canada, 2011, p. 161.

[104] R. Giaquinto, W. Loew, S. Serai, J. Tkach, K. Emery, and C. Dumoulin, "A Novel Phased Array Coil for Limb Imaging Incorporating 3D Coil Overlaps," in *ISMRM-20*, Melbourne, Australia, 2012, p. 2653.

[105] M. A. López Terrones and S. E. Solís-Nájera, "A six-channel pediatric coil array for detection of children spinal pathologies by MRI at 1.5 Tesla," in *XIII Mexican Symposium on Medical Physics*, León, Guanajuato, Mexico, 2014, vol. 1626, pp. 82-85.

[106] Q. X. Yang *et al.*, "Manipulation of image intensity distribution at 7.0 T: Passive RF shimming and focusing with dielectric materials," *J Magn Reson Imaging,* vol. 24, no. 1, pp. 197-202, Jul. 2006.

[107] Q. X. Yang, J. Wang, J. Wang, C. M. Collins, C. Wang, and M. B. Smith, "Reducing SAR and enhancing cerebral signal-to-noise ratio with high permittivity padding at 3 T," *Magn Reson Med,* vol. 65, no. 2, pp. 358-362, Feb. 2011.

[108] W. M. Teeuwisse, W. M. Brink, K. N. Haines, and A. G. Webb, "Simulations of high permittivity materials for 7 T neuroimaging and evaluation of a new barium titanate-based dielectric," *Magn Reson Med,* vol. 67, no. 4, pp. 912-918, Apr. 2012.

[109] W. M. Teeuwisse, W. M. Brink, and A. G. Webb, "Quantitative assessment of the effects of high-permittivity pads in 7 Tesla MRI of the brain," *Magn Reson Med,* vol. 67, no. 5, pp. 1285-1293, May. 2012.

[110] R. Lattanzi, M. V. Vaidya, G. Carluccio, D. K. Sodickson, and C. M. Collins, "Signal-to-Noise Ratio gain at 3T using a thin layer of high-permittivity material inside enclosing receive arrays," in *ISMRM-22* Milan, Italy, 2014, p. 4814.

[111] W. Luo, Y. Qing, and C. M. Collins, "Improved surface coil performance at any depth in a lossy sphere with a dielectric disc," in *ISMRM-22*, Milan, Italy, 2014, p. 4812.

[112] A. K. Bitz *et al.*, "RF safety evaluation of different configurations of high-permittivity pads used to improve imaging of the cerebellum at 7 Tesla," in *ISMRM-22*, Milan, Italy, 2014, p. 4892.

[113] M. A. López Terrones, J. M. Algarín Guisado, M. J. Freire Rosales, F. A. Breuer, and R. Marquez, "Application of Magneto-Inductive Metamaterial Lenses in Parallel Imaging," in *ISMRM-20*, Melbourne, Australia, 2012, p. 2793.

[114] J. M. Algarin, M. A. Lopez, M. J. Freire, and R. Marques, "Signal-to-noise ratio evaluation in resonant ring metamaterial lenses for MRI applications," *New J Phys*, vol.

13, Nov. 8. doi: 10.1088/1367-2630/13/11/115006 [Online]. Available: http://iopscience.iop.org/article/10.1088/1367-2630/13/11/115006

[115] T. R. Fenton, "A new growth chart for preterm babies: Babson and Benda's chart updated with recent data and a new format," *BMC Pediatrics*, vol. 3, no. 13, Dic. 16. doi: 10.1186/1471-2431-3-13 [Online]. Available: https://www.ncbi.nlm.nih.gov/pmc/articles/PMC324406/pdf/1471-2431-3-13.pdf

[116] Centers for Disease Control and Prevention. (2001). *Data Table of Infant Head Circumference-for-age Charts. National Center for Health Statistics* [Online]. Available: https://www.cdc.gov/growthcharts/html_charts/hcageinf.htm

[117] W. L. Stutzman and G. A. Thiele, *Antenna theory and design*, 3rd ed. New York, USA: John Wiley & Sons, Inc., 2012.

[118] FEKO. Altair. (2010). *MRI Birdcage Coil Design. An application note on the modelling of a 7T MRI birdcage headcoil in FEKO* [Online]. Available: https://www.feko.info/applications/white-papers/mri-birdcage-coil-design/MRI-birdcage-coil-design

[119] B. K. Li, B. Xu, F. Liu, H. T. Hui, and S. Crozier, "High Frequency Electromagnetic Analysis using Hybrid MOM/FEM Method," in *ISMRM-14*, Milan, Italy, 2006, p. 699.

[120] B. K. Li, E. Weber, B. Beck, S. Blackband, and S. Crozier, "An Experimental Verification of a Hybrid MoM/FEM Method for RF Simulations in MRI," in *ISMRM-15*, Berlin, Germany, 2007, p. 450.

[121] D. B. Davidson, *Computational Electromagnetics for RF and Microwave Engineering*. New York, USA: Cambridge University Press, 2011.

[122] L. Bing Keong, L. Feng, E. Weber, and S. Crozier, "Hybrid numerical techniques for the modelling of radiofrequency coils in MRI," *NMR Biomed,* vol. 22, no. 9, pp. 937-51, Nov. 2009.

[123] F. J. C. Meyer, D. B. Davidson, U. Jakobus, and M. A. Stuchly, "Human Exposure Assessment in the Near Field of GSM Base-Station Antennas Using a Hybrid Finite Element/Method of Moments Technique," *IEEE Trans. Biomed. Eng.,* vol. 50, no. 2, pp. 224-233, Feb. 2003.

[124] H. Wang, M. Xu, C. Wang, and T. Hubing, "Impedance Boundary Conditions in a Hybrid FEM/MOM Formulation," *IEEE Trans. Electromagn. Compat.,* vol. 45, no. 2, pp. 198-206, May. 2003.

[125] X. Yuan, D. R. Lynch, and J. W. Strohbehn, "Coupling of Finite Element and Moment Methods for Electromagnetic Scattering from Inhomogeneous Objects," *IEEE Trans. Antennas Propag.,* vol. 38, no. 3, pp. 386-393, Mar. 1990.

[126] N. Benabdallah, N. Benahmed, B. Benyoucef, R. Bouhmidi, and M. H. Khelif, "Electromagnetic analysis of the slotted-tube resonator with a circular cross section for MRI applications," *Phys. Med. Biol.,* vol. 52, pp. 4943–4952, 2007.

[127] G. C. Wiggins, "Shaped MRI coil array," US Patent 2008/0007250 A1, 2008.

[128] G. R. Duensing, H. R. Brooker, and J. R. Fitzsimmons, "Maximizing Signal-to-Noise Ratio in the Presence of Coil Coupling," *J Magn Reson,* vol. 111, no. 3, pp. 230-235, Jun. 1996.

[129] X. Hu *et al.*, "A 20 channel head/neck array for three dimensional arterial wall imaging at 3T," in *ISMRM-22*, Milan, Italy, 2014, p. 2543.

[130] S. Ziegler, H. Braun, P. Ritt, C. Hocke, T. Kuwert, and H. H. Quick, "Systematic Evaluation of Phantom Fluids for Simultaneous PET/MR Hybrid Imaging," *J Nucl Med,* vol. 54, no. 8, pp. 1464-1471, Aug. 2013.

[131] FEKO. Altair. (2014). *MRI quantities B1+, B1-, ratio and iSNR. A Lua script that computes B1+, B1-, the ratio and the intrinsic SNR for MRI investigations* [Online]. Available: https://www.feko.info/support/lua-scripts/mri-b1-and-b1/mri-b1-and-b1

[132] A. Reykowski, S. M. Wright, and J. R. Porter, "Design of matching networks for low noise preamplifiers," *Magn Reson Med,* vol. 33, pp. 848-852, Jun. 1995.

[133] P. Kellman and E. R. McVeigh, "Image reconstruction in SNR units: a general method for SNR measurement," *Magn Reson Med,* vol. 54, no. 6, pp. 1439-47, Dec. 2005.

APPENDIX A – MATLAB CODES

Function to read the FEKO output file

```
function [ valuesFinal ]in:in;in = ReadFile( fileName )

index = 0;
found = 0;
values = zeros;
dataFinal = [];
openingSentence = '    sink source     real part   imag. part      linear      in dB     in deg.';
finalSentence = '         Sum |S|^2 of these S-parameters:';

% open the file
fileID = fopen(fileName,'r');

% make sure the file is not empty
finfo = dir(fileName);
fsize = finfo.bytes;

if fsize > 0

   while ~feof(fileID)

     tline = fgetl(fileID);

     while ischar(tline)

         if strcmp(tline, openingSentence)
            found = 1;
         end

         tline = fgetl(fileID);

         if (found == 1)
             foundFinalSentence = strfind(tline, finalSentence);

             while (isempty(foundFinalSentence))
                    A = sscanf(tline,'%s %u %u %f %f %f %f %f');
                    values(end + index) = A(7);
                    tline = fgetl(fileID);
                    foundFinalSentence = strfind(tline, finalSentence);
                    index = 1;
             end

             if (isempty(dataFinal))
                 dataFinal = values;
             else
                 dataFinal = [dataFinal;values];
             end

             values = [];
             found = 0;

         end
      end
   end
end

fclose(fileID);
valuesFinal = dataFinal;

end
```

S-parameters matrix construction (tuned/matched array)

```
[fileName,pathName] = uigetfile('*.txt','Select the file');

if isequal(fileName,0)
   disp('User selected Cancel')
else
   disp(['User selected ', fullfile(pathName, fileName)])

   prompt = {'X1:', 'X2:','Y1:', 'Y2:'};
   dlg_title = 'Input';
   num_lines = 1;
   defaultans = {'1','13', '1','13'};
   answer = inputdlg(prompt,dlg_title,num_lines,defaultans);
   x1 = str2num(answer{1});
   x2 = str2num(answer{2});
   y1 = str2num(answer{3});
   y2 = str2num(answer{4});

   fullMatrix = ReadFile(fullfile(pathName, fileName));

   subMatrix = fullMatrix (y1:y2,x1:x2);

   x = linspace(x1,x2,13);
   y = linspace(y1,y2,13);
   imagesc(x,y,subMatrix);
   set(gca,'FontSize',16);
   h = colorbar;
   set(h,'fontsize',16);

end
```

S-parameters matrix construction (array with preamplifier decoupling)

```
[fileName,pathName] = uigetfile('*.txt','Select the file');

if isequal(fileName,0)
   disp('User selected Cancel')
else
   disp(['User selected ', fullfile(pathName, fileName)])

   prompt = {'X1:', 'X2:','Y1:', 'Y2:'};
   dlg_title = 'Input';
   num_lines = 1;
   defaultans = {'1','13', '14','26'};
   answer = inputdlg(prompt,dlg_title,num_lines,defaultans);
   x1 = str2num(answer{1});
   x2 = str2num(answer{2});
   y1 = str2num(answer{3});
   y2 = str2num(answer{4});

   fullMatrix = ReadFile(fullfile(pathName, fileName));

   subMatrix = fullMatrix (y1:y2,x1:x2);

   [valueMax, location] = max(subMatrix);
   valueMax = valueMax (:);
   resultMatrix = bsxfun(@minus,subMatrix,valueMax);

   x = linspace(x1,x2,13);
   y = linspace(y1,y2,13);
   imagesc(x,y,resultMatrix);
   set(gca,'FontSize',16);
   h = colorbar ('northoutside');
   set(h,'fontsize',16);
   xlabel('Sinks'); ylabel('Sources');


end
```

APPENDIX B – PATENT APPLICATION FILING RECIPT

UNITED STATES PATENT AND TRADEMARK OFFICE

UNITED STATES DEPARTMENT OF COMMERCE
United States Patent and Trademark Office
Address: COMMISSIONER FOR PATENTS
P.O. Box 1450
Alexandria, Virginia 22313-1450
www.uspto.gov

APPLICATION NUMBER	FILING or 371(c) DATE	GRP ART UNIT	FIL FEE REC'D	ATTY.DOCKET.NO	TOT CLAIMS	IND CLAIMS
62/490,173	04/26/2017		130	05015490-116USPR		

CONFIRMATION NO. 7818

20988
NORTON ROSE FULBRIGHT CANADA LLP
1, Place Ville Marie
SUITE 2500
MONTREAL, QC H3B 1R1
CANADA

Received
MAY 09 2017
NORTON ROSE FULBRIGHT

FILING RECEIPT

OC00000009113140

Date Mailed: 05/04/2017

Receipt is acknowledged of this provisional patent application. It will not be examined for patentability and will become abandoned not later than twelve months after its filing date. Any correspondence concerning the application must include the following identification information: the U.S. APPLICATION NUMBER, FILING DATE, NAME OF APPLICANT, and TITLE OF INVENTION. Fees transmitted by check or draft are subject to collection. Please verify the accuracy of the data presented on this receipt. **If an error is noted on this Filing Receipt, please submit a written request for a Filing Receipt Correction. Please provide a copy of this Filing Receipt with the changes noted thereon. If you received a "Notice to File Missing Parts" for this application, please submit any corrections to this Filing Receipt with your reply to the Notice. When the USPTO processes the reply to the Notice, the USPTO will generate another Filing Receipt incorporating the requested corrections**

Inventor(s)

Nibardo LOPEZ RIOS, MONTREAL, CANADA;
Julien COHEN-ADAD, MONTREAL, CANADA;

Applicant(s)

Nibardo LOPEZ RIOS, MONTREAL, CANADA;
Julien COHEN-ADAD, MONTREAL, CANADA;

Power of Attorney:
A. Mandy--74714

Permission to Access Application via Priority Document Exchange: Yes

Permission to Access Search Results: Yes

Applicant may provide or rescind an authorization for access using Form PTO/SB/39 or Form PTO/SB/69 as appropriate.

If Required, Foreign Filing License Granted: 05/04/2017

The country code and number of your priority application, to be used for filing abroad under the Paris Convention, is **US 62/490,173**

Projected Publication Date: None, application is not eligible for pre-grant publication

Non-Publication Request: No

Early Publication Request: No
**** SMALL ENTITY ****

Title

MRI COIL APPARATUS AND METHOD

Statement under 37 CFR 1.55 or 1.78 for AIA (First Inventor to File) Transition Applications: No

PROTECTING YOUR INVENTION OUTSIDE THE UNITED STATES

Since the rights granted by a U.S. patent extend only throughout the territory of the United States and have no effect in a foreign country, an inventor who wishes patent protection in another country must apply for a patent in a specific country or in regional patent offices. Applicants may wish to consider the filing of an international application under the Patent Cooperation Treaty (PCT). An international (PCT) application generally has the same effect as a regular national patent application in each PCT-member country. The PCT process **simplifies** the filing of patent applications on the same invention in member countries, but **does not result** in a grant of "an international patent" and does not eliminate the need of applicants to file additional documents and fees in countries where patent protection is desired.

Almost every country has its own patent law, and a person desiring a patent in a particular country must make an application for patent in that country in accordance with its particular laws. Since the laws of many countries differ in various respects from the patent law of the United States, applicants are advised to seek guidance from specific foreign countries to ensure that patent rights are not lost prematurely.

Applicants also are advised that in the case of inventions made in the United States, the Director of the USPTO must issue a license before applicants can apply for a patent in a foreign country. The filing of a U.S. patent application serves as a request for a foreign filing license. The application's filing receipt contains further information and guidance as to the status of applicant's license for foreign filing.

Applicants may wish to consult the USPTO booklet, "General Information Concerning Patents" (specifically, the section entitled "Treaties and Foreign Patents") for more information on timeframes and deadlines for filing foreign patent applications. The guide is available either by contacting the USPTO Contact Center at 800-786-9199, or it can be viewed on the USPTO website at http://www.uspto.gov/web/offices/pac/doc/general/index.html.

For information on preventing theft of your intellectual property (patents, trademarks and copyrights), you may wish to consult the U.S. Government website, http://www.stopfakes.gov. Part of a Department of Commerce initiative, this website includes self-help "toolkits" giving innovators guidance on how to protect intellectual property in specific countries such as China, Korea and Mexico. For questions regarding patent enforcement issues, applicants may call the U.S. Government hotline at 1-866-999-HALT (1-866-999-4258).

LICENSE FOR FOREIGN FILING UNDER

Title 35, United States Code, Section 184

Title 37, Code of Federal Regulations, 5.11 & 5.15

GRANTED

The applicant has been granted a license under 35 U.S.C. 184, if the phrase "IF REQUIRED, FOREIGN FILING LICENSE GRANTED" followed by a date appears on this form. Such licenses are issued in all applications where the conditions for issuance of a license have been met, regardless of whether or not a license may be required as set forth in 37 CFR 5.15. The scope and limitations of this license are set forth in 37 CFR 5.15(a) unless an earlier

license has been issued under 37 CFR 5.15(b). The license is subject to revocation upon written notification. The date indicated is the effective date of the license, unless an earlier license of similar scope has been granted under 37 CFR 5.13 or 5.14.

This license is to be retained by the licensee and may be used at any time on or after the effective date thereof unless it is revoked. This license is automatically transferred to any related applications(s) filed under 37 CFR 1.53(d). This license is not retroactive.

The grant of a license does not in any way lessen the responsibility of a licensee for the security of the subject matter as imposed by any Government contract or the provisions of existing laws relating to espionage and the national security or the export of technical data. Licensees should apprise themselves of current regulations especially with respect to certain countries, of other agencies, particularly the Office of Defense Trade Controls, Department of State (with respect to Arms, Munitions and Implements of War (22 CFR 121-128)); the Bureau of Industry and Security, Department of Commerce (15 CFR parts 730-774); the Office of Foreign AssetsControl, Department of Treasury (31 CFR Parts 500+) and the Department of Energy.

NOT GRANTED

No license under 35 U.S.C. 184 has been granted at this time, if the phrase "IF REQUIRED, FOREIGN FILING LICENSE GRANTED" DOES NOT appear on this form. Applicant may still petition for a license under 37 CFR 5.12, if a license is desired before the expiration of 6 months from the filing date of the application. If 6 months has lapsed from the filing date of this application and the licensee has not received any indication of a secrecy order under 35 U.S.C. 181, the licensee may foreign file the application pursuant to 37 CFR 5.15(b).
